Electromechanical Modeling and Simulation of Thin Cardiac Tissue Constructs –

Smoothed FEM Applied to a Biomechanical Plate Problem

Von der Fakultät für Ingenieurwissenschaften,
Abteilung Bauwissenschaften
der Universität Duisburg-Essen
zur Erlangung des akademischen Grades

Doktor-Ingenieur

genehmigte Dissertation

von

Ralf Frotscher, M.Sc.

Hauptberichter:	Prof. Dr.-Ing. habil. J. Schröder
Betreuer:	Prof. Dr.-Ing. M. Staat
Korreferent:	Prof. Dr.-Ing. W. Kowalczyk

Tag der Einreichung:	14. September 2015
Tag der mündlichen Prüfung:	16. Februar 2016

Fakultät für Ingenieurwissenschaften,
Abteilung Bauwissenschaften
der Universität Duisburg-Essen
Institut für Mechanik
Prof. Dr.-Ing. habil. J. Schröder

Herausgeber:

Prof. Dr.-Ing. habil. J. Schröder

Organisation und Verwaltung:

Prof. Dr.-Ing. habil. J. Schröder
Institut für Mechanik
Fakultät für Ingenieurwissenschaften
Abteilung Bauwissenschaften
Universität Duisburg-Essen
Universitätsstraße 15
45141 Essen
Tel.: 0201 / 183 - 2682
Fax.: 0201 / 183 - 2680

Preface

The work on this thesis has been carried out under the supervision of Prof. Dr.-Ing. Manfred Staat at the Biomechanics Lab at Aachen University of Applied Sciences (FH Aachen) in Jülich where I started working in September 2010, in cooperation with Prof. Dr.-Ing. habil. Jörg Schröder, the director of the Institute for Mechanics at the University Duisburg-Essen.

My work has been financially supported by

- the ZIM cooperative project "Einstellbares alloplastisches Schlingensystem zur minimalinvasiven Therapie der Belastungsinkontinenz bei Frauen" (2010–2011) funded by the German Federal Ministry of Economics and Technology (BMWi),
- the project "Cardia$_{kytos}$: Messung mechanischer Grundspannungen und Schlagamplituden von Monolayern stammzellbasierter Kardiomyozyten für die funktionelle Medikamenten- und Toxinforschung" (2011–2013) that has been selected from the operational program for NRW in 'Ziel 2: Regionale Wettbewerbsfähigkeit und Beschäftigung' (2007–2013) which is co-financed by EFRE,
- the project "Optimierung des Systems Netzimplantat-Beckenboden zur therapeutischen Gewebeverstärkung nach der Integraltheorie" (2013–2015) funded by the German Federal Ministry of Education and Research and
- the project "CardiacDrums: Messung mechanischer Grundspannungen und Schlagamplituden von hiPS-basierten Kardiomyozyten für funktionelle Medikamenten- und Toxintests in der personalisierten Medizin" (2014–2015) funded by funded by the German Ministry of Innovation, Science and Research (MIWF) through the program Translational Stem Cell Research.

My first and deep thankful thoughts are dedicated to Prof. Dr.-Ing. Manfred Staat who guided me through this thesis and who taught me scientific working. His invaluable personal and professional support was accompanied by introducing me into the field of Computational Biomechanics, by letting me develop my own scientific interests, by giving me the freedom to gain a broad and deep knowledge in different fields, by patience and by flexibility.

I want to thank Prof. Dr.-Ing. habil. Jörg Schröder for providing me the chance to obtain a PhD degree at his institute in terms of this cooperation and for his valuable comments on my mork.

Dr.-Ing. Minh Tuan Duong, who recently obtained his PhD degree at RWTH Aachen, I want to thank for his kindness and for the countless interesting, engaged, detailed, critical and thoughtful discussions through five years. I also thank Dr.-Ing. Thanh Ngoc Tran who introduced me into the smoothed FEM and Karl-Heinz Gatzweiler for the introduction in practical FEA and his technical support. The researchers at the Lab

of Medical and Molecular Biology helped me understanding cellular electrophysiology and how cells behave in a tissue. Dr. rer. nat. Matthias Goßmann performed all the experiments that are computationally investigated in here and I deeply appreciate his patience in explaining his work to me. Dr.-Ing. Dominik Brands and Dr.-Ing. Alexander Schwarz were very courteous in supporting my PhD project administratively and with regard to contents, respectively.

Special thanks to all the scientists I was able to meet at conferences and summer schools in Graz, Barcelona, Vienna, Minsk, Paris, Pavia and Aachen and to the graduate program of FH Aachen that financially supported some of these visits. These opportunities to personally discuss own and others work and to learn from experienced and leading researchers were precious.

I also want to thank my family who always encouraged me in continuing my academic career, my dear colleagues at FH Aachen and my Volleyball team for talking with me about anything but my work.

The final paragraph is short because I do not have words to express the love and gratitude I feel for my wife and daughters. Luckily I am able to show both everyday.

Leinfelden-Echterdingen, in February 2016 Ralf Frotscher

Abstract

This work models and simulates an inflation test for *in vitro* cardiac tissues in the framework of the Finite Element Method (FEM). It focuses on the simulation of drug treatment of autonomously beating cardiac tissue consisting of human-induced pluripotent stem cell-derived cardiac myocytes and the validation based on in-house experimental results and on literature data. The ultra-thin composite material is modeled as a shell that is coupled with Hodgkin-Huxley based systems of differential equations describing the cellular electrophysiology. Additionally, the edge-based smoothed FEM is investigated concerning its applicability to biomechanical plate problems. This method achieves a higher accuracy than the standard FEM by smoothing the element-wise constant compatible strains over the edges of the finite element mesh. It is especially beneficial in the computation of strongly distorted elements that are often created by automatic meshing of anatomical structures.
The thesis starts by introducing the employed plate and FE theories, the electromechanical basics of cardiac tissue as well as of drug treatment and corresponding computational models. The model is then applied to the inflation test that serves as the validation basis for the quality and the ability of the model to predict drug effects on cardiac tissue.

Zusammenfassung

In dieser Arbeit wird ein Aufblasversuch für *in vitro* Herzgewebe im Rahmen der Finite Elemente Methode (FEM) modelliert und simuliert. Ziel ist dabei insbesondere die Simulation von Medikamentenwirkung auf auto-kontraktile Herzgewebe bestehend aus von human-induzierten pluripotenten Stammzellen abgeleiteten Kardiomyozyten und der Abgleich mit hausinternen experimentellen Resultaten und mit Literaturdaten. Für das sehr dünne Kompositmaterial wird ein Schalenmodell aufgestellt und mit Hodgkin-Huxley basierten Differentialgleichungssystemen gekoppelt, die die zelluläre Elektrophysiologie beschreiben. Zusätzlich wird die kanten-basiert geglättete FEM auf ihre Anwendbarkeit auf biomechanische Schalenprobleme hin untersucht. Diese Methode glättet die elementweise konstanten, kompatiblen Dehnungen über Elementgrenzen hinweg und erreicht so eine höhere Genauigkeit, als die Standard FEM. Darüberhinaus eignet sie sich in besonderem Maße für die Berechnung auf stark verzerrten Elementen, die bei automatischer Netzgenerierung für anatomische Strukturen häufig entstehen.
Zunächst werden die verwendeten Schalen- und FE-Theorien, die elektromechanischen Grundlagen von Herzgeweben, sowie von Medikamentenwirkung und einschlägige Modelle vorgestellt. Im Anschluß wird das Modell auf den Aufblasversuch angewandt, an dem die Qualität und die Fähigkeit des Modells Medikamentenwirkung auf Herzgewebe vorherzusagen, validiert und beurteilt werden.

Abbreviations

CE	contractile element
CM	cardiomyocyte
DSG	Discrete Shear Gap
ECM	extracellular matrix
hiPSC	human-induced pluripotent stem cell
hePSC	human embryonic pluripotent stem cell
hiPSC-CM	human-induced pluripotent stem cell-derived cardiomyocyte
FEM	Finite Element Method
HMT	Hunter-McCulloch-ter Keurs (model)
MNT	McAllister-Noble-Tsien (model)
NHS	Niederer-Hunter-Smith (model)
ODE	ordinary differential equation
PE	parallel element
Q4	4-noded quadrilateral (element)
SE	series element
S-FEM	Smoothed Finite Element Method
TnC	troponin C
TT	ten Tusscher (model)
T3, T4, T6, T7	3-, 4-, 6-, 7-noded triangular (element)

Important symbols and notation

Indices

i	$\in \{1, 2, 3\}$
α	$\in \{1, 2\}$
I	$\in \mathbb{N}_0$

Continuum Mechanics

$\boldsymbol{e}_i, e_i$	global coordinate vectors and components
$\boldsymbol{\xi}_i, \xi_i$	local coordinate vectors and components
$\boldsymbol{X} = (X_1, X_2, X_3)^T$	position vector in reference configuration
$\boldsymbol{x} = (x_1, x_2, x_3)^T$	position vector in current configuration
$\boldsymbol{N}_0$	normal vector in reference configuration
$\boldsymbol{n}$	normal vector in current configuration
θ^i	contravariant curvilinear coordinates
$\boldsymbol{d}$	shell unit director in current configuration
h	shell thickness in current configuration
$\boldsymbol{u}$	total displacement
$\boldsymbol{v}$	displacement of shell middle plane
$\boldsymbol{w}$	change of shell director
θ_α	rotation about α-axis
χ	change in thickness
$(\cdot)_{i,j} = \frac{\partial (\cdot)_i}{\partial (\cdot)_j}$	derivative of component i with respect to coordinate j
$(\cdot)_{,j}$	directional derivative
$\boldsymbol{I}$	identity
$\boldsymbol{H}$	displacement gradient
$\boldsymbol{F}$	deformation gradient
$\boldsymbol{C}$	right Cauchy-Green tensor
$\boldsymbol{b}$	left Cauchy-Green tensor
$\boldsymbol{E}$	Green-Lagrangian strain
$\boldsymbol{e}$	Euler-Almansi strain
$\boldsymbol{\varepsilon}$	strain
$\boldsymbol{\varepsilon}^m$	shell membrane strain
$\boldsymbol{\varepsilon}^l$	linear shell membrane strain
$\boldsymbol{\varepsilon}^{nl}$	non-linear shell membrane strain
$\boldsymbol{\varepsilon}^b$	shell bending strain
$\boldsymbol{\varepsilon}^s$	shell transverse shear strain
$\gamma_{12}, \gamma_{13}, \gamma_{23}$	shear strain components
$\boldsymbol{\sigma}$	Cauchy stress
$\boldsymbol{P}$	1^{st} Piola-Kirchhoff stress
$\boldsymbol{S}$	2^{nd} Piola-Kirchhoff stress
$\boldsymbol{N}$	in-plane stress resultants
$\boldsymbol{M}$	bending moments
$\boldsymbol{Q}$	transverse forces

Constitutive equations

Ψ	strain energy
I_I	scalar invariant
λ, λ_i	principal stretches
E	Young's modulus
ν	poisson ratio
C_{IJ}	Ogden material parameters
p	hydrostatic pressure
$\mathbb{C}$	constitutive tensor

FEM

Ω	computational domain
Γ	boundary of the computational domain
Γ_u, Γ_d	Dirichlet (displacement) and Neumann (traction) boundary, respectively
$(\cdot)$	quantity expressed in context-related coordinates
$\tilde{(\cdot)}$	quantity expressed in global coordinates
$\hat{(\cdot)}$	quantity expressed in element coordinates
$\bar{(\cdot)}$	quantity expressed in smoothing domain coordinates
Ω_I^e	domain occupied by element I
Ω_I^s	domain occupied by smoothing domain I
$\mathbf{\Phi}$	matrix of shape functions
$\mathbf{\Phi}^{enh}$	matrix of enhanced shape functions
$\mathbf{L}_1, \mathbf{L}_2$	helper matrices
$\mathbf{B}$	strain-displacement matrix
$\mathbf{K}^t$	tangent stiffness matrix
$\mathbf{K}$	material stiffness matrix
$\mathbf{G}$	geometrical stiffness matrix
$\mathbf{C}$	material matrix
$\mathbf{u}$	global displacement vector
$\mathbf{d}$	local displacement vector
$\mathbf{f}$	internal force vector
N_N	total number of nodes in mesh
N_e	total number of elements in mesh
N_s	total number of smoothing domains in mesh
N_n	number of nodes of a smoothing domain or an element (from context)
$\mathbf{B}_*^i$	local strain-displacement matrix of domain Ω_i related to a certain kind of strain
$\mathbf{R}_{*I}^{\alpha}$	rotation matrix

Electrophysiology

V_m	membrane action potential
I_*	ionic current
g_*	ionic gate
IC_{50}	half-inhibitory constant

Contents

List of Tables

List of Figures

1 Introduction

The human heart is a complex organ with a complicated anisotropic, heterogeneous microscopic and macroscopic structure. The complexity of the electromechanical processes and working mechanisms at the macroscopic level is relatively well understood compared to the microscopic level. Especially the electrophysiology of different types of native cardiomyocytes (CM) has a level of intricacy such that the current knowledge in this field must be viewed as incomplete. This limited knowledge is exemplarily illustrated by the fact that multiple hypotheses are still discussed concerning which biochemical process drives the autonomous pacemaking of the heart (Li et al. [90]). Although these processes are of major interest since the beginning of cardiovascular research, it still cannot be decided which one is preferable.

Despite this lack of knowledge in cardiac electrophysiology, the pharmaceutical industry develops and sells medication that is supposed to change specific biochemical processes more or less selectively in order to cure cardiac diseases. Regarding the fact that the cellular electrophysiology is far from completely understood one has to conclude that quantitative assessments, supposed selectivity and assumed compatibility of medication needs to be viewed with caution.

As it is in the sense of the patient's health, drug effects are investigated at the protein level, at the cellular level, in cell clusters, at tissue level and at organ level using various experimental setups and methods. All the setups and methods share the major issue that it is close to impossible to perform experiments on healthy native human CM *in vivo*. In the best case, diseased specimens from cadavers can be obtained in a very low sample size. One remedy often was and still is to perform animal testing which is not only ethically critical but mammalian cells of different species also differ in their electrophysiology which questions the cross-species translation.

As a further remedy, in 2006, Takahashi and Yamanaka presented the breakthrough technology of reprogramming adult somatic, i.e. fully differentiated cells to embryonic-like cells (Takahashi and Yamanaka [145]) which in general can be differentiated into any human cell. Since then, human-induced pluripotent stem cells (hiPSC) became a powerful tool not only for drug screening. Although today there are some cell types that are difficult to be derived from hiPS cells, hiPSC-derived cardiomyocytes (hiPSC-CM) are very commonly used in experimental setups all over the world because they are relatively cheap, reliably and infinitely reproducible, ethically nearly uncritical and they reproduce the prominent characteristics of native CM fairly well.

In the following years many groups started to investigate medicated hiPSC-CM performing patch clamp experiments (e.g. Liang et al. [92]), fluorescent imaging (e.g. Sirenko et al. [140]), using multi-electrode arrays (e.g. Harris et al. [68]) or (electro-)mechanical testing (e.g. Grosberg et al. [64], Nawroth et al. [111] and Agarwal et al. [2]). Mechanical testing of hiPSC-CM monolayers and tissues is also performed in the Lab of Medical and Molecular Biology at Aachen University of Applied Sciences (Linder et al. [93]). There, the so-called CellDrum system, an inflatable thin silicone membrane with cultivated myocardial tissue, provides mechanical quanti-

ties that one can investigate and evaluate in order to determine the contractility of cells and the effect of drugs on them (Trzewik et al. [152] and Trzewik [151]). This way macroscopic information about the cardiac tissue being investigated is obtained. Even more interesting than those information is the question: 'How do the drugs act on the gates that activate and inactivate cellular ion channels?' because this is the level where medication changes the cellular processes.

For this purpose this thesis aims to build and employ a computational model for cardiac tissue and drug action. Simulating cardiac tissue or even the human heart is an interdisciplinary task as special knowledge in biology, medicine, cardiology, chemistry, biochemistry, cell culturing, microscopy, electrophysiology, mechanics, electromechanics, neurology, computer science and mathematics is required. The need for computational models in this field is evident due to multiple reasons:

- Experiments are very expensive, time consuming and they require a lot of manpower. Often a long trial and error phase is needed to build an experimental setup and to perform special experiments.
- Replacing some experiments by parametric simulations also reduces the amount of unethical or at least ethically questionable animal testing.
- Besides experiments on hiPSC-CM, animal testing is the only way to produce data. Of course the hearts of different animal species differ from that of a human. Transferring the results to a human heart can be facilitated by simulations.
- Simulations can enhance the information that is gathered from experiments and thereby increase the benefit from each individual experiment.
- Simulations may help to understand individual differences or deviating behavior of isolated cells, cell clusters, monolayers, 3D tissues and organs.
- Performing simulations prior to the construction of an experimental setup or the conduction of experiments can reveal helpful advice how to build the setup or how to perform the experiment.
- Simulations based on literature data serve as validation for own experimental results.
- In view of personalized medicine, computational models might be able to predict the effects and side-effects of medical treatment on person-specific cardiac cells with only very little experimental data that has to be determined.

There is a strong community currently building models for the electrophysiology of individual cardiac cells (e.g. ten Tusscher and Panfilov [146], Chandler et al. [23] and Paci et al. [122]), the electromechanical behavior of cardiac tissue (e.g. Böl et al. [15], Göktepe and Kuhl [59] and Göktepe et al. [61]), the mechano-electrical feedback, the pathologies of the heart (Genet et al. [58]), the electrical propagation through the whole heart and tissues (e.g. Nash and Panfilov [110], Göktepe and Kuhl [59] and Weise and Panfilov [156]) and drug action (e.g.

Obiol-Pardo et al. [121]). All models suffer from the fact that reliable experimental data is difficult to obtain. Experimental results depend on a lot of influences like the experimental setup, the cell type, the species, the cell production batch, the maturity of the cells and their health condition. In total there are a lot of factors that can hardly be measured, controlled or quantified during an experiment. Thus, developing or choosing an appropriate model for a specific application often is very difficult and choices should be made with caution.

This thesis builds and investigates a model for very thin cardiac tissue constructs, so-called 2D tissue, that consist of a collagen matrix seeded with hiPSC-CM. All parts of the finite element model are explained in detail. Concerning the employed experimental data, be it own data or literature data, all choices become justified and explained including an evaluation of the quality of the available data. Special attention is drawn on the comparison of experimental data of drug action on a cardiac tissue construct from an inflation test called CellDrum with simulations. This setup has been developed in the Lab of Medical and Molecular Biology at Aachen University of Applied Sciences. The comparison of experiments and simulations reveals modeling deficiencies that clearly show necessary improvements. Nevertheless, the qualitatively good results presented in this thesis are very promising regarding the prediction of the patient-specific response of cardiac tissue to drug treatment.

Mathematically, the problem can be separated into a global and a local problem. The local problem comprises the cellular electrophysiology and the excitation-contraction coupling that are formulated in terms of systems of ordinary differential equations. The global mechanical problem is stated in terms of a partial differential equation that is solved numerically using the FEM. Within this thesis the standard FEM as well as the so-called smoothed FEM are employed. The latter method proves to be very suitable for simulations in biomechanical applications.

In section 2 the reader gets a quick introduction into continuum mechanics, existing plate and shell theories and the nonlinear FEM. The following section 3 introduces into the smoothed FEM that has been used for many of the simulations and that is especially useful in future applications. Section 4 introduces into the electrophysiology of cardiac cells before section 5 draws attention on the material modeling of cardiac tissue and specifically on the proper modeling of the cellular electrophysiology of cardiomyocytes. In section 6 the inflation setup is explained before the whole finite element model becomes summed up in section 7. The final two sections 8 and 9 present implementational details and results as well as a conclusion and outlook.

2 Continuum Mechanics and FEM

This chapter is intended to introduce the basic ideas of continuum mechanics, plates and the FEM as far as needed to explain the contents of this thesis. For details each section refers to special literature on the respective topic. The notation that is used throughout the thesis is also explained in the following sections. In this thesis both, the symbolic as well as the index notation of tensors, are used.

2.1 Continuum Mechanics

This section mainly bases on the standard text book Holzapfel [72] and on the introduction into Continuum Mechanics in Willner [157].

A material point $\boldsymbol{X}$, as illustrated in fig. 2.1, can be referred to either with respect to the reference (undeformed) configuration B_0 using the coordinate vector

$$\boldsymbol{X} = \boldsymbol{\chi}^{-1}(\boldsymbol{x}, t) \; , \tag{2.1}$$

with $\boldsymbol{\chi}$ being the movement of particle X and the time t or with respect to the current (deformed) configuration B using

$$\boldsymbol{x} = \boldsymbol{\chi}(\boldsymbol{X}, t) \; , \tag{2.2}$$

the coordinate vector to the current position of the particle in the physical space. The displacement $\boldsymbol{u}(\boldsymbol{x}, t)$ is simply defined by the difference of the position vectors of a particle in both configurations

$$\boldsymbol{u} = \boldsymbol{x} - \boldsymbol{X} \; . \tag{2.3}$$

A basic deformation measure between B_0 and B is the deformation gradient

$$\boldsymbol{F} = \frac{\partial \boldsymbol{\chi}(\boldsymbol{X}, t)}{\partial \boldsymbol{X}} = \frac{\partial \boldsymbol{x}}{\partial \boldsymbol{X}} \; , \tag{2.4}$$

that maps a line element $d\boldsymbol{X}$ in the reference configuration onto a line element $d\boldsymbol{x}$ in the current configuration

$$d\boldsymbol{x} = \boldsymbol{F} d\boldsymbol{X} \; . \tag{2.5}$$

It can be expressed in terms of the displacement gradient as

$$\boldsymbol{F} = \frac{\partial \boldsymbol{u}}{\partial \boldsymbol{X}} + \boldsymbol{I} = \operatorname{Grad} \boldsymbol{u} + \boldsymbol{I} \; , \tag{2.6}$$

Based on eq. (2.5) one can derive that a reference area element $d\boldsymbol{A}$ can be mapped to a current area element $d\boldsymbol{a}$ by Nanson's formula

$$d\boldsymbol{a} = \boldsymbol{n} da = J \boldsymbol{F}^{-T} \boldsymbol{N}_0 dA = J \boldsymbol{F}^{-T} d\boldsymbol{A} \; , \tag{2.7}$$

using the unit normal vectors $\boldsymbol{N}_0$ and $\boldsymbol{n}$ of the area elements in the reference and current configuration, respectively and the determinant of $\boldsymbol{F}$,

$$J = det \boldsymbol{F} \; . \tag{2.8}$$

The Jacobian determinant J $(0 < J < \infty)$ determines the volume change between a volume element dV in B_0 and a volume element dv in B

$$dv = JdV \ . \tag{2.9}$$

Equations (2.5),(2.7) and (2.9) are called the transport theorems for line, area and volume elements, respectively and are illustrated in fig. 2.2.

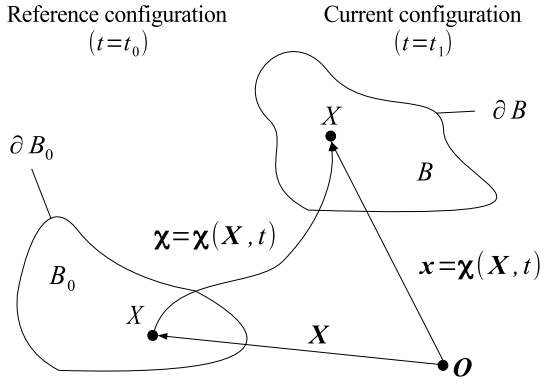

Figure 2.1: Movement of a particle in material and physical coordinates

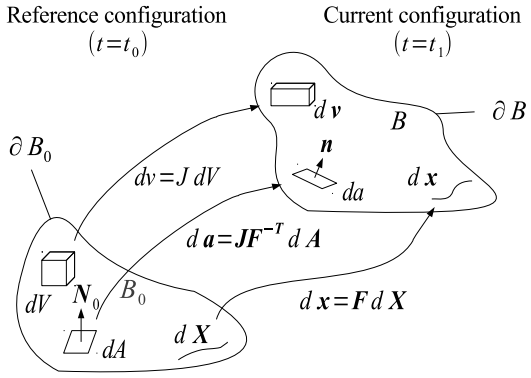

Figure 2.2: Transport theorems

2.1.1 Strain

As $\boldsymbol{F}$ is the most basic deformation measure, the other strain measures are defined on its basis. The right Cauchy-Green tensor

$$\boldsymbol{C} = \boldsymbol{F}^T\boldsymbol{F} \tag{2.10}$$

for instance determines the configurational change of the scalar product of two vectors $\boldsymbol{x}_1$ and $\boldsymbol{x}_2$,

$$d\boldsymbol{x}_1 \cdot d\boldsymbol{x}_2 = d\boldsymbol{X}_1 \cdot \boldsymbol{F}^T\boldsymbol{F}d\boldsymbol{X}_2 = d\boldsymbol{X}_1 \cdot \boldsymbol{C}d\boldsymbol{X}_2 \ . \tag{2.11}$$

The inverse operation is accomplished by $\boldsymbol{b}^{-1}$, where

$$\boldsymbol{b} = \boldsymbol{F}\boldsymbol{F}^T \tag{2.12}$$

is the left Cauchy-Green tensor. For details on these and other kinematic tensors the reader is directed to Bonet and Wood [18]. A commonly used, reference configuration based strain measure is the Cauchy-Green strain tensor

$$\boldsymbol{E} = \frac{1}{2}(\boldsymbol{F}^T\boldsymbol{F} - \boldsymbol{I}) = \frac{1}{2}(\boldsymbol{C} - \boldsymbol{I}) \ , \tag{2.13}$$

which is often expressed in terms of the displacement gradient using eq. (2.6)

$$\begin{aligned} \boldsymbol{E} &= \frac{1}{2}(\boldsymbol{F}^T\boldsymbol{F} - \boldsymbol{I}) = \frac{1}{2}((\mathrm{Grad}\,\boldsymbol{u} + \boldsymbol{I})^T(\mathrm{Grad}\,\boldsymbol{u} + \boldsymbol{I}) - \boldsymbol{I}) \\ &= \frac{1}{2}(\mathrm{Grad}^T\boldsymbol{u} + \mathrm{Grad}\,\boldsymbol{u} + \mathrm{Grad}^T\boldsymbol{u}\mathrm{Grad}\,\boldsymbol{u}) \ . \end{aligned} \tag{2.14}$$

Ignoring the quadratic contribution in eq. (2.14) gives the linear part of the strain

$$\operatorname{Lin} \boldsymbol{E} = \frac{1}{2}(\operatorname{Grad}^T \boldsymbol{u} + \operatorname{Grad} \boldsymbol{u}) = \operatorname{sym}(\operatorname{Grad} \boldsymbol{u}) \ , \tag{2.15}$$

which is the symmetric part of the displacement gradient. This part purely refers to deformation whereas the additive skew-symmetric part refers to the rotational part of the tensor.

Applying the so-called covariant *push-forward* operation $\boldsymbol{F}^{-T}(\bullet)\boldsymbol{F}^{-1}$ that transforms a quantity given in the reference configuration into the current configuration leads to the Euler-Almansi strain tensor

$$\boldsymbol{e} = \boldsymbol{F}^{-T}\boldsymbol{E}\boldsymbol{F}^{-1} = \frac{1}{2}(\boldsymbol{I} - \boldsymbol{b}^{-1}) \ . \tag{2.16}$$

The inverse operation to a covariant *push-forward* is the covariant *pull-back* operation $\boldsymbol{F}^T(\bullet)\boldsymbol{F}$.

2.1.2 Stress

Cauchy's fundamental lemma

$$\boldsymbol{t} = \boldsymbol{\sigma}\boldsymbol{n} \tag{2.17}$$

states that the stress vector $\boldsymbol{t}$ is defined by a linear mapping of the outward normal vector $\boldsymbol{n}$, namely the Cauchy (or true) stress $\boldsymbol{\sigma}$ operating on $\boldsymbol{n}$. Applying $\boldsymbol{t}$ to the area da leads to

$$d\boldsymbol{f} = \boldsymbol{t}da = \boldsymbol{\sigma}\boldsymbol{n}da = \boldsymbol{\sigma}d\boldsymbol{a} \ , \tag{2.18}$$

with $d\boldsymbol{f}$ being a true force applied to the current area element $d\boldsymbol{a}$. The benefit of introducing $\boldsymbol{\sigma}$ is that it does not contain information about the orientation, like the stress vector. Proper handling of the stress vector requires the knowledge of $\boldsymbol{n}$, whereas the Cauchy stress can be computed independent of the normal to the area element. From eq. (2.18) one derives the first Piola-Kirchhoff stress tensor by using the transport theorem (2.7)

$$d\boldsymbol{f} = \boldsymbol{\sigma}J\boldsymbol{F}^{-T}d\boldsymbol{A} \ . \tag{2.19}$$

Thus the first Piola-Kirchhoff stress tensor

$$\boldsymbol{P} = \boldsymbol{\sigma}J\boldsymbol{F}^{-T} \tag{2.20}$$

can be interpreted as the actual force applied to an area element in the reference configuration. Of course it is possible to transform the force itself to the reference configuration too which leads to

$$\boldsymbol{S} = \boldsymbol{F}^{-1}\boldsymbol{P} = J\boldsymbol{F}^{-1}\boldsymbol{\sigma}\boldsymbol{F}^{-T} \ , \tag{2.21}$$

the second Piola-Kirchhoff stress tensor that represents a force mapped to the reference configuration and applied to the reference configuration. $\boldsymbol{S}$ is often preferred because it is a symmetric tensor, unlike $\boldsymbol{P}$.

Stress and strain can be related via a fourth-order constitutive tensor $\mathbb{C}$

$$\boldsymbol{\Sigma} = \mathbb{C}(t, T, \boldsymbol{\varepsilon}, \boldsymbol{\alpha})\boldsymbol{\varepsilon} \tag{2.22}$$

that might be dependent on the time t, the temperature T, the strain $\boldsymbol{\varepsilon}$ or other parameters $\boldsymbol{\alpha}$. Throughout this thesis Voigt's notation of symmetric stress and strain tensors will be used, i.e.

$$\begin{aligned} \boldsymbol{\Sigma} &= (\Sigma_{11}, \Sigma_{22}, \Sigma_{33}, \Sigma_{12}, \Sigma_{13}, \Sigma_{23})^T \text{ and} && (2.23)\\ \boldsymbol{\varepsilon} &= (\varepsilon_{11}, \varepsilon_{22}, \varepsilon_{33}, 2\varepsilon_{12}, 2\varepsilon_{13}, 2\varepsilon_{23})^T && (2.24)\\ &= (\varepsilon_{11}, \varepsilon_{22}, \varepsilon_{33}, \gamma_{12}, \gamma_{13}, \gamma_{23})^T \ , && (2.25) \end{aligned}$$

with γ_{ij} being the shear strains and $\boldsymbol{\Sigma}$ and $\boldsymbol{\varepsilon}$ representing any conjugate stress and strain tensors. A stress-strain pair $(\boldsymbol{\Sigma}, \boldsymbol{\varepsilon})$ is termed (work) conjugate if their double contraction equals the internally stored energy Ψ:

$$\boldsymbol{\Sigma} : \boldsymbol{\varepsilon} = \Psi \ . \tag{2.26}$$

In the given notation the fourth-order constitutive tensor $\mathbb{C}$ is a square matrix.

2.2 Plate and Shell Theories

Plate and shell models are used to describe the kinematics of very thin bodies, whose lateral dimension l is much larger than its thickness h, i.e.

$$l >> h \ . \tag{2.27}$$

A full three-dimensional discretization of such a plate either leads to very high length-thickness ratios or an unreasonably large number of elements, depending on whether it is a coarse or a fine mesh. In the former case one observes numerical locking whereas the latter case leads to a highly increased number of degrees of freedom resulting in increased computation time and increased memory consumption. In order to avoid those circumstances one degenerates the three-dimensional model into a middle plane with a thickness h. A local, generally curvilinear coordinate system $\boldsymbol{\xi} = [\xi_1, \xi_2, \xi_3]$ is attached to this middle plane as shown in fig. 2.3, with in-plane coordinates ξ_1 and ξ_2, and ξ_3 being the coordinate normal to the middle plane. If not otherwise stated, in this thesis, $\boldsymbol{\xi}$ is always a Cartesian basis system because the developments herein are mainly based on plane plate models. In the case of shells one would switch to local curvilinear coordinates in order to properly take into account the curvature of the shell geometry.

Due to the contents of the thesis the term *plate* is used rather than the term *shell* although all the concepts may be applied to shells too. The basic kinematic quantities of standard plate and shell formulations are shown in fig. 2.3. The displacement $\boldsymbol{u}(\xi_1, \xi_2, \xi_3) = [u_1, u_2, u_3]^T$ of any point of the shell in general varies in thickness direction and depends on the translation $\boldsymbol{v}(\xi_1, \xi_2) = [v_1, v_2, v_3]^T$ of the shell middle plane $\boldsymbol{E}(\xi_1, \xi_2, \xi_3 = 0)$ and on its rotation in point $(\xi_1, \xi_2, 0)$, termed $\boldsymbol{w}(\xi_1, \xi_2) = [w_1, w_2]^T = [\theta_2, -\theta_1]^T$.

2.2.1 Plate Models

In order to simplify the very general descripton of plates, different theories of varying complexity have been introduced that are depicted in fig. 2.4 with respect to a beam example (cross-section of a plate). The beam is clamped on its left end and on its right end a moment M is applied.

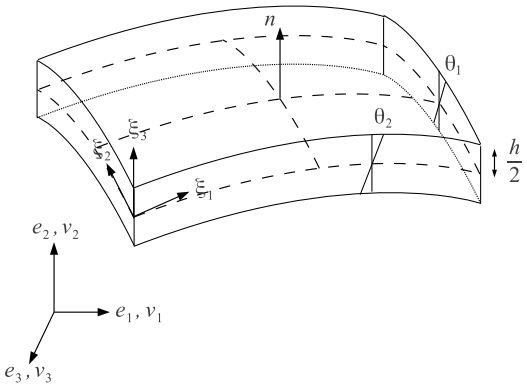

Figure 2.3: Global and local coordinate systems $\boldsymbol{e}$ and $\boldsymbol{\xi}$, displacements v_i, rotations w_α and normal $\boldsymbol{n}$

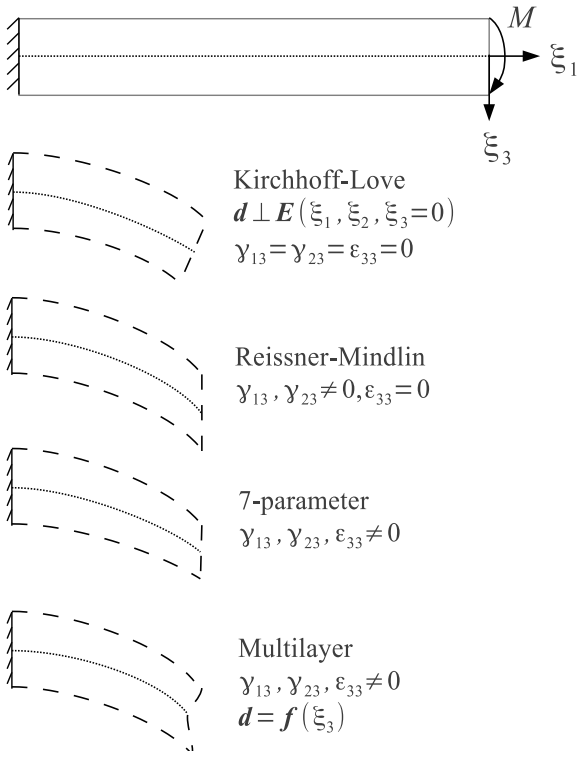

Figure 2.4: Plate theories

First of all the *Kirchhoff-Love* theory assumes that lines that initially are normal to the plate middle plane remain normal, i.e. the shell director $\boldsymbol{d}$ that is attached to the middle plane remains normal, shear strains are zero and it assumes constant thickness. Allowing for transverse shear strains leads to so-called *Reissner-Mindlin* plates that usually assume a linearly varying displacement field in thickness direction ξ_3

$$\boldsymbol{u} = \boldsymbol{v} + \xi_3 \boldsymbol{w} \ , \tag{2.28}$$

which can be written in detail for a local coordinate system $\boldsymbol{\xi} = [\xi_1, \xi_2, \xi_3]$ tangential to the plate middle plane,

$$u_1(\xi_1, \xi_2, \xi_3) = v_1(\xi_1, \xi_2) + \xi_3 \theta_2(\xi_1, \xi_2) \tag{2.29}$$

$$u_2(\xi_1, \xi_2, \xi_3) = v_2(\xi_1, \xi_2) - \xi_3 \theta_1(\xi_1, \xi_2) \tag{2.30}$$

$$u_3(\xi_1, \xi_2, \xi_3) = v_3(\xi_1, \xi_2) \ . \tag{2.31}$$

In both, the *Kirchhoff-Love* and the *Reissner-Mindlin* theory, the so-called *Kirchhoff* constraint, $\varepsilon_{33} = 0$, leads to an inconsistency. Assuming plane stress, i.e. $\sigma_{33} = 0$, which is

a common assumption for the thin plate limit, one normally would be able to determine ε_{33} from the constitutive eq. (2.22). The resulting non-zero thickness strain contradicts the Kirchhoff constraint.

Consequently the next step in complexity of the formulation is the drop of the constraint $\varepsilon_{33} = 0$ to get rid of this inconcistency. The so-called *7-parameter* model introduces two new parameters into the variational form, namely the constant thickness strain χ and a strain component β_{33} that is linear in ξ_3 to get a linearly varying thickness strain. The variational form then is a three-field Hu-Washizu functional as described in sect. 2.3.4.1. As β_{33} is introduced using the *Enhanced Assumed Strain* technique and therefore does not need to be compatible, its parameters can be eliminated on element level. In fact the *7-parameter* model ends up with a two-field functional as described in sect. 2.3.4.2. Plate and shell formulations including thickness strain have already been the topic of many researchers and detailed explanations of the concept of *7-parameter* models and the *Enhanced Assumed Strain* technique can be found in Simo et al. [138], Simo and Armero [139], Büchter [21], Büchter et al. [22], Roehl [129], Betsch et al. [11], Bischoff [13], Miehe and Schröder [106] and Koschnick [85], to name only a selection. Those shell models share the benefit of being able to use full three-dimensional constitutive laws for the shell without modification.

The last degree of complexity that is shown in fig. 2.4 is a nonlinear director $\boldsymbol{d}$ leading to *multilayer* models. For details the reader is referred to Eckstein [46].

2.2.2 Reissner-Mindlin Plates in Detail

The Reissner-Mindlin plate theory is sufficiently accurate for the applications investigated in this thesis. Figure 2.5 shows the stress resultants of a unit volume of a plate with respect to this theory. The stress resultants are

$$\boldsymbol{N} = \begin{pmatrix} N_{11} \\ N_{22} \\ N_{12} \end{pmatrix} = \int_{-\frac{h}{2}}^{\frac{h}{2}} \begin{pmatrix} \sigma_{11} \\ \sigma_{22} \\ \sigma_{12} \end{pmatrix} d\xi_3 \,, \tag{2.32}$$

$$\boldsymbol{M} = \begin{pmatrix} M_{11} \\ M_{22} \\ M_{12} \end{pmatrix} = \int_{-\frac{h}{2}}^{\frac{h}{2}} \xi_3 \begin{pmatrix} \sigma_{11} \\ \sigma_{22} \\ \sigma_{12} \end{pmatrix} d\xi_3 \,, \tag{2.33}$$

$$\boldsymbol{T} = \begin{pmatrix} T_1 \\ T_2 \end{pmatrix} = \int_{-\frac{h}{2}}^{\frac{h}{2}} \begin{pmatrix} \sigma_{13} \\ \sigma_{23} \end{pmatrix} d\xi_3 \,, \tag{2.34}$$

with $\boldsymbol{N}, \boldsymbol{M}$ and $\boldsymbol{T}$ the axial forces, bending moments and transversal shear forces, respectively.

Therefore the strains are introduced as follows

$$\boldsymbol{\varepsilon} = (\varepsilon_{11}, \varepsilon_{22}, \gamma_{12}, \gamma_{13}, \gamma_{23})^T = \begin{pmatrix} \boldsymbol{\varepsilon}^m \\ 0 \end{pmatrix} + \begin{pmatrix} \xi_3 \boldsymbol{\varepsilon}^b \\ 0 \end{pmatrix} + \begin{pmatrix} 0 \\ \boldsymbol{\varepsilon}^s \end{pmatrix} \,, \tag{2.35}$$

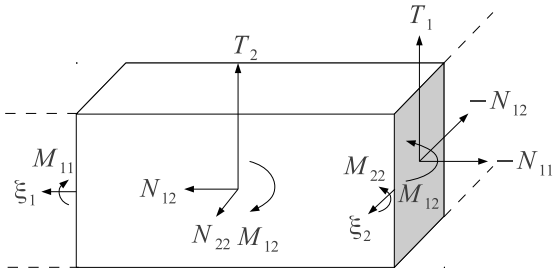

Figure 2.5: Axial forces, bending moments and transversal shear

where the membrane and bending parts, $\boldsymbol{\varepsilon}^m$ and $\boldsymbol{\varepsilon}^b$, respectively, contribute to the in-plane strain components and the transverse shear part $\boldsymbol{\varepsilon}^s$ determines γ_{13} and γ_{23}. The membrane strain part reads as

$$\boldsymbol{\varepsilon}^m = \boldsymbol{\varepsilon}^l + \boldsymbol{\varepsilon}^{nl} = \begin{pmatrix} v_{1,1} \\ v_{2,2} \\ v_{1,2} + v_{2,1} \end{pmatrix} + \begin{pmatrix} \frac{1}{2}(v_{3,1})^2 \\ \frac{1}{2}(v_{3,2})^2 \\ v_{3,1} v_{3,2} \end{pmatrix} , \tag{2.36}$$

and in turn can be split into a linear and a nonlinear part. The nonlinear part accounts for the geometrical nonlinearity that arises from the assumption of large displacements. The linear bending and transverse shear parts read as

$$\boldsymbol{\varepsilon}^b = \begin{pmatrix} w_{1,1} \\ w_{2,2} \\ w_{1,2} + w_{2,1} \end{pmatrix} \text{ and } \boldsymbol{\varepsilon}^s = \begin{pmatrix} v_{3,1} + w_1 \\ v_{3,2} + w_2 \end{pmatrix} . \tag{2.37}$$

More details on plate and shell models and their applications in the FEM can be found for instance in Chapelle and Bathe [24] and Zienkiewicz and Taylor [167].

2.3 Finite Element Method

The Finite Element Method (FEM) is the most widely used numerical method for the simulation of a vast amount of - possibly coupled - field problems in mechanics, acoustics, fluid mechanics, biomechanics, electro-magnetism, thermodynamics and many more that can be described by partial differential equations, particularly by elliptic and parabolic ones. In consequence the amount of books written on this topic is huge and there are countless other publications concerning FEM. Some influential books on FEM with respect to this thesis are Zienkiewicz [165], Crisfield [34], Crisfield [35], Zienkiewicz and Taylor [166], Zienkiewicz and Taylor [167] and Bathe [6].

2.3.1 The Principle of Virtual Displacements

In elasticity the problem to be solved is given in its differential form as

$$\begin{aligned} \operatorname{div}\boldsymbol{\sigma} + \boldsymbol{f} &= 0 \text{ in } \Omega \,, & (2.38)\\ \boldsymbol{u} &= \boldsymbol{u}_0 \text{ on } \Gamma_u \,, & (2.39)\\ \boldsymbol{\sigma}\boldsymbol{n} &= \boldsymbol{t}_0 \text{ on } \Gamma_d \,, & (2.40) \end{aligned}$$

where eq. (2.38) is called the global balance of momentum and states the equilibrium of internal forces and external forces $\boldsymbol{f}$. Both, $\boldsymbol{f}$ and the unknown displacement field $\boldsymbol{u}$ need to be twice continuously differentiable. In addition, $\boldsymbol{u}$ has to fullfill the (essential) Dirichlet boundary conditions (2.39) and the (natural) Neumann boundary conditions (2.40). Robin (Newton) boundary conditions are a mixed kind and thus can be neglected here for simplicity. Equivalent formulations of this problem are the variational formulation and the herein employed principle of virtual displacements. Details on all formulations can be found for instance in Bathe [6].

The principle of virtual displacements can be derived from the differential form by multiplication with a test function $\delta\boldsymbol{u}$ and integration, i.e.

$$\int_\Omega \operatorname{div}\boldsymbol{\sigma} \cdot \delta\boldsymbol{u}\, d\boldsymbol{x} + \int_\Omega \boldsymbol{f} \cdot \delta\boldsymbol{u}\, d\boldsymbol{x} = 0 \,, \tag{2.41}$$

which, using the symmetry of the stress tensor $\boldsymbol{\sigma} = \boldsymbol{\sigma}^T$, can be expanded to

$$\int_\Omega \operatorname{div}(\boldsymbol{\sigma} \cdot \delta\boldsymbol{u})\, d\boldsymbol{x} - \int_\Omega \boldsymbol{\sigma} \cdot \operatorname{grad}\delta\boldsymbol{u}\, d\boldsymbol{x} + \int_\Omega \boldsymbol{f} \cdot \delta\boldsymbol{u}\, d\boldsymbol{x} = 0 \,. \tag{2.42}$$

The test function $\delta\boldsymbol{u} := \epsilon\boldsymbol{\eta}$ is called the variation of $\boldsymbol{u}$ and is a non-zero function that has similar properties like $\boldsymbol{u}$ besides that it vanishes on Γ. In the limit case, by construction,

$$\lim_{\epsilon\to 0}(\boldsymbol{u} + \delta\boldsymbol{u}) = \lim_{\epsilon\to 0}(\boldsymbol{u} + \epsilon\boldsymbol{\eta}) = \boldsymbol{u} \,, \tag{2.43}$$

holds. Application of the divergence theorem to the first term in eq. (2.42) leads to

$$\int_{\Gamma_d} \boldsymbol{\sigma}\boldsymbol{n} \cdot \delta\boldsymbol{u}\, ds - \int_\Omega \boldsymbol{\sigma} \cdot \delta\boldsymbol{\varepsilon}\, d\boldsymbol{x} + \int_\Omega \boldsymbol{f} \cdot \delta\boldsymbol{u}\, d\boldsymbol{x} = 0 \,, \tag{2.44}$$

where the symmetry of the stress tensor has been used again to get the equality $\operatorname{grad}\delta\boldsymbol{u} = \delta\boldsymbol{\varepsilon}$ which is generally not true if $\boldsymbol{\sigma}$ were asymmetric. By rearranging one finally derives the principle of virtual displacements or the weak form of the differential formulation as

$$\int_\Omega \boldsymbol{\sigma} \cdot \delta\boldsymbol{\varepsilon}\, d\boldsymbol{x} = \int_\Omega \boldsymbol{f} \cdot \delta\boldsymbol{u}\, d\boldsymbol{x} + \int_{\Gamma_d} \boldsymbol{\sigma}\boldsymbol{n} \cdot \delta\boldsymbol{u}\, ds \,, \tag{2.45}$$

Finally inserting the constitutive relation (2.22) between stress and strain, the Neumann boundary condition (2.40) and switching to Voigt's notation as introduced in sect. 2.1.2 leads to

$$\int_\Omega \delta\boldsymbol{\varepsilon}^T \mathbb{C}\boldsymbol{\varepsilon}\, d\boldsymbol{x} = \int_\Omega \delta\boldsymbol{u}^T \boldsymbol{f}\, d\boldsymbol{x} + \int_{\Gamma_d} \delta\boldsymbol{u}^T \boldsymbol{t}_0\, ds \,. \tag{2.46}$$

The Dirichlet boundary conditions (2.39) are enforced globally and do not show up in the weak form (2.46). The main difference of the weak form to the differential form is that the unknown $\boldsymbol{u}$ needs to be only continuously differentiable now, i.e. $\boldsymbol{u}$ lies in the Sobolev space

$$H^1(\Omega) = \{\boldsymbol{u} | D^{\boldsymbol{\alpha}} \boldsymbol{u} \in L^2(\Omega), ||\boldsymbol{\alpha}|| \leq 1\}, \tag{2.47}$$

with $D^{\boldsymbol{\alpha}}$ the differential operator for all spatial dimensions indicated by $\boldsymbol{\alpha} = \{\alpha_1, ..., \alpha_n\}$ and the Hilbert space

$$L^2(\Omega) = \{\boldsymbol{u} | \int_\Omega \boldsymbol{u}^2 d\Omega < \infty\} \tag{2.48}$$

of all square integrable functions. Summarizing this the function space of the solution is

$$\mathcal{S} = \{\boldsymbol{u} | \boldsymbol{u} \in H^1(\Omega), \boldsymbol{u}|_{\Gamma_u} = \boldsymbol{u}_0, \boldsymbol{\sigma}\boldsymbol{n}|_{\Gamma_d} = \boldsymbol{t}_0\} \ . \tag{2.49}$$

The function space of $\delta\boldsymbol{u}$ is similar but as already indicated, the function vanishes on Γ. Due to the lower requirements, the principle of virtual displacements and variational approaches are called weak forms whereas the differential form is called the strong form.

2.3.2 Variational Formulation

Although the formulations are fully equivalent, the variational formulation is shortly summarized here in order to provide the basics to show the variational consistency of S-FEM in sect. 3.2. Keeping in mind that the boundary conditions need to be fulfilled, the functional Π, being an energy potential, for a general problem can be written in the form

$$\Pi(\boldsymbol{u}) = \int_\Omega f\left(\boldsymbol{x}, \boldsymbol{u}, \frac{\partial \boldsymbol{u}}{\partial \boldsymbol{x}}\right) d\boldsymbol{x} \ . \tag{2.50}$$

It can be shown that the differential formulation is equivalent to the minimization of Π. The necessary condition for the functional to be minimal is that its first variation equals zero, i.e.

$$\delta\Pi(\boldsymbol{u}) = \left.\frac{d}{d\epsilon}\Pi(\boldsymbol{u} + \epsilon\boldsymbol{\eta})\right|_{\epsilon=0} = \lim_{\epsilon\to 0}\frac{1}{\epsilon}(\Pi(\boldsymbol{u} + \epsilon\boldsymbol{\eta}) - \Pi(\boldsymbol{u})) \stackrel{!}{=} 0 \ , \tag{2.51}$$

where the test function $\epsilon\boldsymbol{\eta}$ appears again.

2.3.3 Discretization

In order to solve the global eq. (2.45) FEM discretizes the computational domain Ω into N_E finite elements Ω_i^e, with $i = 1, ..., N_E$ based on N_N nodes. For the derivation of the element equations a linear two-dimensional problem is addressed in order to keep it simple. The derivation of the equations for three-dimensional problems is straightforward and can be found in Bathe [6]. The equations for plate problems will be shown in chap. 3.

Based on a discretization the local version of eq. (2.45) in Voigt's notation reads as

$$\int_{\Omega^e} \delta\boldsymbol{\varepsilon}^T \boldsymbol{\sigma} \, d\boldsymbol{x} = \int_{\Omega^e} \delta\boldsymbol{u}^T \boldsymbol{f} \, d\boldsymbol{x} + \int_{\Gamma_d^e} \delta\boldsymbol{u}^T \boldsymbol{t}_0 \, ds \ . \tag{2.52}$$

By using the constitutive equation (2.22) as in eq. (2.46) and by switching to matrix notation eq. (2.52) can be rewritten

$$\int_{\Omega^e} \delta\mathbf{u}^T \mathbf{L}^T \mathbf{C}\mathbf{L}\mathbf{u}\, d\mathbf{x} = \int_{\Omega^e} \delta\mathbf{u}^T \mathbf{f}\, d\mathbf{x} + \int_{\Gamma_d^e} \delta\mathbf{u}^T \mathbf{t}_0\, d\mathrm{s}\ , \tag{2.53}$$

with the differential operator

$$\mathbf{L} = \begin{bmatrix} \frac{\partial}{\partial x_1} & 0 \\ 0 & \frac{\partial}{\partial x_2} \\ \frac{\partial}{\partial x_2} & \frac{\partial}{\partial x_1} \end{bmatrix} \tag{2.54}$$

and the constitutive matrix $\mathbf{C}$.

Up to here the field $\mathbf{u}$ is an element of the function space $\mathcal{S}^h \subset \mathcal{S}$, cf. eq. (2.49), which only contains the admissible functions regarding the discretization. Applying the Galerkin method, specific nodal shape functions Φ_I are chosen to avoid searching for a solution in the whole space $\mathcal{S}^h$. Denoting N_n the number of nodes of an element, the discrete displacement field and its variation can then be written on element level

$$\mathbf{u}^e(\mathbf{x}) = \sum_{I=1}^{N_n} \Phi_I(\mathbf{x})\mathbf{d}_I\ , \tag{2.55}$$

$$\delta\mathbf{u}^e(\mathbf{x}) = \sum_{I=1}^{N_n} \Phi_I(\mathbf{x})\delta\mathbf{d}_I\ , \tag{2.56}$$

where the nodal shape functions Φ_I have compact support on the respective element only and are applied to the respective nodal displacement vector $\mathbf{d}_I$. Summing up the contributions of all N_N nodes of the finite element mesh, one gets the global discrete displacement field $\mathbf{u}^h$.

Herein the same shape functions for $\mathbf{u}^e$ and $\delta\mathbf{u}^e$ are used (Bubnov-Galerkin method) although this is generally not required (Petrov-Galerkin method). For convenience the position vector $\mathbf{x}^e$ is represented in the same way as $\mathbf{u}^e$ using the same shape functions. This approach is called the isoparametric concept. The application of the differential operator $\mathbf{L}$ to obtain the local strain field is straightforward

$$\boldsymbol{\varepsilon}^e = \mathbf{L}\mathbf{u}^e(\mathbf{x}) = \sum_{I=1}^{N_n} \mathbf{L}\Phi_I(\mathbf{x})\mathbf{d}_I = \sum_{I=1}^{N_n} \mathbf{B}_I(\mathbf{x})\mathbf{d}_I\ , \tag{2.57}$$

with the nodal strain-diplacement matrix $\mathbf{B}_I$ containing the derivates of the shape functions. Using $\mathbf{B} = [\mathbf{B_1}, ..., \mathbf{B_{N_n}}]$, $\mathbf{d}^e = [\mathbf{d_1}, ..., \mathbf{d_{N_n}}]^T$, $\delta\mathbf{d}^e = [\delta\mathbf{d_1}, ..., \delta\mathbf{d_{N_n}}]^T$, $\boldsymbol{\Phi} = [\Phi_1, ..., \Phi_{N_n}]$ and the divergence theorem to integrate the boundary condition over the boundary only, eq. (2.53) can be reexpressed as

$$(\delta\mathbf{d}^e)^T \int_{\Omega^e} \mathbf{B}^T\mathbf{C}\mathbf{B}\mathbf{d}^e\, d\mathbf{x} = (\delta\mathbf{d}^e)^T \int_{\Omega^e} \boldsymbol{\Phi}^T\mathbf{f}\, d\mathbf{x} + (\delta\mathbf{d}^e)^T \int_{\Gamma_d} \boldsymbol{\Phi}^T\mathbf{t}_0\, d\mathrm{s}\ . \tag{2.58}$$

The element stiffness matrix $\mathbf{K}^e$ and the right hand side of the equation system, $\mathbf{F}^e$, then read as

$$\mathbf{K}^e = \int_{\Omega^e} \mathbf{B}^T \mathbf{C} \mathbf{B} \, d\mathbf{x} \; , \; \mathbf{F}^e = \int_{\Omega^e} \mathbf{\Phi}^T \mathbf{f} \, d\mathbf{x} + \int_{\Gamma_d} \mathbf{\Phi}^T \mathbf{t}_0 \, d\mathrm{s} \tag{2.59}$$

and the global version of eq. (2.58) is given as

$$(\delta \mathbf{d})^T \left(\mathop{\mathbf{A}}_{i=1}^{N_E} \int_{\Omega_i^e} \mathbf{B}^T \mathbf{C} \mathbf{B} \, d\mathbf{x} \right) \mathbf{d} = (\delta \mathbf{d})^T \mathop{\mathbf{A}}_{i=1}^{N_E} \left(\int_{\Omega_i^e} \mathbf{\Phi}^T \mathbf{f} \, d\mathbf{x} + \int_{\Gamma_d} \mathbf{\Phi}^T \mathbf{t}_0 \, d\mathrm{s} \right) \; , \tag{2.60}$$

where $\mathbf{d} = [\mathbf{d_1}, ..., \mathbf{d_{N_N}}]^T$, $\delta\mathbf{d} = [\delta\mathbf{d_1}, ..., \delta\mathbf{d_{N_N}}]^T$ and the operator $\mathbf{A}$ assembles the nodal contributions of elements into the global stiffness matrix and into the global internal force vector. In short terms, eq. (2.60) can be expressed as

$$\mathbf{K}\mathbf{d} = \mathbf{F} \; , \tag{2.61}$$

with $\mathbf{K}, \mathbf{d}$ and $\mathbf{F}$ being the global counterparts of $\mathbf{K}^e, \mathbf{d}^e$ and $\mathbf{F}^e$, respectively. The Dirichlet boundary conditions are not part of the assembly as they prescribe the solution at certain degrees of freedom and therefore need not to be computed.

The integration on element level usually is carried out using Gaussian integration based on a certain number of weighted Gaussian points that are distributed within the element. The choice of the kind of Gaussian integration and the number of Gaussian points is done with respect to the degree of the shape functions and the desired accuracy of the solution. Moreover one usually performs the Gaussian integration on a *parent* element that is defined in a natural coordinate system. Those details are not explained here because they are not relevant for this thesis. Details can be found in each of the references named in the introduction of this chapter.

2.3.4 Special Principles of Potential Energy

According to Willner [157] the complete representation of the considered energy potential is

$$\Pi(\boldsymbol{u}) = \frac{1}{2} \int_{\Omega} \boldsymbol{\sigma} \cdot \boldsymbol{\varepsilon} \, d\boldsymbol{x} - \int_{\Omega} \boldsymbol{f} \cdot \boldsymbol{u} \, d\boldsymbol{x} - \int_{\Gamma_u} \boldsymbol{u}_0 \cdot \boldsymbol{t} \, ds - \int_{\Gamma_d} \boldsymbol{t}_0 \cdot \boldsymbol{u} \, ds \; , \tag{2.62}$$

with traction vector $\boldsymbol{t}$ and $\boldsymbol{u}_0$ and $\boldsymbol{t}_0$ given by boundary conditions. It is called a 1-field functional because it solely depends on $\boldsymbol{u}$. The necessary supplementary conditions for fully defining the linear problem are the expression of the strain in terms of the displacement gradient (2.15) and the constitutive equation (2.22).

There is a number of different energy potentials that directly integrate the supplementary conditions into the potential thereby introducing more (Euler-Lagrange) differential equations. Those potentials are the functional basis for methods like the already mentioned *Enhanced Assumed Strain* method or the *Smoothed FEM* (S-FEM) described in chap. 3. Both of the following energy potential formulations can be viewed as a functional basis of S-FEM, although chap. 3 only uses the 2-field de Veubeke functional.

2.3.4.1 Hu-Washizu The 3-field Hu-Washizu functional integrates both supplementary conditions (2.15) and (2.22) into the functional resulting in

$$\Pi(\boldsymbol{u},\boldsymbol{\varepsilon},\boldsymbol{\sigma}) = \frac{1}{2}\int_\Omega \boldsymbol{\sigma}\cdot\boldsymbol{\varepsilon}\,d\boldsymbol{x} \;-\; \int_\Omega \boldsymbol{f}\cdot\boldsymbol{u}\,d\boldsymbol{x} - \int_{\Gamma_u}\boldsymbol{u}_0\cdot\boldsymbol{t}\,ds - \int_{\Gamma_d}\boldsymbol{t}_0\cdot\boldsymbol{u}\,ds \\ - \int_\Omega \left(\boldsymbol{\varepsilon} - \frac{1}{2}(\nabla^T\boldsymbol{u}+\nabla\boldsymbol{u})\right)\cdot\boldsymbol{\sigma}\,d\boldsymbol{x}\,. \tag{2.63}$$

In this functional all three fields are treated as unknowns. Using the supplementary condition (2.22) again to eliminate $\boldsymbol{\sigma}$ leads to the 2-field de Veubeke functional.

2.3.4.2 de Veubeke Using symmetry of the stress tensor and, for convenience, the constitutive tensor in tensor notation, it reads as

$$\begin{aligned}\Pi(\boldsymbol{u},\boldsymbol{\varepsilon}) = \frac{1}{2}\int_\Omega \mathbb{C}\boldsymbol{\varepsilon}\cdot\boldsymbol{\varepsilon}\,d\boldsymbol{x} \qquad & - \int_\Omega \boldsymbol{f}\cdot\boldsymbol{u}\,d\boldsymbol{x} - \int_{\Gamma_u}\boldsymbol{u}_0\cdot\boldsymbol{t}\,ds - \int_{\Gamma_d}\boldsymbol{t}_0\cdot\boldsymbol{u}\,ds \\ & - \int_\Omega \mathbb{C}\left(\boldsymbol{\varepsilon} - \frac{1}{2}(\nabla^T\boldsymbol{u}+\nabla\boldsymbol{u})\right)\cdot\boldsymbol{\varepsilon}\,d\boldsymbol{x} \\ = -\frac{1}{2}\int_\Omega \mathbb{C}\boldsymbol{\varepsilon}\cdot\boldsymbol{\varepsilon}\,d\boldsymbol{x} \qquad & + \int_\Omega \mathbb{C}\left(\frac{1}{2}(\nabla^T\boldsymbol{u}+\nabla\boldsymbol{u})\right)\cdot\boldsymbol{\varepsilon}\,d\boldsymbol{x} \\ & - \int_\Omega \boldsymbol{f}\cdot\boldsymbol{u}\,d\boldsymbol{x} - \int_{\Gamma_u}\boldsymbol{u}_0\cdot\boldsymbol{t}\,ds - \int_{\Gamma_d}\boldsymbol{t}_0\cdot\boldsymbol{u}\,ds\,.\end{aligned} \tag{2.64}$$

Willner [157] explains that this functional formerly has been called the *Reissner* principle but that it should be named after de Veubeke. Liu and Nguyen [95] even call it *Hellinger-Reissner* principle. Within this thesis a functional $\Pi(\boldsymbol{u},\boldsymbol{\sigma})$ is called a *Hellinger-Reissner* functional.

The variation of the de Veubeke potential energy

$$\delta\Pi(\boldsymbol{u},\boldsymbol{\varepsilon}) = -\frac{1}{2}\int_\Omega \mathbb{C}\boldsymbol{\varepsilon}\delta\boldsymbol{\varepsilon}\,d\boldsymbol{x} \;+\; \int_\Omega \mathbb{C}\left(\frac{1}{2}(\nabla^T\boldsymbol{u}+\nabla\boldsymbol{u})\right)\cdot\delta\boldsymbol{\varepsilon}\,d\boldsymbol{x} \\ - \int_\Omega \boldsymbol{f}\cdot\delta\boldsymbol{u}\,d\boldsymbol{x} - \int_{\Gamma_u}\boldsymbol{u}_0\cdot\delta\boldsymbol{t}\,ds - \int_{\Gamma_d}\boldsymbol{t}_0\cdot\delta\boldsymbol{u}\,ds \tag{2.65}$$

delivers the principle of virtual displacements that is later used for the variationally consistent derivation of S-FEM. The nonlinear variational form is straightforward and can be found in Willner [157].

2.3.5 Nonlinear FEM

The derivation of the principle of virtual displacements for geometrically nonlinear three-dimensional problems can be found in e.g. Crisfield [34] and Bathe [6], the latter of

which is the foundation of this section. Geometrically nonlinear plate problems can be viewed as a special case of a three-dimensional problem, thus here the principle for the three-dimensional case is derived.

For the nonlinear case we rewrite the linear principle of virtual displacements (2.45), stay in Voigt's notation for convenience and seek for an incremental solution $\boldsymbol{u}_{t+\Delta t}$ at time $t + \Delta t$ that satisfies

$$\int_{\Omega} \delta\boldsymbol{\varepsilon}^T_{t+\Delta t}\boldsymbol{\sigma}_{t+\Delta t}\, d\boldsymbol{x} = \boldsymbol{R}_{t+\Delta t} \;, \tag{2.66}$$

with $\boldsymbol{R}_{t+\Delta t}$ containing the body forces and the static boundary conditions. Assuming that $\boldsymbol{\varepsilon}$ is nonlinear now, one has to linearize eq. (2.66) using Taylor series expansion at a degree of freedom u_j. With an incremental change, Δu_j, the linearization of the integrand is given as

$$\delta\boldsymbol{\varepsilon}^T_{t+\Delta t}\boldsymbol{\sigma}_{t+\Delta t} = \delta\boldsymbol{\varepsilon}^T_t\boldsymbol{\sigma}_t + \frac{\partial\left(\delta\boldsymbol{\varepsilon}^T_t\boldsymbol{\sigma}_t\right)}{\partial u_j}\Delta u_j \;. \tag{2.67}$$

From this notation it becomes apparent that in the incremental procedure, computable quantities at time t are employed to compute the solution at time $t + \Delta t$. Moreover, due to the nonlinearity of the problem, the accuracy of the solution strongly depends on the time step Δt. Keeping this in mind, in the sequel the time information is dropped for compactness. Using the following property of a variation

$$\delta\boldsymbol{\varepsilon} = \frac{\partial\boldsymbol{\varepsilon}}{\partial u_j}\delta u_j \;, \tag{2.68}$$

the second term in eq. (2.67) can be differentiated and simplified as follows

$$\begin{aligned}
\frac{\partial\left(\delta\boldsymbol{\varepsilon}^T\boldsymbol{\sigma}\right)}{\partial u_j}\Delta u_j &= \left(\frac{\partial\delta\boldsymbol{\varepsilon}^T}{\partial u_j}\boldsymbol{\sigma} + \delta\boldsymbol{\varepsilon}^T\frac{\partial\boldsymbol{\sigma}}{\partial u_j}\right)\Delta u_j \\
&= \left(\delta u_j^T\frac{\partial^2\boldsymbol{\varepsilon}^T}{\partial u_j^2}\boldsymbol{\sigma} + \delta u_j^T\frac{\partial\boldsymbol{\varepsilon}^T}{\partial u_j}\frac{\partial\boldsymbol{\sigma}}{\partial\boldsymbol{\varepsilon}}\frac{\partial\boldsymbol{\varepsilon}}{\partial u_j}\right)\Delta u_j \\
&= \delta u_j^T\left(\frac{\partial^2\boldsymbol{\varepsilon}^T}{\partial u_j^2}\boldsymbol{\sigma} + \frac{\partial\boldsymbol{\varepsilon}^T}{\partial u_j}\mathbb{C}\frac{\partial\boldsymbol{\varepsilon}}{\partial u_j}\right)\Delta u_j \;,
\end{aligned} \tag{2.69}$$

which leads to the linearized principle of virtual displacements

$$\delta u_j^T\int_{\Omega}\frac{\partial\boldsymbol{\varepsilon}^T}{\partial u_j}\boldsymbol{\sigma}\, d\boldsymbol{x} + \delta u_j^T\int_{\Omega}\left(\frac{\partial^2\boldsymbol{\varepsilon}^T}{\partial u_j^2}\boldsymbol{\sigma} + \frac{\partial\boldsymbol{\varepsilon}^T}{\partial u_j}\mathbb{C}\frac{\partial\boldsymbol{\varepsilon}}{\partial u_j}\right) d\boldsymbol{x}\Delta u_j = \boldsymbol{R} \tag{2.70}$$

or

$$\delta u_j^T\int_{\Omega}\left(\frac{\partial^2\boldsymbol{\varepsilon}^T}{\partial u_j^2}\boldsymbol{\sigma} + \frac{\partial\boldsymbol{\varepsilon}^T}{\partial u_j}\mathbb{C}\frac{\partial\boldsymbol{\varepsilon}}{\partial u_j}\right) d\boldsymbol{x}\Delta u_j = \boldsymbol{R} - \delta u_j^T\int_{\Omega}\frac{\partial\boldsymbol{\varepsilon}^T}{\partial u_j}\boldsymbol{\sigma}\, d\boldsymbol{x} \;. \tag{2.71}$$

The second term on the left hand side is called the material stiffness as before. The first term arises from the geometrical nonlinearity and therefore is called the geometrical stiffness. On the right hand side an additional term appears in the nonlinear formulation that can be identified with internal forces.

The nonlinear global principle of virtual work can now be expressed using the matrices known from the linear FEM. It reads as

$$(\mathbf{K}_m + \mathbf{K}_g)\mathbf{d} = \mathbf{R} - \mathbf{F} \,, \tag{2.72}$$

with the global material and geometrical stiffness matrices $\mathbf{K}_m$ and $\mathbf{K}_g$, respectively, or in more detail

$$\left(\int_\Omega \mathbf{B}^T \mathbf{C} \mathbf{B} \, d\mathbf{x} + \int_\Omega \mathbf{G}^T \mathbf{S} \mathbf{G} \, d\mathbf{x} \right) \mathbf{d} = \mathbf{R} - \int_\Omega \mathbf{B}^T \mathbf{S} \, d\mathbf{x} \,, \tag{2.73}$$

where $\mathbf{B}$ now is the nonlinear strain-displacement matrix related to the nonlinear strain (2.14) and $\mathbf{G}$ contains derivatives of shape functions. Finally, $\mathbf{S}$ is a matrix of stress components, such that the second term on the right hand side of eq. (2.73) represents the internal forces. Detailed expressions of the respective matrices are omitted here because for geometrically nonlinear plate problems they are given in sect. 3.4.

2.3.6 Finite Element Discretization of Plates and Shells

As it is apparent from the cited references, FE discretizations exist for any of the theories shown in fig. 2.4. In this thesis the Reissner-Mindlin theory has been applied and two different FE discretizations have been used. Both of them use triangular elements because a robust automatic meshing is required for biomechanical applications in general, although not necessarily for the particular model built here. In terms of standard FEM the shape functions are of degree two whereas in the context of S-FEM only linear shape functions are employed. In the latter case the disadvantages of constant strain triangular elements are greatly reduced by S-FEM.

Both discretizations introduce six degrees of freedom per node, three of which are translational and two of which are rotational. The sixth degree of freedom does not have a physical meaning and the related stiffness is chosen very small to only marginally influence the result but sufficiently large to avoid ill conditioning.

3 Smoothed FEM

The FE modeling of biological tissue possesses some general difficulties:

- **Mesh quality:** First of all the mesh quality often is bad, i.e. one expects high aspect ratios of the inner angles of at least some elements. With respect to soft biological tissues there are some possible reasons for a bad mesh quality:

  1. The considered geometries defined by the problem domain usually can not be discretized with other elements than triangles or tetrahedrals because of their complexity. Patient-specific geometrical data from X-Ray, MRI, CT, plastinates or similar imaging procedures usually result in geometrical data where most of the automatic meshing algorithms fail. Even requiring some manual repairing, the only class of meshing algorithm that is able to reliably produce a valid FE mesh, is triangulation in 2D and 3D. Besides the fact that a common triangulation in those cases usually produces some elements with high aspect ratios between the inner angles of the triangle, in general triangular, as well as tetrahedral meshes are known to have a worse performance than their quadrilateral and hexahedral counterparts, respectively.
  2. Even if the automatic and manual efforts result in a reasonable mesh quality, difficulties arise during deformation. Soft biological tissues undergo large deformations that again lead to high aspect ratios. Even more so if some elements already have high aspect ratios that become even higher. Unfortunately one badly shaped element already leads to computational problems or even abortion of the computation. Remeshing is a possible but very expensive remedy in terms of computation time.
  3. The simulation of cutting soft tissues is done in real-time for surgical training purposes. Cutting eventually produces badly shaped elements that have to be handled with caution.

  In the best case, if the computation does not abort due to a singularity, shear locking might occur because of the distorted elements, resulting in highly inaccurate deformation behaviour.

- **Incompressibility:** Biological soft tissues often are (quasi-)incompressible, i.e. $J = det(\boldsymbol{F}) \approx 1$, which leads to the volumetric locking phenomenon in a standard FE setup. To overcome this problem some techniques already exist, like underintegrated elements. A comprehensive and well-written overview of these techniques is given in Koschnick [85]. In order to impose incompressibility the constitutive tensor can be decomposed into a deviatoric and a volumetric part (cf. Holzapfel [72]).

- **Transverse shear locking:** With respect to the thin plate problem that is investigated in this thesis another locking phenomenon occurs, namely the transverse shear locking. It occurs in the computation of very thin structures and leads to inaccurate deformation behaviour too. This locking phenomenon stiffens the system and the

computed deformation is often much smaller than the real deformation. There are advanced techniques to remedy this locking phenomenon like the *Discrete Shear Gap* method presented in Bletzinger et al. [14].

Most of the named problems lead to some kind of locking. A very informative and comprehensive thesis on locking phenomena and their treatment has been written by Koschnick [85]. One way to overcome all the named problems at the same time is the so-called smoothed FEM (S-FEM). S-FEM is a class of methods that bases on the idea of strain smoothing. Chen et al. [25] started to apply this idea to avoid material instabilities in meshless methods and Chen et al. [26] proposed to use strain smoothing for stabilizing nodal integration. Since then, S-FEM has been developed and a collection of S-FEM theory and computational examples can be found in Liu and Nguyen [95]. There is a large number of different kinds of S-FEM with different benefits and drawbacks that are explained in detail in Liu and Nguyen [95] too. Some of them are presented in sect. 3.3. Moreover there is a number of publications covering different topics concerning S-FEM, like Cui et al. [36], Dai and Liu [39], Dai et al. [40], Liu et al. [96] and Liu et al. [97] that construct S-FEM for various 2D problems, Cui et al. [38], Frotscher and Staat [50] and Nguyen-Xuan et al. [113] that apply S-FEM on plates and shells, Bordas et al. [19], Chen et al. [27], Liu et al. [94] and Nix et al. [118] where S-FEM is combined with the extended FEM and for instance Nguyen-Thoi et al. [112] where the face-based S-FEM is introduced for 3D problems.

Within this thesis the so-called edge-based Smoothed Finite Element Method (ES-FEM) is applied to the nonlinear plate problems because this method shows a very good accuracy when applied to linear triangular elements, it is insensitive to element distortion and it overcomes shear locking naturally. Before the ES-FEM becomes explained in detail, the idea of strain smoothing and the variational details for S-FEM are presented. Some parts of this chapter already appeared in Frotscher et al. [54] and are repeated here with some modifications.

3.1 Strain Smoothing

All different kinds of S-FEM share the idea of smoothing the strain over so-called smoothing domains Ω_i^s

$$\bar{\boldsymbol{\varepsilon}}_i = \bar{\boldsymbol{\varepsilon}}(\boldsymbol{x}_i) = \int_{\Omega_i^s} W(\boldsymbol{x}_i - \boldsymbol{x}) \boldsymbol{\varepsilon}(\boldsymbol{x}) \, d\Omega \,, \tag{3.1}$$

with $\boldsymbol{\varepsilon}$ being the usual, possibly known, (compatible) strain, W representing a scalar weighting function and $\bar{\boldsymbol{\varepsilon}}_i$ being the smoothed strain in Ω_i^s. In order to stay consistent with the FEM the smoothing domains are non-overlapping, i.e. $\Omega_i^s \cap \Omega_j^s = \emptyset (i \neq j)$ but fully cover the computational domain, i.e. $\Omega_1^s \cup \cdots \cup \Omega_{N_s}^s = \Omega$, where N_s is the total number of smoothing domains. Usually W is chosen in the way that the smoothed strain

in eq. (3.1) becomes an area-weighted average of the strains in the smoothing domain

$$W(\boldsymbol{x}_i - \boldsymbol{x}) = \begin{cases} \frac{1}{A_i^s}, & \boldsymbol{x} \in \Omega_i^s \\ 0, & \boldsymbol{x} \notin \Omega_i^s \end{cases} , \tag{3.2}$$

with A_i^s the area of the i-th smoothing domain. In the case of a plate problem we can apply eq. (3.1) to each strain part separately using eq. (3.2) to get

$$\bar{\boldsymbol{\varepsilon}}_i^l = \frac{1}{A_i^s} \int_{\Omega_i^s} \boldsymbol{\varepsilon}_i^l(\boldsymbol{x})\, d\Omega , \tag{3.3}$$

$$\bar{\boldsymbol{\varepsilon}}_i^b = \frac{1}{A_i^s} \int_{\Omega_i^s} \boldsymbol{\varepsilon}_i^b(\boldsymbol{x})\, d\Omega , \tag{3.4}$$

$$\bar{\boldsymbol{\varepsilon}}_i^s = \frac{1}{A_i^s} \int_{\Omega_i^s} \boldsymbol{\varepsilon}_i^s(\boldsymbol{x})\, d\Omega , \tag{3.5}$$

$$\bar{\boldsymbol{\varepsilon}}_i^{nl} = \frac{1}{A_i^s} \int_{\Omega_i^s} \boldsymbol{\varepsilon}_i^{nl}(\boldsymbol{x})\, d\Omega , \tag{3.6}$$

with $\bar{\boldsymbol{\varepsilon}}_i^l, \bar{\boldsymbol{\varepsilon}}_i^b, \bar{\boldsymbol{\varepsilon}}_i^s, \bar{\boldsymbol{\varepsilon}}_i^{nl}$ the smoothed linear membrane, bending, shear and nonlinear strain parts, respectively.

In eqs. (3.1) and (3.3)–(3.6) a known strain $\boldsymbol{\varepsilon}$ becomes smoothed. One way of getting a known strain field is to perform a standard FE computation and smooth the compatible strain afterwards. In this case the S-FEM is boiled down to a simple averaging procedure. As the reader will see below it is more advantageous to avoid the smoothing of the compatible strain and compute the smoothed strain directly instead. The principle idea of strain smoothing can easily be explained with respect to the smoothed linear membrane strain and the same procedure can be applied to the other smoothed strain parts too. To get to the discretized equations, first the compatible strain is replaced by an unknown strain that can be computed using the differential operator $\boldsymbol{L}_d$

$$\bar{\boldsymbol{\varepsilon}}^l(\boldsymbol{x}_i) = \int_{\Omega_i^s} \boldsymbol{L}_d \bar{\boldsymbol{u}}(\boldsymbol{x}) W(\boldsymbol{x}_i - \boldsymbol{x})\, d\Omega . \tag{3.7}$$

Using integration by parts one can transform the domain integral in eq. (3.7) into an integral over the boundary Γ_i^s of the smoothing domain

$$\begin{aligned} \bar{\boldsymbol{\varepsilon}}^l(\boldsymbol{x}_i) &= \int_{\Gamma_i^s} \boldsymbol{L}_n(\boldsymbol{x}) \bar{\boldsymbol{u}}(\boldsymbol{x}) W(\boldsymbol{x}_i - \boldsymbol{x})\, d\Gamma - \int_{\Omega_i^s} \bar{\boldsymbol{u}}(\boldsymbol{x}) \underbrace{\dot{W}(\boldsymbol{x}_i - \boldsymbol{x})}_{=0}\, d\Omega \\ &= \frac{1}{A_i^s} \int_{\Gamma_i^s} \underbrace{\begin{bmatrix} n_1 & 0 \\ 0 & n_2 \\ n_2 & n_1 \end{bmatrix}}_{\boldsymbol{L}_n(\boldsymbol{x})} \bar{\boldsymbol{u}}(\boldsymbol{x})\, d\Gamma \;\; \forall \boldsymbol{x} \in \Omega_i^s . \end{aligned} \tag{3.8}$$

It is apparent that $\boldsymbol{L}_n$ contains the components of the outward normal vector on the boundary of the smoothing domain and that the strains are no longer the symmetric part of the displacement gradient because no derivatives of shape functions are involved in eq. (3.8). The next step would be to derive the discretized equations but first the variational basis of S-FEM is derived and further the smoothing domain creation is adressed.

3.2 Smoothed Galerkin Weak Form

Liu and Nguyen [95] derive the smoothed Galerkin weak form from the 2-field de Veubeke variational principle although therein it is called the Hellinger-Reissner principle. Assuming an admissible strain field $\bar{\boldsymbol{\varepsilon}}$ that can be obtained from the displacement field $\bar{\boldsymbol{u}}$ the de Veubeke variational principle (cf. eq. (2.65)) degenerates into a 1-field variational principle. Its variation in Voigt's notation on smoothing domain Ω_i^s reads as

$$\begin{aligned}\delta\Pi(\bar{\boldsymbol{u}})|_{\Omega_i^s} &= \delta\left(-\frac{1}{2}\int\limits_{\Omega_i^s}\bar{\boldsymbol{\varepsilon}}_i{}^T(\bar{\boldsymbol{u}})\mathbb{C}\bar{\boldsymbol{\varepsilon}}_i(\bar{\boldsymbol{u}})\,d\boldsymbol{x}+\int\limits_{\Omega_i^s}\bar{\boldsymbol{\varepsilon}}_i{}^T(\bar{\boldsymbol{u}})\mathbb{C}\left(\boldsymbol{L}\bar{\boldsymbol{u}}\right)\,d\boldsymbol{x}\right)\\ &\quad-\int\limits_{\Omega}\delta\bar{\boldsymbol{u}}^T\boldsymbol{f}\,d\boldsymbol{x}-\int\limits_{\Gamma_u}\delta\bar{\boldsymbol{t}}^T\boldsymbol{u}_0\,ds-\int\limits_{\Gamma_d}\delta\bar{\boldsymbol{u}}^T\boldsymbol{t}_0\,ds\,,\end{aligned}\tag{3.9}$$

with a differential operator $\boldsymbol{L}$. Taking into account the assumption that the smoothed strain $\bar{\boldsymbol{\varepsilon}}$ is constant within a smoothing domain leads to

$$\int\limits_{\Omega_i^s}\bar{\boldsymbol{\varepsilon}}_i{}^T(\bar{\boldsymbol{u}})\mathbb{C}\left(\boldsymbol{L}\bar{\boldsymbol{u}}\right)\,d\boldsymbol{x}=\bar{\boldsymbol{\varepsilon}}_i{}^T(\bar{\boldsymbol{u}})\mathbb{C}A_i^s\boldsymbol{L}\bar{\boldsymbol{u}}=\int\limits_{\Omega_i^s}\bar{\boldsymbol{\varepsilon}}_i{}^T(\bar{\boldsymbol{u}})\mathbb{C}\bar{\boldsymbol{\varepsilon}}_i(\bar{\boldsymbol{u}})\,d\boldsymbol{x}\,.\tag{3.10}$$

Reinserting this into eq. (3.9) and using a similar assembly process as in standard FEM to get the global discretized weak form one gets

$$\begin{aligned}\delta\Pi(\bar{\boldsymbol{u}}) &= \delta\mathop{\mathbf{A}}_{i=1}^{N_s}\left(\frac{1}{2}\int\limits_{\Omega_i^s}\bar{\boldsymbol{\varepsilon}}_i{}^T(\bar{\boldsymbol{u}})\mathbb{C}\bar{\boldsymbol{\varepsilon}}_i(\bar{\boldsymbol{u}})\,d\boldsymbol{x}\right)\\ &\quad-\int\limits_{\Omega}\delta\bar{\boldsymbol{u}}^T\boldsymbol{f}\,d\boldsymbol{x}-\int\limits_{\Gamma_u}\delta\bar{\boldsymbol{t}}^T\boldsymbol{u}_0\,ds-\int\limits_{\Gamma_d}\delta\bar{\boldsymbol{u}}^T\boldsymbol{t}_0\,ds\,.\end{aligned}\tag{3.11}$$

For the linear part of the smoothed strain one inserts eq. (3.8) into eq. (3.11), which leads to

$$\begin{aligned}\delta\Pi(\bar{\boldsymbol{u}}) &= \mathop{\mathbf{A}}_{i=1}^{N_s}\left(\frac{1}{A_i^s}\int\limits_{\Gamma_i^s}(\boldsymbol{L}_n\delta\bar{\boldsymbol{u}})^T\mathbb{C}(\boldsymbol{L}_n\bar{\boldsymbol{u}})\,d\boldsymbol{x}\right)\\ &\quad-\int\limits_{\Omega}\delta\bar{\boldsymbol{u}}^T\boldsymbol{f}\,d\boldsymbol{x}-\int\limits_{\Gamma_u}\delta\bar{\boldsymbol{t}}^T\boldsymbol{u}_0\,ds-\int\limits_{\Gamma_d}\delta\bar{\boldsymbol{u}}^T\boldsymbol{t}_0\,ds\,.\end{aligned}\tag{3.12}$$

This variational form can now be specialized for any kind of S-FEM by choosing the respective smoothing domains. The most important message from this section is that S-FEM methods are variationally consistent because they can be derived from the de Veubeke variational form.

3.3 Smoothing Domains

So far the shape or creation of the smoothing domains have not been adressed. The basic S-FEM kinds are the cell-based (CS-FEM), the node-based (NS-FEM) and the edge-based (ES-FEM) S-FEM for 2D meshes and the face-based (FS-FEM) S-FEM for 3D meshes. Those methods solely differ in the creation of the smoothing domains thereby creating different advantages. Combinations of different kinds of S-FEM to get the benefits in the part of the mesh where they are needed or direct combination of the methods on smoothing domain level (αS-FEM) already have been developed by Liu and Nguyen [95].

All the methods have in common that they create their smoothing domains based on a standard FE mesh constisting of linear elements, without the introduction of additional nodes or degrees of freedom. Within the smoothing domains a constant strain is assumed. Figure 3.1 depicts four possible ways of smoothing domain creation in the case of CS-FEM. CS-FEM can be applied to quadrilateral elements by subdividing each element Ω_i^e into a number of smoothing cells $\Omega_{i_e}^s$, with i_e depending on the respective element. Cell-based smoothing domains are formed by taking the nodes of the finite element and virtual nodes on the element boundary as well as inside the element as corner points of the cells. The way of subdivision and the number of smoothing cells should be chosen with respect to stability requirements. Regarding stability there is an optimal number of smoothing cells per element. Figure 3.1 shows a quadrilateral element that has been subdivided into 1,2,3 and 4 smoothing cells.

Figure 3.2 shows that node-based smoothing domains are created around each node of the FE mesh by taking the barycenters of the elements surrounding the respective node and the midpoints of each edge connected to the node as the cornerpoints of the smoothing domain. The special property of NS-FEM is that it is free of volumetric locking. Therefore the selective combination of CS-FEM and NS-FEM to NCS-FEM is very beneficial to have the stability and accuracy of CS-FEM and to get rid of the volumetric locking where it occurs.

Figure 3.3 shows a middle plane of a plate that is meshed with three triangular elements based on four nodes A, B, C and D. Two edge-based smoothing domains Ω_k^s and Ω_m^s are highlighted here; the former one bases on edge k and the latter one on edge m of the standard finite element mesh. Both are formed using the two corner nodes of the respective edge and the barycenters of the element(s) connected to the respective edge. Please note that, as in any of the S-FEM kinds, the barycenters are virtual nodes thus they do not carry additional degrees of freedom. Concerning the discretization there is no difference between 2D and plate problems despite from the number of degrees of freedoms. The ES-FEM and its benefits are explained in detail in sect. 3.4 because it is the method of choice with respect to the computation of soft biological tissues. The last basic S-FEM

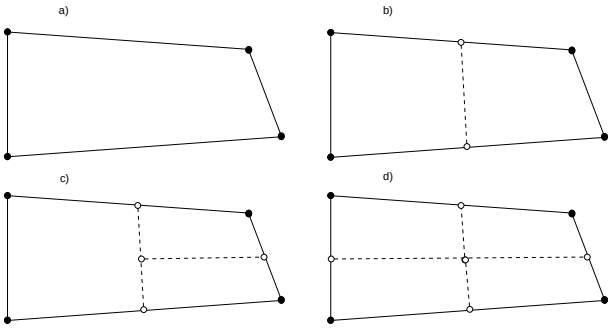

Figure 3.1: Cell-based smoothing domains

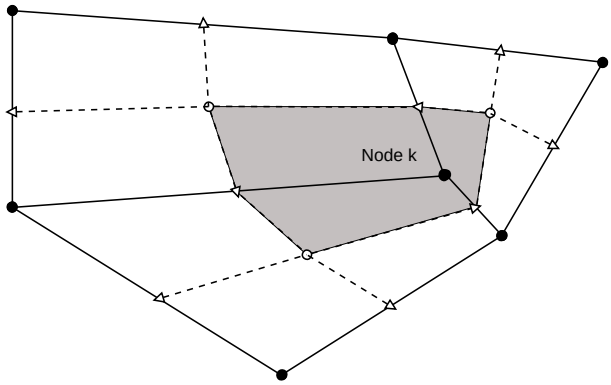

Figure 3.2: Node-based smoothing domains

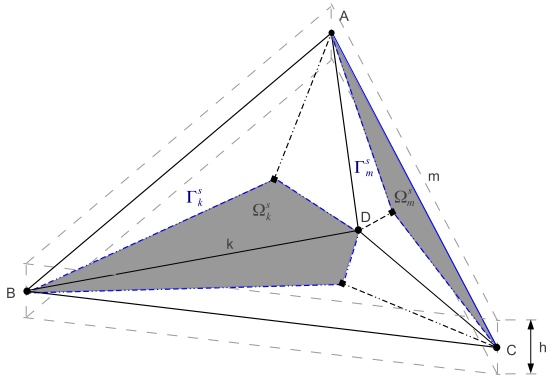

Figure 3.3: Edge-based smoothing domains

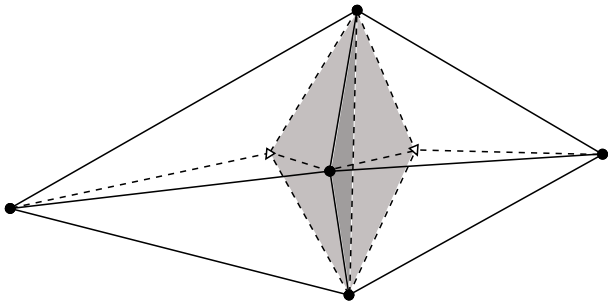

Figure 3.4: Face-based smoothing domains

kind is the FS-FEM, shown in fig. 3.4. It is the 3D equivalent of ES-FEM and basically has the same properties.

3.4 Edge-based S-FEM for Nonlinear Plate Problems

Equation (3.12) reveals that the integration is now performed on smoothing domains instead of elements. Besides the fact that the local quantities now lie on smoothing domains the discretization of eq. (3.8) looks quite familiar:

$$\bar{\boldsymbol{\varepsilon}}^l(\mathbf{x}_i) = \sum_{I=1}^{N_n} \bar{\mathbf{B}}_I^l(\mathbf{x}_i)\bar{\mathbf{d}}_I \ , \tag{3.13}$$

with N_n being the number of nodes related to the smoothing domain, $\bar{\mathbf{B}}_I^l$ being the respective smoothed strain-displacement matrix and $\bar{\mathbf{d}}_I$ being the nodal vector of degrees of freedom at node I. For plate problems each nodal $\bar{\mathbf{d}}_I = [\bar{d}_{I1}, \bar{d}_{I2}, \bar{d}_{I3}, \bar{d}_{I4}, \bar{d}_{I5}]^T$ contains two in-plane translational, one out-of-plane translational and two rotational degrees of freedom according to the plate kinematics given by eqs. (2.29)–(2.31). Regarding the example in fig. 3.3 N_n takes the values 3 for Ω_m^s and 4 for Ω_k^s. An *inner* smoothing

domain like Ω_k^s occupies space in two different elements thereby relating all the nodes of both elements. As a consequence the local stiffness matrix on Ω_k^s has an increased size compared to standard FEM leading to an increased bandwidth of the global matrices.

Please note that for the computation of the global smoothed displacement field $\bar{\mathbf{u}}$, the N standard nodal shape functions are employed and that the isoparametric concept is still used. N is the total number of nodes in the FE mesh. From eqs. (3.8) and (3.13) it is now possible to construct

$$\bar{\mathbf{B}}_I^l(\mathbf{x}_i) = \frac{1}{A_i^s} \int_{\Gamma_i^s} \mathbf{L}_n(\mathbf{x}) \Phi_I(\mathbf{x}) \, d\Gamma = \begin{bmatrix} \bar{b}_{I1} & 0 & 0 & 0 & 0 \\ 0 & \bar{b}_{I2} & 0 & 0 & 0 \\ \bar{b}_{I2} & \bar{b}_{I1} & 0 & 0 & 0 \end{bmatrix} , \tag{3.14}$$

with

$$\mathbf{L}_n(\mathbf{x}) = \begin{bmatrix} n_1(\mathbf{x}) & 0 & 0 & 0 & 0 \\ 0 & n_2(\mathbf{x}) & 0 & 0 & 0 \\ n_2(\mathbf{x}) & n_1(\mathbf{x}) & 0 & 0 & 0 \end{bmatrix} \tag{3.15}$$

containing the components of the outwards directed normal vector on the boundary of the smoothing domain. The structure of $\mathbf{L}_n$ differs with respect to the respective part of the strain (cf. eqs. (3.19)–(3.21)). The entries of the smoothed strain-displacement matrix read as

$$\bar{\mathbf{b}}_I(\mathbf{x}_i) = \frac{1}{A_i^s} \int_{\Gamma_i^s} \Phi_I(\mathbf{x}) \mathbf{n}_i(\mathbf{x}) \, d\Gamma \, . \tag{3.16}$$

Placing Gauss Points in the center of each boundary segment of the smoothing domain (e.g. Γ_k^s and Γ_m^s in fig. 3.3) one discretizes the remaining boundary integral to get

$$\bar{\mathbf{b}}_I(\mathbf{x}_i) = \frac{1}{A_i^s} \sum_{k=1}^{N_s} \Phi_I(\mathbf{x}_k^{GP}) \mathbf{n}_i(\mathbf{x}_k^{GP}) l_k \, , \tag{3.17}$$

with N_s being the number of boundary segments, $\mathbf{x}_k^{GP}$ the Gaussian Point at the center of segment Γ_k, $\mathbf{n}_i$ the outward normal vector and l_k the length of segment Γ_k. Of course, like in standard FEM the number of Gaussian Points and also their placement can vary. Regarding the fact that the strain is assumed to be constant within a smoothing domain the placement of one Gaussian Point at the center of each boundary segment is sufficient. Concerning applications that have to deal with discontinuities (Smoothed X-FEM) more Gaussian Points are used and differently distributed within the smoothing domain in order to better resolve close to the discontinuity.

It has been mentioned earlier that computing the smoothed strain from eq. (3.13) rather than using a known compatible strain field is beneficial. The first reason is that the computation of $\bar{\mathbf{B}}_I$ does not require derivatives of shape functions. The shape functions themselves are sufficient due to the boundary integral formulation. Secondly, with the choice of linear triangular elements all quantities are computed in physical coordinates thus isoparametric mappings are avoided.

The given procedure applies to the other parts of $\bar{\mathbf{B}}$ too thus the smoothed strain-displacement matrix for smoothing domain Ω_i^s reads as

$$\bar{\mathbf{B}}_i = \begin{bmatrix} \bar{\mathbf{B}}_i^l + \bar{\mathbf{B}}_i^{nl} \\ \bar{\mathbf{B}}_i^b \\ \bar{\mathbf{B}}_i^s \end{bmatrix} , \tag{3.18}$$

with $\bar{\mathbf{B}}_i = [\bar{\mathbf{B}}_1, ..., \bar{\mathbf{B}}_{N_n}]$. $\bar{\mathbf{B}}_I^l$ has already been given in eq. (3.14). The other parts of the smoothed strain are

$$\bar{\mathbf{B}}_I^b = \begin{bmatrix} 0 & 0 & 0 & 0 & \bar{b}_{I1} \\ 0 & 0 & 0 & -\bar{b}_{I2} & 0 \\ 0 & 0 & 0 & -\bar{b}_{I1} & \bar{b}_{I2} \end{bmatrix} , \tag{3.19}$$

$$\bar{\mathbf{B}}_I^s = \begin{bmatrix} 0 & 0 & \bar{b}_{I1} & \frac{1}{N_n}\sum_{j=1}^{N_n}\Phi_I(\mathbf{x}_j) & 0 \\ 0 & 0 & \bar{b}_{I2} & 0 & \frac{1}{N_n}\sum_{j=1}^{N_n}\Phi_I(\mathbf{x}_j) \end{bmatrix} , \tag{3.20}$$

$$\bar{\mathbf{B}}_I^{nl} = \sum_{J=1}^{N_n} \begin{bmatrix} \bar{b}_{J1}\bar{\omega}_J & 0 \\ 0 & \bar{b}_{J2}\bar{\omega}_J \\ \bar{b}_{J2}\bar{\omega}_J & \bar{b}_{J1}\bar{\omega}_J \end{bmatrix} \begin{bmatrix} 0 & 0 & \bar{b}_{I1} & 0 & 0 \\ 0 & 0 & \bar{b}_{I2} & 0 & 0 \end{bmatrix} , \tag{3.21}$$

with $\bar{\omega}_J$ the nodal deflection. The sum in eq. (3.21) represents the smoothed displacement gradient. The smoothing of which is similar to that of the strain. Starting from

$$\begin{aligned} \bar{\mathbf{H}}(\mathbf{x}_i) &= \int_{\Omega_i^s} \frac{\partial \mathbf{u}}{\partial \mathbf{x}} W(\mathbf{x}_i - \mathbf{x})\, d\mathbf{x} \\ &= \int_{\Gamma_i^s} \mathbf{L}_n \mathbf{u} W(\mathbf{x}_i - \mathbf{x})\, d\mathbf{x} - \int_{\Omega_i^s} \mathbf{u}\dot{W}(\mathbf{x}_i - \mathbf{x})\, d\mathbf{x} \\ &= \frac{1}{A_i^s} \int_{\Gamma_i^s} \mathbf{L}_n \mathbf{u}\, d\mathbf{x} , \end{aligned} \tag{3.22}$$

the discretized smoothed displacement gradient applied to the deflection component only reads as

$$\bar{\mathbf{H}}(\mathbf{x}_i) = \sum_{I=1}^{N_n} \bar{\mathbf{B}}_I \bar{w}_I . \tag{3.23}$$

Figure 3.5 shows the different coordinate systems that are needed for the computation besides the global coordinate system, i.e. the element coordinate systems $\hat{\boldsymbol{\xi}}^1$ and $\hat{\boldsymbol{\xi}}^2$ as well as a smoothing domain coordinate system $\bar{\boldsymbol{\xi}}^1$.

With respect to fig. 3.5 one can sum up the computation of $\bar{\mathbf{B}}_i$ as follows. Both smoothed strain-displacement matrices $\hat{\mathbf{B}}_1$ and $\hat{\mathbf{B}}_2$ are computed on element level in the respective element coordinate system and transformed into the smoothing domain coordinate system

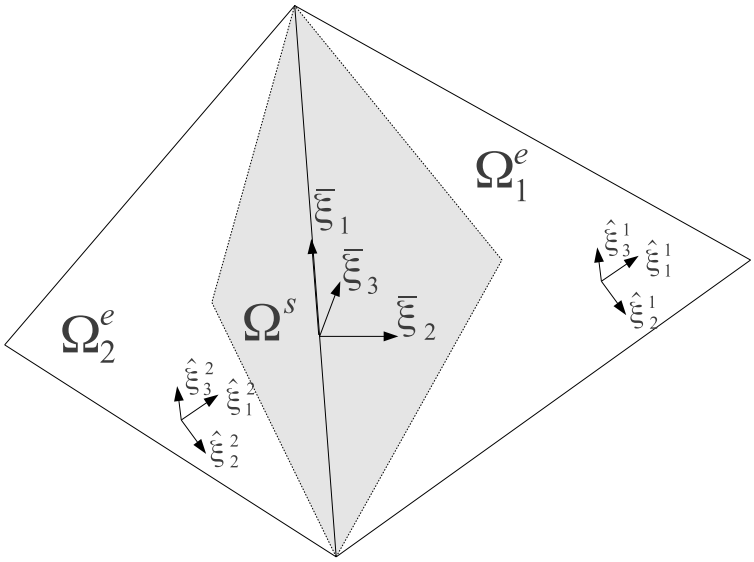

Figure 3.5: Element and smoothing domain coordinate systems

to add up the contributions to $\bar{\mathbf{B}}_i$ from both elements. Realizing that the case is even simpler if the smoothing domain is built around a boundary edge of the computation domain (cf. edge m in fig. 3.3) the smoothed strain-displacement matrix on smoothing domain Ω_i^s reads as

$$\bar{\mathbf{B}}_i^* = \frac{1}{A_i^s} \sum_{k=1}^{N_e} A_k \bar{\mathbf{R}}_{*k}^1 \hat{\mathbf{R}}_{*k}^2 \hat{\mathbf{B}}_k^* \hat{\mathbf{T}}_k \,, \tag{3.24}$$

with N_e the number of elements sharing edge i of the FE mesh, A_k the area of the respective element and the asterisk indicating the applicability to each strain part. The transformation matrices are

$$\hat{\mathbf{T}}_k = \begin{bmatrix} c_{\hat{1}1} & c_{\hat{1}2} & c_{\hat{1}3} & 0 & 0 \\ c_{\hat{2}1} & c_{\hat{2}2} & c_{\hat{2}3} & 0 & 0 \\ c_{\hat{3}1} & c_{\hat{3}2} & c_{\hat{3}3} & 0 & 0 \\ 0 & 0 & 0 & c_{\hat{1}1} & c_{\hat{1}2} \\ 0 & 0 & 0 & c_{\hat{2}1} & c_{\hat{2}2} \end{bmatrix} \,, \tag{3.25}$$

the transformation matrix from global coordinates to element local coordinates,

$$\hat{\mathbf{R}}_{*k}^2 = \begin{bmatrix} c_{\hat{1}1}^2 & c_{\hat{1}2}^2 & c_{\hat{1}3}^2 & 2c_{\hat{1}1}c_{\hat{1}2} & 2c_{\hat{1}1}c_{\hat{1}3} & 2c_{\hat{1}2}c_{\hat{1}3} \\ c_{\hat{2}1}^2 & c_{\hat{2}2}^2 & c_{\hat{2}3}^2 & 2c_{\hat{2}1}c_{\hat{2}2} & 2c_{\hat{2}1}c_{\hat{2}3} & 2c_{\hat{2}2}c_{\hat{2}3} \\ c_{\hat{3}1}^2 & c_{\hat{3}2}^2 & c_{\hat{3}3}^2 & 2c_{\hat{3}1}c_{\hat{3}2} & 2c_{\hat{3}1}c_{\hat{3}3} & 2c_{\hat{3}2}c_{\hat{3}3} \\ c_{\hat{1}1}c_{\hat{2}1} & c_{\hat{1}2}c_{\hat{2}2} & c_{\hat{1}3}c_{\hat{2}3} & c_{\hat{1}1}c_{\hat{2}2} + c_{\hat{1}2}c_{\hat{2}1} & c_{\hat{1}3}c_{\hat{2}1} + c_{\hat{1}1}c_{\hat{2}3} & c_{\hat{1}2}c_{\hat{2}3} + c_{\hat{1}3}c_{\hat{2}2} \\ c_{\hat{1}1}c_{\hat{3}1} & c_{\hat{1}2}c_{\hat{3}2} & c_{\hat{1}3}c_{\hat{3}3} & c_{\hat{3}1}c_{\hat{1}2} + c_{\hat{3}2}c_{\hat{1}1} & c_{\hat{3}3}c_{\hat{1}1} + c_{\hat{3}1}c_{\hat{1}3} & c_{\hat{3}2}c_{\hat{1}3} + c_{\hat{3}3}c_{\hat{1}2} \\ c_{\hat{2}1}c_{\hat{3}1} & c_{\hat{2}2}c_{\hat{3}2} & c_{\hat{2}3}c_{\hat{3}3} & c_{\hat{2}1}c_{\hat{3}2} + c_{\hat{2}2}c_{\hat{3}1} & c_{\hat{2}3}c_{\hat{3}1} + c_{\hat{2}1}c_{\hat{3}3} & c_{\hat{2}2}c_{\hat{3}3} + c_{\hat{2}3}c_{\hat{3}2} \end{bmatrix}^T \,, \tag{3.26}$$

the rotation matrix from element to global coordinates and

$$\bar{\mathbf{R}}^1_{*k} = \begin{bmatrix} c^2_{\bar{1}1} & c^2_{\bar{1}2} & c^2_{\bar{1}3} & c_{\bar{1}1}c_{\bar{1}2} & c_{\bar{1}1}c_{\bar{1}3} & c_{\bar{1}2}c_{\bar{1}3} \\ c^2_{\bar{2}1} & c^2_{\bar{2}2} & c^2_{\bar{2}3} & c_{\bar{2}1}c_{\bar{2}2} & c_{\bar{2}1}c_{\bar{2}3} & c_{\bar{2}2}c_{\bar{2}3} \\ c^2_{\bar{3}1} & c^2_{\bar{3}2} & c^2_{\bar{3}3} & c_{\bar{3}1}c_{\bar{3}2} & c_{\bar{3}1}c_{\bar{3}3} & c_{\bar{3}2}c_{\bar{3}3} \\ 2c_{\bar{1}1}c_{\bar{2}1} & 2c_{\bar{1}2}c_{\bar{2}2} & 2c_{\bar{1}3}c_{\bar{2}3} & c_{\bar{1}1}c_{\bar{2}2}+c_{\bar{1}2}c_{\bar{2}1} & c_{\bar{1}3}c_{\bar{2}1}+c_{\bar{1}1}c_{\bar{2}3} & c_{\bar{1}2}c_{\bar{2}3}+c_{\bar{1}3}c_{\bar{2}2} \\ 2c_{\bar{1}1}c_{\bar{3}1} & 2c_{\bar{1}2}c_{\bar{3}2} & 2c_{\bar{1}3}c_{\bar{3}3} & c_{\bar{3}1}c_{\bar{1}2}+c_{\bar{3}2}c_{\bar{1}1} & c_{\bar{3}3}c_{\bar{1}1}+c_{\bar{3}1}c_{\bar{1}3} & c_{\bar{3}2}c_{\bar{1}3}+c_{\bar{3}3}c_{\bar{1}2} \\ 2c_{\bar{2}1}c_{\bar{3}1} & 2c_{\bar{2}2}c_{\bar{3}2} & 2c_{\bar{2}3}c_{\bar{3}3} & c_{\bar{2}1}c_{\bar{3}2}+c_{\bar{2}2}c_{\bar{3}1} & c_{\bar{2}3}c_{\bar{3}1}+c_{\bar{2}1}c_{\bar{3}3} & c_{\bar{2}2}c_{\bar{3}3}+c_{\bar{2}3}c_{\bar{3}2} \end{bmatrix}, \tag{3.27}$$

the rotation matrix from global to smoothing domain coordinates.

The global smoothed tangent stiffness matrix in the smoothing domain coordinate system then is given by

$$\bar{\mathbf{K}}^t_{IJ} = \sum_{i=1}^{N_s} \left(\bar{\mathbf{B}}_i\right)^T_I \mathbf{C} \left(\bar{\mathbf{B}}_i\right)_J A^s_i + \sum_{i=1}^{N_s} \left(\bar{\mathbf{G}}_i\right)^T_I \breve{\mathbf{N}} \left(\bar{\mathbf{G}}_i\right)_J A^s_i \,, \tag{3.28}$$

with N_s the number of smoothing domains, i.e. edges in the mesh. The second term in eq. (3.28) is the smoothed geometrical stiffness matrix and consists of

$$\left(\bar{\mathbf{G}}_i\right)_I = \begin{bmatrix} 0 & 0 & \bar{b}_{I1} & 0 & 0 \\ 0 & 0 & \bar{b}_{I2} & 0 & 0 \end{bmatrix} \tag{3.29}$$

and the matrix of the membrane stress resultants

$$\breve{\mathbf{N}} = \begin{bmatrix} N_{11} & N_{12} \\ N_{12} & N_{22} \end{bmatrix} . \tag{3.30}$$

According to eq. (2.73) the nodal force vector given in the coordinate system $\bar{\boldsymbol{\xi}}$ can be computed from

$$\bar{\mathbf{F}}_I = \sum_{i=1}^{N_s} \left(\bar{\mathbf{B}}_i\right)^T_I \begin{bmatrix} \mathbf{N} \\ \mathbf{M} \\ \mathbf{T} \end{bmatrix}_I , \tag{3.31}$$

where $\mathbf{N}, \mathbf{M}$ and $\mathbf{T}$ are the discrete axial forces, bending moments and transverse shear forces (cf. eqs. (2.32)–(2.34)). Given that the boundary conditions are integrated as usual (e.g. by elimination or by Lagrangian coefficients) the global system of equations that has to be solved reads as

$$\bar{\mathbf{K}}^t \mathbf{d} = \bar{\mathbf{F}} \,. \tag{3.32}$$

The assembly process for the stiffness matrix and the internal force vector is similar to that of standard FEM although some remarks are indicated. In this work the smoothed local tangent stiffness matrices $\bar{\mathbf{K}}^t_i$ are directly assembled into the global smoothed tangent stiffness matrix. It should be noticed that $\bar{\mathbf{K}}^t \in \mathbb{R}^{5N\times 5N}$ (five degrees of freedom per node) has exactly the same size as the standard tangent stiffness matrix whereas the size of the smoothed local tangent stiffness matrices $\bar{\mathbf{K}}^t_i \in \mathbb{R}^{5N_n\times 5N_n}$ depends on whether the respective smoothing domain is related to an inner edge or an edge on the boundary of the FE mesh. For a mesh consisting of linear triangular elements, in the latter case

$\bar{\mathbf{K}}_i^t$ contributes to three nodes only, i.e. $N_n = 3$, whereas in the former one $N_n = 4$, leading to an increased bandwidth of $\bar{\mathbf{K}}^t$. The proposed smoothing domain-based assembly necessitates a modification of the standard implementation of the assembly process. This can be avoided by splitting up $\bar{\mathbf{K}}_i^t$ into element-wise contributions as for instance done in Cui et al. [37].

For completeness, the final remark concerns the sixth, unphysical degree of freedom at each node, that was already mentioned in sect. 2.3.6. For numerical reasons it is also included in the presented ES-FEM formulation but it has not been shown for compactness.

3.5 Involving the Discrete Shear Gap Method

It has already been shown in sect. 2.2.2 that each component of the shear strain,

$$\boldsymbol{\varepsilon}^s = \begin{pmatrix} v_{3,1} + w_1 \\ v_{3,2} + w_2 \end{pmatrix} , \tag{3.33}$$

is computed from the sum of the first derivative of a displacement v and from a rotation w. For plates one often states the so-called Kirchhoff constraint that requires

$$\gamma = v' + w = 0 . \tag{3.34}$$

However, this is usually in contradiction to the reality which becomes apparent if pure bending is regarded. In the case of pure bending the transverse shear stresses vanish, i.e in theory eq. (3.34) is satisfied but regarding a discretization this is usually not true. Usually the displacements and the rotations are discretized using the same shape functions or at least shape functions of equal degree. One can directly see that this violates the Kirchhoff constraint because after discretization v' is one degree lower than w, i.e.

$$\gamma = v' + w \neq 0 . \tag{3.35}$$

This discrepancy that causes transverse shear locking has been adressed by many different approaches that are detailed and compared in Koschnick [85]. One of the most simple approaches has been published in Bletzinger et al. [14] and is called the *Discrete Shear Gap* (DSG) method. This method introduces a discretized shear gap field on element level that later can be condensed in order to keep the number of degrees of freedom of the element. In a linear triangular element, the discretized shear gap field removes the linear part of the transverse shear which results from the discretization and makes it constant. This way no parasitic shear stresses occur anymore and transverse shear locking is effectively avoided. The DSG method has been generalized for other strain parts in Koschnick et al. [86] and is called the *Discrete Strain Gap* method then.

The ES-FEM triangular plate element employed in this thesis is enhanced by the DSG method. The only thing that changes on element level, is the computation of the shear part of the strain-displacement matrix thus this method can be called a B-bar method. The respective shear strain, $\boldsymbol{\varepsilon}^s_{DSG}$ replaces the standard shear strain on element level. It reads as

$$\boldsymbol{\varepsilon}^s_{DSG} = \mathbf{B}^s_{DSG}[\mathbf{d}_1, \mathbf{d}_2, \mathbf{d}_3]^T , \tag{3.36}$$

with $\mathbf{B}^s_{DSG}$ that has already been presented in NGUYEN-XUAN ET AL. [114] and CUI ET AL. [37] and is shown here for the sake of completeness. $\mathbf{B}^s_{DSG}$ is composed of three nodal parts, thus $\mathbf{B}^s_{DSG} = [\mathbf{B}^{s1}_{DSG}, \mathbf{B}^{s2}_{DSG}, \mathbf{B}^{s3}_{DSG}]$, with

$$\mathbf{B}^{s1}_{DSG} = \frac{1}{2A_k}\begin{bmatrix} 0 & 0 & b-d & 0 & A_k \\ 0 & 0 & c-a & -A_k & 0 \end{bmatrix} \tag{3.37}$$

$$\mathbf{B}^{s2}_{DSG} = \frac{1}{2A_k}\begin{bmatrix} 0 & 0 & d & -\frac{bd}{2} & \frac{ad}{2} \\ 0 & 0 & -c & \frac{bc}{2} & -\frac{ac}{2} \end{bmatrix} \tag{3.38}$$

$$\mathbf{B}^{s3}_{DSG} = \frac{1}{2A_k}\begin{bmatrix} 0 & 0 & -b & \frac{bd}{2} & -\frac{bc}{2} \\ 0 & 0 & a & -\frac{ad}{2} & \frac{ac}{2} \end{bmatrix} . \tag{3.39}$$

The parameters $a = x_2 - x_1, b = y_2 - y_1, c = x_3 - x_1$ and $d = y_3 - y_1$ are computed from the nodal coordinates of the element and A_k is the area of the element. As this method is a B-bar method, nothing changes in the smoothing of this strain part, i.e. eq. (3.24) can be applied to get the respective smoothed strain-displacement matrix.

4 Cardiac Cells and Tissue

This section is intended to provide an overview over human cardiac tissue and cardiac cells as far as it is needed to understand their electrophysiology.

The human heart is an autonomously beating organ as depicted in fig. 4.1 and as most biological tissues each tissue in the human heart consists of a collagen-based extracellular matrix (ECM) and embedded cells. Both, the ECM and the respective cardiac cells are under investigation because they fulfill different tasks. The ECM mainly provides a passive stiffness of the tissue whereas the contribution of cells to the passive stiffness of the tissue is negligible. Cardiac cells mainly provide an active contribution to the stiffness by contraction, be it self-induced or triggered. This thesis investigates the contractile behavior of cardiac cells and therefore the ECM is not explained in further detail. However, it should be noticed that the composition of the ECM in fact strongly influences the overall contractile strength of the tissue.

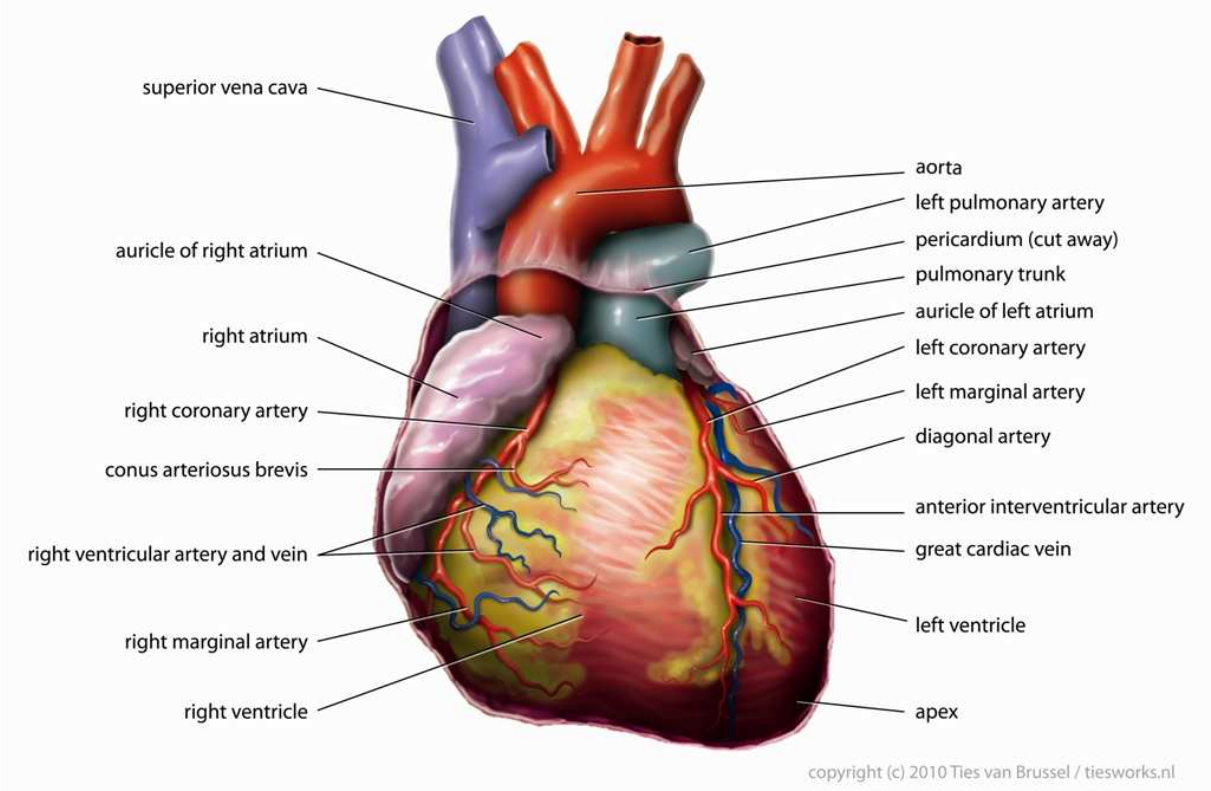

Figure 4.1: The anatomy of the human heart (Credits: Ties van Brussel, public domain)

Cardiac cells consist of overlapping actin and myosin filaments. They are attached via so-called cross bridges. The overlap is strain dependent thus if the tissue is stretched the actin and myosin myofilaments overlap less and the stress produced is higher.

The constituent of the heart that is responsible for generating the electrical stimulus is called *sinoatrial node* (SA node), cf. fig. 4.2. The dominating cells in the SA node are auto-contractile sinoatrial cells. The electrophysiology of SA cells is balanced in a way so

that they autonomously beat with a certain frequency. The electrical conduction system of the heart propagates the generated electrical stimulus through the whole heart.

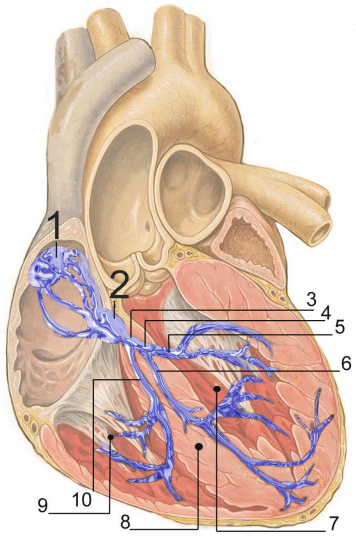

Figure 4.2: Electrical conduction system of the human heart (Credits: J. Heuser, Patrick J. Lynch, medical illustrator; C. Carl Jaffe, MD, cardiologist under Creative Commons License 2.5 `http://creativecommons.org/licenses/by/2.5/`); 1 - Sinoatrial node, 2 - Atrioventricular node

If the SA node is defective the atrioventricular node (AV node), cf. fig. 4.2, becomes important. AV cells are self-contractile as well but they are beating with a slightly lower frequency than SA cells. Consequently, a working SA node triggers the AV node before the latter can send an own trigger signal. In case that the SA node does not work, the AV node can keep the heart working for a certain time with a lower frequency.

This thesis focuses on self-contractile *in vitro* tissues. Therefore it is not necessary to explain the electrical conduction system further. It is more important to understand the electrophysiology on cell level to realize how an *in vitro* tissue can beat autonomously. The electrophysiology of two kinds of cells will now be explained in detail: nodal cells and ventricular cells. The development of an action potential can be described best for the example of Purkinje cells. This cell type creates a ventricular-like action potential but it has the nodal self-contractile characteristics.

It has to be emphasized that the real electrophysiology of any cell inside the human heart is by far more complicated than described here and that it is not even entirely understood. Of course all models have a limit in complexity and accuracy thus they are incomplete with respect to reality.

Further there are many and partially strong differences in the electrophysiology of different cardiomyocytes (CM). The electrophysiology of different native *in vivo* CM differs due to the species of the mammalian, the heart region, the cell type, the health condition of the organism and many more. Even more influences come into play when CM or hiPSC-CM are investigated *in vitro*, among which are the temperature, the pH, the tissue dimension

(isolated cell, cell cluster, monolayer, 3D tissue) or other culture conditions.

To account for some of the differences, computational models of cardiac cells have been established not only with respect to the different cell types within one heart but also with respect to the species. Although they largely influence the cellular electrophysiology, the countless environmental influences can hardly be quantified thus they are normally not incorporated in the models.

In the following, as this thesis focuses on the investigation of human cardiac cells and hiPSC-CM, all the details are related to the human heart if not otherwise stated.

4.1 Purkinje Cells

Purkinje fibers are located inside the ventricular walls, i.e. the walls of the right and left ventricles shown in fig. 4.1. They belong to the pacemaker-conduction system and play a major role in electrical conduction and propagation of impulses to the ventricular muscle. Figure 4.3 schematically illustrates the cellular processes that take place during cell contraction and relaxation. The contents of this figure are very closely related to the computational model that is described later.

An action potential is the transient depolarization of a cell resulting from voltage- and time-dependent currents across the membrane. At rest (phase 4), cardiac muscle cells possess a negative membrane potential due to outward-directed potassium currents I_{K1}. The resting potential depends on the cell type and for purkinje cells it ranges between -79 and -85 mV. Cells from the pacemaker-conduction system slowly depolarize due to pacemaker currents until a threshold potential is exceeded, followed by a full action potential sequence. The rate of spontaneous depolarization determines the beating frequency of the heart. Ventricular cells lack these pacemaker currents. Their action is initiated by propagating electrical impulses from the pacemaker-conduction system.

After the threshold potential is actively exceeded, the upstroke (phase 0) of purkinje cells is carried by a rapid inward sodium current I_{Naf}. When the cell is depolarized, a transient outward current I_{Cl} that is carried by chloride and potassium ions causes a quick repolarization (phase 1). This is followed by a second inward current I_{si} which is mainly carried by calcium ions and marginally carried by sodium ions. It counteracts the outward directed slow and fast delayed rectifier potassium currents I_{x1} and I_{x2}, leading to a depolarized plateau (phase 2). The calcium influx during the plateau phase triggers a massive release of calcium as indicated in the figure by I_{CaSR} from the sarcoplasmic reticulum. The sarcoplasmic reticulum is an intracellular calcium store. Some of the calcium ions then bind to troponin C, thereby initiating the contraction process. Total action potential repolarization (phase 3) to the resting state occurs when the L-type calcium channels (Cav1.2) close. Further there are three background currents, a sodium current I_{Nab}, a potassium current I_{Kb} and a chloride current I_{Clb} that have only little influence on the action potential. Ion pumps and exchangers, e.g. the sodium-calcium exchanger and sodium-potassium ATPase, help regulating the ionic concentration gradients across the membrane in order to allow action potential sequences to occur physiologically identically.

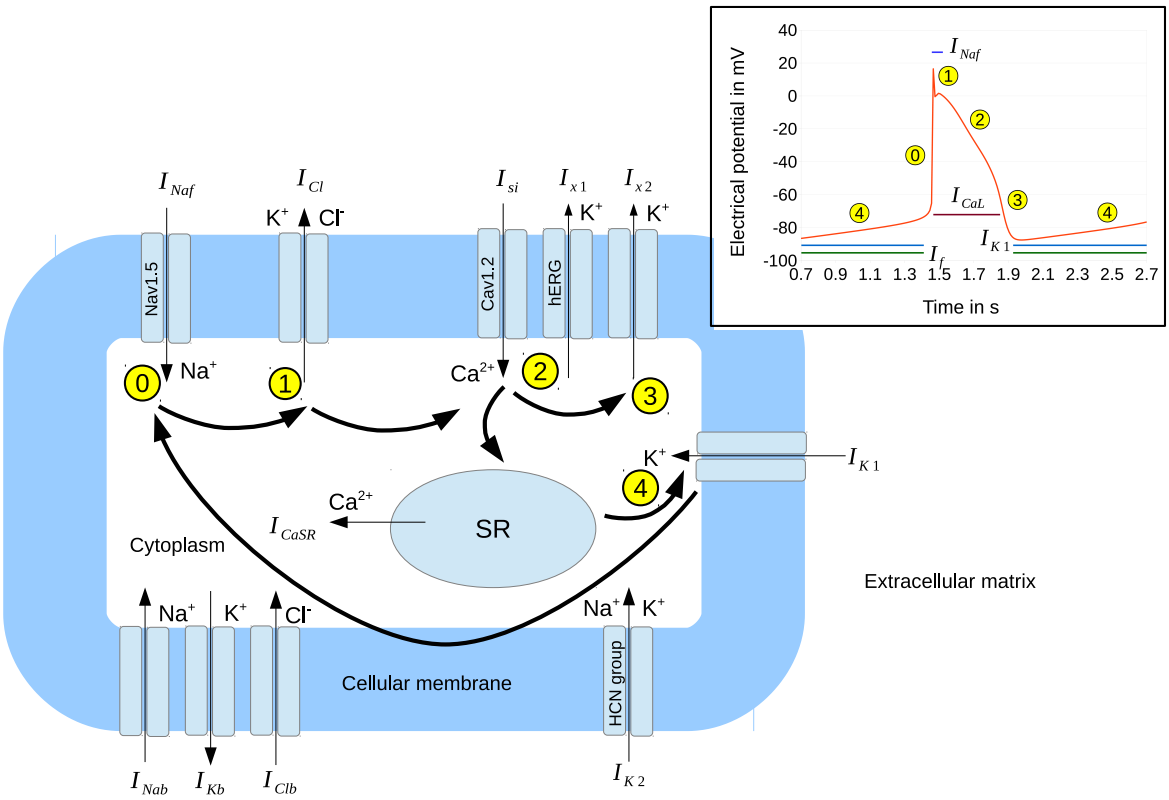

Figure 4.3: Electrophysiology of Purkinje cells, a typical action potential with phases 0–4 and major ion currents

4.2 Ventricular Cells

Ventricular cells are passively contractile cells of the mid wall of either the left or the right ventricle. Each of the ventricular walls, cf. fig. 4.1, consists of an endocardium, a myocardium and an epicardium, which are the inner, mid and outer wall, respectively. The cellular processes are very similar to the processes shown in fig. 4.3. The most important difference lies in the pacemaker current, that does not exist in this type of cell. The activation of ventricular cells (as of any other passively contractile kind of cell) needs to be triggered by electrical propagation of the action potential from the SA node through the whole heart. As a consequence the positive slope in phase 4 does not exist in ventricular cells.

4.3 Human-induced Pluripotent Stem Cell Derived Cardiomyocytes

Although they are not existing in a mammalian heart, human-induced pluripotent stem cell derived cardiomyocytes (hiPSC-CM) today are a valuable tool for investigating cardiac diseases, mutations and drug action. HiPS cells are cells that can be obtained by backwards differentiation followed by reprogramming of adult human cells. They are pluripotent stem

cells, meaning that they can be differentiated into any kind of cell existing in the human body. Since there are ethical concerns in performing experiments on native animal or human cells, the possibility of generating those cells from any cell, is brilliant and even brought the Nobel prize to Takahashi and Yamanaka [145].

When this method has been developed, of course it was questionable by what extent the hiPSC-CM functionally resemble native human cells. It has been shown that the differentiation of human embryonic pluripotent stem cells (hePSC) leads to functionally similar adult cells. However, again there are ethical concerns in obtaining ePSC. Thus, hiPS cells are commonly used instead of hePSC. In fact, one major problem in using hiPS cells is their immaturity or at least the unknown stage of maturity. This and the general applicability of experimental results obtained for hiPS cells to native human cells will be addressed at many points within this thesis.

Despite the known and unknown differences between native and differentiated induced cells they are commonly used because they are ethically acceptable. Thus they are currently used as models for native human cardiomyocytes in the investigation of cardiac diseases (Liang and Du [91]), of drug action (Liang et al. [92], Mehta et al. [104]) and the effect of mutations (Roden and Hong [128]).

4.4 Drug Action

The variety and the operating modes of known drugs are huge. Some drugs are acting somewhere in the metabolism, thereby having some influence to the cardiovascular system. Some other drugs occupy proteins in the cell membrane thus limit the availability of those proteins to other drugs. Both operation modes are not part of the investigations in this thesis. This work focuses on drugs that selectively influence specific ion channels with different intensity and depending on their concentration. Those drugs can be inhibitory and stimulating in the sense of blocking activation or inactivation gates (inhibition) or in the sense of accelerating the activation or inactivation of specific gates (stimulation). At the same time one drug can have an inhibitory behavior with respect to one gate and a stimulating behavior with respect to another gate with different potency. Both actions change the action potential, thus change the beating force and the heart rate (beating frequency). In the following paragraphs the drugs and their ways of action that are investigated within this thesis are explained.

4.4.1 Lidocaine

The common local anesthetic drug Lidocaine is clinically used as an antiarrhythmic drug for emergency-treatment of ventricular arrhythmias. As a Class IB antiarrhythmic agent, it binds to fast sodium channels (Nav1.5) in their inactivated state, thereby inhibiting their activation. Its effectivity strongly rises with increased heart rate and therefore it has a use-dependency. The block of fast sodium channels results in a decreased sodium influx I_{Na} during depolarization that subsequently causes a lowered inner calcium concentration in ventricular myocytes during the action potential plateau due to the reverse mode of

the sodium-calcium-exchanger as reported by Saleh et al. [134]. Lidocaine thus lowers ventricular contractile force.

Recent studies provide evidence for the inhibitory effect of Lidocaine on HCN channels which are assumed to be responsible for the pacemaker current thus the drug lowers the heart rate, Meng et al. [105].

4.4.2 Verapamil

Verapamil is a multi-ion-channel blocker classified as a class IV-antiarrhytmic agent. In cardiac tissue, this agent especially inhibits calcium ion influx through L-type calcium channels (Cav1.2) during the early plateau phase as well as potassium ion efflux through rapidly activating delayed rectifier potassium channels (hERG) during the late plateau and repolarization phases by dose-dependent blocking of the activation of the respective channels. This causes a slower repolarization-rate that in turn leads to an action potential prolongation. The action potential prolongation leads to the expectation that Verapamil induces a negative chronotropic effect, i.e. a reduction of the heart rate as found by Arnold et al. [4]. The decreased calcium influx yields a negative inotropic effect of Verapamil, i.e. a reduced beating force, since calcium ions play a major role in the contraction process. Kramer et al. [87] reported that the drug additionally blocks fast sodium channels (Nav1.5), but with a very low potency.

4.4.3 Veratridine

Veratridine is a sodium channel toxin that solely prolongates the permeability of fast sodium channels (Nav1.5) by drug-induced inhibition of channel inactivation, resulting in an increased inner sodium ion concentration as found by Brill and Wasserstrom [20] and Honerjäger and Reiter [74]. Saleh et al. [134] found that this consequently triggers an increase in intracellular calcium ions by stimulation of the sodium-calcium exchange and to an increased beating force. By an extension of the plateau phase, Veratridine additionally induces an action potential prolongation due to the lowered calcium influx which results in a decreased beating frequency as found by Arnold et al. [4].

4.4.4 Bay K8644

In calf and guinea pig myocardial cells, Bay K8644 has been found to be a L-type calcium channel agonist which increases the calcium concentration in the cell thus it is a positively inotropic substance (Thomas et al. [149]). The drug not only increases the open probability of the L-type calcium gates but also shifts the reversal potentials of the activation and inactivation gates to more negative voltages and accelerates the decay of this channel (Chen et al. [28]).

Kang et al. [82] and Ji et al. [80] found that Bay K8644 does not show the channel activating behavior in the case of hiPSC-CM and hePSC-CM. As this statement is not entirely true for all investigated cell cultures it is supposed that the lack of the effects in stem cell-derived cardiomyocytes was due to an immaturity of the cells.

5 Mechanical and Electrophysiological Modeling of Cardiac Tissue

From the modeling point of view cardiac tissue can be described by the three-element model of Hill [69] that has been established in 1938 and is shown in fig. 5.1. The model assumes a passive elastic element (PE) that is in parallel to a serial elastic (SE) element which is in series with a contractile element (CE). Although within this thesis it is applied to cardiac muscles only, Hill's model is a general model that describes the passive and active behavior of muscles, be they skeletal, smooth or cardiac muscles. The passive element mainly corresponds to the extracellular matrix (ECM) that provides passive stiffness by collagen, elastin and other proteins. Besides its mechanical role the ECM plays a huge role in shaping cells, it contains ions and regulates ion diffusion necessary for proper cellular function and it serves as a biological scaffold for the cells (Humphrey [77], Alberts et al. [3]). Its constituent collagen is a protein that, in an unloaded environment, is folded as can be seen in fig. 5.2. If the ECM, i.e. the tissue, is stretched, the collagen proteins will unfold thus provide an anisotropic structure to the tissue and develop an increasing stress. The corresponding nonlinear relationship between stress and strain can be seen in fig. 5.2 too. For small strains this relationship is highly flexible because the protein is still unfolding but as soon as the collagen fibers are properly aligned they produce an increasing stiffness.

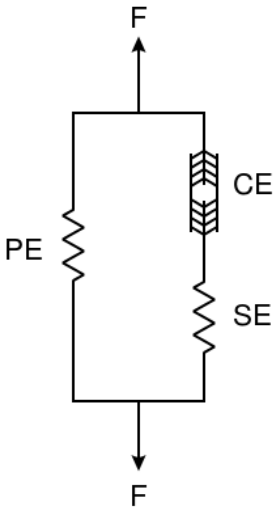

Figure 5.1: Hill's muscle model, Hill [69]

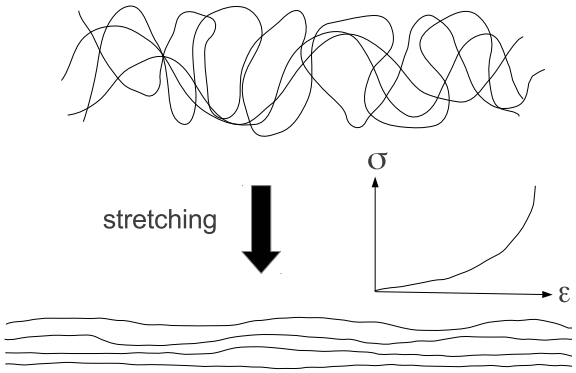

Figure 5.2: Collagen structure at rest and in stretching

In Hill's model the active component that is in parallel to the passive element also produces a passive stress via the serial element. This element can be identified with the inherent elasticity provided by cross-bridges that form during contraction. Cross-bridges are built by overlapping actin and myosin filaments, that, the more they overlap, increase the contraction force. This passive contribution of the active element usually is neglected because the passive stress that solely results from the contraction of the cells is rather small compared to the stress arising from the contractile component, i.e. the so-called

active stress.

In general the constitutive modeling of soft tissue is very flexible as can be seen for instance regarding the structural mechanically motivated approach presented in Böl et al. [16]. Therein a tetrahedral representative volume element has been created with truss elements lying on the edges of the tetrahedron. The volumetric stress contribution of the cardiac tissue is computed based on the tetrahedral element whereas the passive stress arising from the collagen fibers is reflected by the truss elements. The active stress component is also incorporated via fiber-oriented truss elements.

Computationally oriented discussions of skeletal, smooth and cardiac muscle structure and more details on the interpretation of Hill's model can be found in Spyrou [142]. Although cardiac muscle is in the focus of this thesis, the very clear and concise practical introduction of Martins et al. [101] into the modeling of skeletal muscle using Hill's model is worth reading and nearly fully valid for cardiac muscle. The main difference between skeletal and cardiac muscle cells is that some of the latter are able to beat autonomously whereas the former cells need to be activated through the nerve system.

5.1 Active Stress Formulation

From the mechanical point of view there are the so-called *active stress* and the *active strain* formulations. The majority today employs the former one. Following the suggestions in the cited literature, the active stress formulation is used herein but the active strain formulation is presented and discussed in the subsequent section. Therein the choice of the active stress formulation for the purposes of this thesis is justified.

The active stress formulation bases on the assumption that passive and active stresses occur separately and both lead to deformation, thus the Cauchy stress

$$\boldsymbol{\sigma} = \boldsymbol{\sigma}_p + \boldsymbol{\sigma}_a = 2J^{-1}\boldsymbol{b}\frac{\partial \Psi(\boldsymbol{b})}{\partial \boldsymbol{b}} - p\boldsymbol{I} + T(t,\boldsymbol{b})\boldsymbol{a}\otimes\boldsymbol{a} \tag{5.1}$$

is split up into a passive part $\boldsymbol{\sigma}_p$ and an active part $\boldsymbol{\sigma}_a$. In eq. (5.1), in the framework of hyperelasticity, the passive stress is expressed via the strain energy Ψ and the hydrostatic pressure p. The active stress is given by a time- and strain-dependent scalar quantity $T(t,\boldsymbol{b})$ that acts in a certain fiber direction $\boldsymbol{a}$.

Both, models for the passive and active stress contributions of cardiac muscles, have been presented in the literature. A very famous and often employed model for $\boldsymbol{\sigma}_p$ is a generalized version of the one shown in eq. (5.1). It has been proposed in Holzapfel and Ogden [73] and for incompressible soft biological tissue reads as

$$\begin{aligned}\boldsymbol{\sigma}_p = \quad & 2\frac{\partial \Psi}{\partial I_1}\boldsymbol{b} + 2\frac{\partial \Psi}{\partial I_2}(I_1\boldsymbol{b} - \boldsymbol{b}^2) - p\boldsymbol{I} + 2\frac{\partial \Psi}{\partial I_{4a}}\boldsymbol{a}\otimes\boldsymbol{a} + 2\frac{\partial \Psi}{\partial I_{4s}}\boldsymbol{s}\otimes\boldsymbol{s} \\ & + \frac{\partial \Psi}{\partial I_{8as}}(\boldsymbol{a}\otimes\boldsymbol{s} + \boldsymbol{s}\otimes\boldsymbol{a}) + \frac{\partial \Psi}{\partial I_{8an}}(\boldsymbol{a}\otimes\boldsymbol{n} + \boldsymbol{n}\otimes\boldsymbol{a})\,.\end{aligned} \tag{5.2}$$

Therein a sheet direction $\boldsymbol{s}$ that lies in the fiber plane and is normal to $\boldsymbol{a}$ and a normal direction $\boldsymbol{n}$ that is normal to both have been introduced and respective invariants I_* have

been formulated. This transversely isotropic stress formulation is much more sophisticated than the isotropic ones used herein but in turn it requires information about fiber orientation and the determination of many material parameters. It will become clear that for the investigations in this thesis, the four terms in eq. (5.2) that are associated with the anisotropy can be ignored. Nevertheless it should be mentioned that such a complex stress formulation should be employed in whole heart simulations as the anisotropy significantly influences the mechanical behavior.

The active stress contribution $\boldsymbol{\sigma}_a$ is detailed in sect. 5.4. The scalar T represents the contractile stress and is determined by a system of ordinary differential equations (ODE) that comprises ODEs describing the cellular electrophysiology, the action potential and the so-called excitation-contraction coupling which is the actual electromechanical coupling.

5.2 Active Strain Formulation

The active strain formulation originates from Nardinocchi and Teresi [109] and Cherubini et al. [29] who firstly proposed a multiplicative decomposition of the deformation gradient

$$\boldsymbol{F} = \boldsymbol{F}_e \boldsymbol{F}_a \,, \tag{5.3}$$

for the analysis of passive and active deformation. The idea is that the elastic part of the deformation gradient $\boldsymbol{F}_e$ produces all the stress and that the active part $\boldsymbol{F}_a$ does not deliver a stress contribution. The intermediate configuration that is created by $\boldsymbol{F}_a$ thus is considered to be *virtual*.

Very recently the active strain formulation has been applied to whole-heart simulations, like in Rossi et al. [131], Göktepe et al. [61] and Ruiz-Baier et al. [132] and to the simulation of isolated cardiomyocytes, cf. Ruiz-Baier et al. [133]. Especially Rossi et al. [131] theoretically compared multiple isotropic and anisotropic constitutive laws in the active stress and active strain frameworks. It comes out that in the small strain regime both are equivalent. In the finite strain regime though, they observe considerable differences in the deformation behavior that even become more severe when the constitutive law becomes more complicated. The main reason for this can be seen by comparing the first Piola-Kirchhoff stress in the active stress formulation

$$\boldsymbol{P} = \mu \boldsymbol{F} + T \boldsymbol{a} \otimes \boldsymbol{a}_0 \tag{5.4}$$

and the active strain formulation

$$\boldsymbol{P} = \mu(1 + \gamma_a)\boldsymbol{F} + \mu g(\gamma_a) \boldsymbol{a} \otimes \boldsymbol{a}_0 \tag{5.5}$$

for the very simple isotropic neo-Hookean material law. Interpreting γ_a as the relative displacement in the fiber axis one can clearly see that in eq. (5.5), in contrast to eq. (5.4), this relative displacement not only influences the anisotropic stress contribution but also the isotropic one by the factor of $(1 + \gamma_a)$. This basically means that an active contraction influences the passive material response as well, i.e. it modifies the stiffness of the material. The authors of the cited references leave open whether the active stress

or the active strain formulation is preferable. They suggest to conduct experiments that lead to this decision but this is still an open issue.

As already pointed out, within this thesis the active stress formulation is applied. It is preferable because it provides a disjunct split of passive and active stress contributions which is in accordance with the assumptions made in the experiments that serve for the parameterization of the employed models. It has to be mentioned though that the active strain formulation might be able to cover microstructural effects at the macro-level that would be disregarded in the active stress formulation. However, it seems to be much simpler to regard passive and active stresses as fully disjunct, both experimental- and interpretation-wise.

In the following sections the employed models for the passive stress are shown. The active stress contribution is in the main focus of this thesis and is discussed in very detail in the following sections as well.

5.3 Modeling the Passive Component

In soft tissue biomechanics the passive stress is usually represented by a hyperelastic constitutive law. As already indicated in eq. (5.1), hyperelastic constitutive laws are defined by a strain energy function Ψ that represents the energy stored in the material. Ψ can be expressed with the help of any strain measure and its derivative with respect to a certain strain measure leads to the dual (conjugate) stress. Therefore the first Piola-Kirchhoff stress is given as

$$\boldsymbol{P} = \frac{\partial \Psi(\boldsymbol{F})}{\partial \boldsymbol{F}} \tag{5.6}$$

and all other stress tensors can be derived using the transformation rules given in sect. 2.1.2. In terms of this thesis the second Piola-Kirchhoff stress

$$\boldsymbol{S} = \boldsymbol{F}^{-1} \frac{\partial \Psi(\boldsymbol{F})}{\partial \boldsymbol{F}} \tag{5.7}$$

and the Cauchy stress

$$\boldsymbol{\sigma} = J^{-1} \frac{\partial \Psi(\boldsymbol{F})}{\partial \boldsymbol{F}} \boldsymbol{F}^T \tag{5.8}$$

are of special interest. In general Ψ can be anisotropic, i.e. dependent on a number of fiber families, which is often the case for biological soft tissues like muscles (usually one fiber family) or blood vessels (multiple fiber families).

A very common constraint on biological soft tissues is the incompressibility of the tissue, i.e. $J = det(\boldsymbol{F}) = 1$. This constraint can be introduced into the strain energy function by a Lagrangian multiplier p

$$\Psi = \Psi(\boldsymbol{F}) - p(J - 1) \, , \tag{5.9}$$

which is known to be the hydrostatic pressure. In the remainder of this work only incompressible and isotropic materials will be examined. Although cardiac tissue in general is anisotropic, it will be shown in sec. 6.1 (cf. fig. 6.3) that the herein investigated tissue is

globally isotropic. Therefore a discussion of anisotropy and anisotropic models is beyond the scope of this thesis.

More on hyperelasticity and related topics can be found in HOLZAPFEL [72].

5.3.1 St. Venant-Kirchhoff

The St. Venant-Kirchhoff material is the generalization of Hooke's law to geometrically nonlinear problems. It is neither elliptic nor polyconvex (cf. e.g. EBBING [44] for proofs) which implies that existence and uniqueness of the solution cannot be guaranteed (MARSDEN AND HUGHES [100]). Moreover it has been shown in LE DRET AND RAOULT [88] that this material should be avoided if high compression is expected. The constitutive tensor in eq. (2.22) in matrix notation reads as

$$\mathbb{C} = \frac{E}{(1+\nu)(1-2\nu)} \begin{bmatrix} 1-\nu & \nu & \nu & 0 & 0 & 0 \\ \nu & 1-\nu & \nu & 0 & 0 & 0 \\ \nu & \nu & 1-\nu & 0 & 0 & 0 \\ 0 & 0 & 0 & 1-2\nu & 0 & 0 \\ 0 & 0 & 0 & 0 & 1-2\nu & 0 \\ 0 & 0 & 0 & 0 & 0 & 1-2\nu \end{bmatrix} , \tag{5.10}$$

with Young's modulus E and Poisson ratio ν. The (quasi-)incompressible case is achieved if ν tends to 0.5 and it leads to numerical problems because the denominator in eq. (5.10) approaches zero. A possible remedy is a reformulation such that the strain energy for the St. Venant-Kirchhoff material reads as

$$\Psi = \frac{\lambda}{2}(\mathrm{tr}(\boldsymbol{E})^2) + \mu \mathrm{tr}\boldsymbol{E}^2 , \tag{5.11}$$

with the Lamé constants λ and μ that are related to E and ν as

$$\lambda = \frac{E\nu}{(1+\nu)(1-2\nu)}, \qquad \mu = \frac{E}{2(1+\nu)} . \tag{5.12}$$

In order to take the derivative of eq. (5.11) with respect to the Green-Lagrangian strain tensor it is important to know that

$$\frac{\partial \mathrm{tr}(\boldsymbol{E})}{\partial \boldsymbol{E}} = \frac{\partial E_{ii}}{\partial E_{kl}} = \boldsymbol{I} . \tag{5.13}$$

Using this the second Piola-Kirchhoff stress for St. Venant-Kirchhoff material can be derived as

$$\boldsymbol{S} = \frac{\partial \Psi(\boldsymbol{E})}{\partial \boldsymbol{E}} = \lambda \mathrm{tr}(\boldsymbol{E})\boldsymbol{I} + 2\mu \boldsymbol{E} . \tag{5.14}$$

Here, $\boldsymbol{S}$ is expressed in terms of the Green-Lagrangian strain but it can easily be shown that this expression is equivalent to the original representation in terms of the deformation

gradient (cf. eq. (5.7)),

$$\begin{aligned} \boldsymbol{S} &= \frac{\partial \Psi(\boldsymbol{E})}{\partial \boldsymbol{E}} = \frac{\partial \Psi(\boldsymbol{E})}{\partial \boldsymbol{F}} \frac{\partial \boldsymbol{F}}{\partial \boldsymbol{E}} = \left(\frac{\partial \boldsymbol{E}}{\partial \boldsymbol{F}} \right)^{-1} \frac{\partial \Psi(\boldsymbol{F})}{\partial \boldsymbol{F}} \\ &= \left(\frac{1}{2} \frac{\partial \left(\boldsymbol{F}^T \boldsymbol{F} - \boldsymbol{I} \right)}{\partial \boldsymbol{F}} \right)^{-1} \frac{\partial \Psi(\boldsymbol{F})}{\partial \boldsymbol{F}} \\ &= \boldsymbol{F}^{-1} \frac{\partial \Psi(\boldsymbol{F})}{\partial \boldsymbol{F}} \, . \end{aligned} \tag{5.15}$$

Herein the fact has been used that Ψ is defined in a way that it stays unchanged under rotation, i.e. $\Psi(\boldsymbol{F}) = \Psi(\boldsymbol{RF})$. Consequently all the different functions

$$\Psi(\boldsymbol{F}) = \Psi(\boldsymbol{U}) = \Psi(\boldsymbol{V}) = \Psi(\boldsymbol{C}) = \Psi(\boldsymbol{b}) = \Psi(\boldsymbol{E}) \tag{5.16}$$

have the same value. This originates from the fact that with the polar decompositions $\boldsymbol{F} = \boldsymbol{RU}$ and $\boldsymbol{F} = \boldsymbol{VR}$ of the deformation gradient tensor into an orthogonal rotation tensor $\boldsymbol{R}$ and a right and left stretch tensor $\boldsymbol{U}$ and $\boldsymbol{V}$, respectively, the strain tensors

$$\boldsymbol{C} = \boldsymbol{F}^T \boldsymbol{F} = \boldsymbol{R} \boldsymbol{U}^T \boldsymbol{R} \boldsymbol{U} = \boldsymbol{U}^T \boldsymbol{R}^T \boldsymbol{R} \boldsymbol{U} = \boldsymbol{U}^T \boldsymbol{U} \, , \tag{5.17}$$

$$\boldsymbol{b} = \boldsymbol{F} \boldsymbol{F}^T = \boldsymbol{V} \boldsymbol{R} \boldsymbol{V} \boldsymbol{R}^T = \boldsymbol{V} \boldsymbol{R} \boldsymbol{R}^T \boldsymbol{V}^T = \boldsymbol{V} \boldsymbol{V}^T \text{ and} \tag{5.18}$$

$$\boldsymbol{E} = \frac{1}{2}(\boldsymbol{C} - \boldsymbol{I}) = \frac{1}{2}(\boldsymbol{U}^T \boldsymbol{U} - \boldsymbol{I}) \tag{5.19}$$

can be expressed independently of the rotation tensor. Intuitively it is clear that, in statics, rigid body rotation or translation does not cause any stress.

Taking the second derivative of Ψ with respect to $\boldsymbol{E}$ gives the constitutive tensor

$$\mathbb{C} = \frac{\partial \boldsymbol{S}}{\partial \boldsymbol{E}} = \frac{\partial^2 \Psi(\boldsymbol{E})}{\partial \boldsymbol{E}^2} = \lambda \boldsymbol{I} \otimes \boldsymbol{I} + 2\mu \boldsymbol{I} \otimes \boldsymbol{I} = (\lambda + 2\mu) \mathbb{S} \, , \tag{5.20}$$

where the symmetric fourth-order tensor $\mathbb{S}$ has the components

$$S_{ijkl} = \frac{1}{2}(\delta_{ik}\delta_{jl} + \delta_{il}\delta_{jk}) \tag{5.21}$$

and replaces the fourth-order identity tensor because $\boldsymbol{E}$ and $\boldsymbol{S}$ are symmetric. Equation (5.20) is equivalent to eq. (5.10). Both equations show that the St. Venant-Kirchhoff material is isotropic and the material properties are strain-independent. Recapitulating fig. 5.2, neither isotropy nor independence of strain can be assumed for cardiac tissue. Nevertheless this material model is useful for describing material in the linear regime. Regarding its limitations that already have been indicated above, the St.Venant-Kirchhoff material model should only be used for boundary value problems with large rotations but small strains.

It can be shown that if a polyconvex or a quasiconvex strain energy density is required in the isotropic hyperelastic case, then the stress-strain relationship must be physically nonlinear in the nonlinear strain measure.

5.3.2 Neo-Hookean

The Neo-Hookean material model is the simplest strain-dependent model and it can be viewed as a special case of the general Ogden model

$$\Psi = \Psi(\lambda_1, \lambda_2, \lambda_3) = \sum_{p=1}^{n} \frac{\mu_p}{\alpha_p}(\lambda_1^{\alpha_p} + \lambda_2^{\alpha_p} + \lambda_3^{\alpha_p} - 3) \ , \tag{5.22}$$

with the principal stretches λ_i, shear moduli μ_p and dimensionless parameters α_p. Setting $N = 1$ and $\alpha_1 = 2$ leads to

$$\Psi(\lambda_1, \lambda_2, \lambda_3) = \frac{\mu_1}{2}(\lambda_1^2 + \lambda_2^2 + \lambda_3^2 - 3) = C_{10}(I_1 - 3) = \Psi(I_1) \ , \tag{5.23}$$

with $I_1(\boldsymbol{C}) = \mathrm{tr}(\boldsymbol{C})$ the first invariant of the right Cauchy-Green tensor.

This hyperelastic strain energy function in terms of the first invariant or the principal stretches is commonly used thus the passive stress contribution in eq. (5.1) has to be reformulated in terms of λ_i too. Using the identities derived in sect. 5.3.1 one gets

$$\begin{aligned}
\boldsymbol{\sigma}_p &= 2J^{-1}\boldsymbol{b}\frac{\partial\Psi(\boldsymbol{b})}{\partial\boldsymbol{b}} - p\boldsymbol{I} = 2J^{-1}\boldsymbol{V}\boldsymbol{V}^T\frac{\partial\Psi(\boldsymbol{V})}{\partial\boldsymbol{V}}\frac{\partial\boldsymbol{V}}{\partial\boldsymbol{b}} - p\boldsymbol{I} \\
&= 2J^{-1}\boldsymbol{V}\boldsymbol{V}^T\frac{\partial\Psi(\boldsymbol{V})}{\partial\boldsymbol{V}}\left(\frac{\partial\boldsymbol{b}}{\partial\boldsymbol{V}}\right)^{-1} - p\boldsymbol{I} = J^{-1}\boldsymbol{V}\boldsymbol{V}^T\frac{\partial\Psi(\boldsymbol{V})}{\partial\boldsymbol{V}}\boldsymbol{V}^{-1} - p\boldsymbol{I} \\
&= J^{-1}\boldsymbol{V}\frac{\partial\Psi(\boldsymbol{V})}{\partial\boldsymbol{V}} - p\boldsymbol{I} \ .
\end{aligned} \tag{5.24}$$

The final step is to simply replace the left stretch tensor by its eigenvalues because $\boldsymbol{\sigma}_p$ shall be expressed in its principal directions. The passive stress contribution then reads as

$$(\boldsymbol{\sigma}_p)_i = J^{-1}\lambda_i\frac{\partial\Psi}{\partial\lambda_i} - p\delta_{ii} \ , \tag{5.25}$$

with $J = \lambda_1\lambda_2\lambda_3$. Of course there are many more different hyperelastic models for soft tissues. Major benefits of the Neo-Hookean model are that it is polyconvex and that only one parameter C_{10} needs to be determined by parameter fitting. On the other hand more complex models allow a better approximation of the material curve if it has regions of largely differing slopes, i.e. different degrees of nonlinearity. In the application that is investigated within this thesis the material behavior can accurately be approximated by the Neo-Hookean material thus more complex models are not required.

The problems that are investigated in this thesis are modeled with either the St. Venant-Kirchhoff material for small deformation but large displacement or the Neo-Hookean material for large deformation problems.

5.4 Modeling the Contractile Component

The modeling of the contractile element in Hill's model is most important for this thesis. This part of the model strongly depends on the type of muscle (skeletal, smooth or cardiac)

and on the cell type because the action potentials of different cells in the heart, like AV cells, SA cells, Purkinje cells or ventricular cells differ significantly. It has already been explained that the main driver for the contractility of any cardiac cell is the concentration of free inner calcium.

In standard tissue models one uses an electrophysiological model of a specific cell type in order to create an action potential and to compute the free inner calcium concentration $[Ca^{2+}]_i$, which then serves as input for the computation of the active stress contribution $\boldsymbol{\sigma}_a$ in eq. (5.1).

There are different ways of modeling cell electrophysiology, cf. Ay and Arnosti [5], but most commonly the electrophysiological processes across the cell membrane (cf. fig. 4.3) are modeled by a system of ordinary differential equations in the form of

$$\frac{dV_m}{dt} = \frac{1}{C_m}\left(I_{stim} - \sum_{i=1}^{M} I_i(g_1, g_2, ..., g_{M_i})\right) \tag{5.26}$$

$$\frac{dg_j(V_m)}{dt} = \alpha_j^+(V_m)(1-g_j) + \alpha_j^-(V_m)g_j \ , \tag{5.27}$$

where V_m is the cell membrane potential, C_m is the electrical capacitance of the cell membrane, I_{stim} is an external (potentially zero) electrical stimulus, I_i are ionic currents and M is the total number of ionic currents in the model. Each current depends on M_i (usually one or two) gate variables g_j that control the opening and closure of the ionic channel i where ions diffuse through. α_j^+ and α_j^- are experimentally determined opening and closure rates of the respective gate. They depend on V_m, i.e. for each gate there are threshold values for the membrane potential that determine the opening and closure of the respective gate.

The membrane potential itself is determined by the difference of an externally applied current I_{stim} and the ionic currents that are governed by the gates. The idea for this very general electrophysiological model for a single cell goes back to Hodgkin and Huxley [71]. Since then numerous special single-cell models have been developed based on an immense amount of experiments to determine the electrical, mechanical and electromechanical properties of cells and single ion channels. As the knowledge of cellular processes is still incomplete but continuously increasing the quantification of the properties is work in progress. Extensive overviews over electrophysiological cell models of different mammalian and human cell types that also have been used to study the electrical propagation in cardiac tissues are provided by Fenton and Cherry [49] and Nickerson [115]. Those models have different complexity, ranging from two variables to very complex models that consist of up to 60 variables. They are too numerous to name them all, i.e. only the models that have been used in this work will be explained.

As already indicated in Ruiz-Baier et al. [132], currently there is no model that properly builds the bridge between the cell and tissue scales by means of homogenization. Usually the micro-scale effects are directly transmitted to the macro-scale, i.e. concerning the contractile behavior, the tissue is treated as if it would consist of cells only, without an extracellular matrix. Those models are referred to as monodomain models. In order to benefit from the detailed data on the cell level in tissue analysis, a switchover

to bidomain models is important. The theoretical background of which can be found in Nobile et al. [119].

5.4.1 Different Scales

At first one has to distinct between the modeling on different scales. There are approaches of modeling optical effects on the Ångström to the nano-scale to achieve realistic multi-scale behavior of the heart. Chemical processes like diffusion of ions through the ion channels of the cell take place on the nano- to the micro-scale. Within this thesis chemical processes are modeled at the cell level (micro-scale) ignoring the local effects that take place at the nano-scale. The chemical and electrophysiological cellular processes are much faster than the mechanical response of the tissue. Therefore the tissue which consists of millions of cells is not only modeled on a coarser length scale but also on a coarser time scale. Crossing the scales is rather simple in the model developed herein.

An even larger scale is the organ itself. For basic investigations like the simulation of drug action on a tissue this scale is too large regarding the fact that cellular processes are not entirely understood and that corresponding models are under current development. Some research has been done in the simulation of the mechanics and the propagation of the electrical potential through the human heart including mechano-electrical feedback, like Göktepe and Kuhl [59], Hunter et al. [79] and Smith et al. [141] but mostly without crossing the scales to the cell level. An exception to that is the recently proposed framework by Göktepe et al. [61] that allows for internal ordinary differential equation systems describing the cellular electrophysiology.

Computational models at the tissue and organ level are often chosen for the investigation of the electromechanics of the whole heart, i.e. when the organ deformation, the electrical conduction system or mechano-electrical effects are of interest. Models at the cellular level are employed when individual ion currents, specific gates or proteins, the cellular action potential or the cellular communication via gap junctions are studied. Cellular models are often used for the computational assessment of single cells, cell clusters or even tissue, like in the present case. Fully bridging the scales from the cellular level up to the organ level is very challenging and is discussed in the outlook section 9 as a current research topic.

5.4.2 Modeling Drug Action

Before starting to explain the chosen electrophysiological models, the general way of modeling drug action within the Hodgkin-Huxley framework shall be clarified.

Different drugs typically have different effects on the membrane potential. First of all, a drug may change the activation or inactivation gate of a certain channel or possibly multiple gates in a varying amount. The two basic effects that are investigated are the blocking and the stimulation of the activation or the inactivation of a certain gate, respectively. The modeling approaches of both are different and strongly depend on the data that is taken from experiments.

5.4.2.1 Blocking Drugs In patch clamp experiments one quantifies an IC_{50} value which is the half-blocking concentration of a drug with respect to a certain gate. In other words the IC_{50} value is the concentration of the drug that is needed to slow down the ion flux through the respective channel by 50%. Knowing the constant IC_{50} value that for instance can be taken from literature and the actually applied drug concentration D, Obiol-Pardo et al. [121] simply introduce a scaling factor into the respective gate differential equation (5.27)

$$\frac{dg_j(V_m; IC_{50}^d, D^d)}{dt} = \frac{1}{1 + \frac{D^d}{IC_{50}^d}} \left(\alpha_j^+(V_m)(1 - g_j) + \alpha_j^-(V_m)g_j\right) . \tag{5.28}$$

Obviously this scaling factor equals 0.5 (half-blocking) if $D^d = IC_{50}^d$, where the upper index d indicates a specific drug. One has to be very careful in searching appropriate IC_{50} values. This experimentally determined parameter depends on the drug, the ion channel, the cell type, the cell environment, stretch, etc. Depending on the numerous influences, values from different publications that seem to be determined in a similar environment often lie in a wide range.

5.4.2.2 Stimulating Drugs Stimulating effects of drugs are modeled in a different way. Experimentally one observes that either the opening rate α_j^+ or the closure rate α_j^- or both are affected by a drug. Those rates are often defined with respect to a threshold potential. Thus if V_m reaches the threshold potential the gate opens. In patch clamp experiments one can measure a shift of a test action potential with respect to the drug concentration. The determined potential shifts ΔV_j^+ and ΔV_j^- are added in order to modify the threshold. Intuitively it is clear that if the gate becomes activated at a lower potential, i.e. it opens earlier, and if the inactivation stays unchanged, then the gate will be in the open state for a longer time, which has a positive effect on the ion flux. The same is true for unchanged activation but later inactivation (at higher potentials). The gate differential equation including the potential shift is introduced as

$$\frac{dg_j(V_m)}{dt} = \alpha_j^+(V_m + \Delta V_j^+)(1 - g_j) + \alpha_j^-(V_m + \Delta V_j^-)g_j . \tag{5.29}$$

Depending on the affected ion channel, a potential shift might result in a changing beating force or beating frequency of the cell. Of course both effects can be seen at the same time, especially if the drug acts on a specific calcium channel and on a specific potassium channel, the latter of which often is called the *pacemaker* channel. Also, there is the well known *staircase* effect that reveals a positive proportionality of cell beating force with respect to the beating frequency.

From a modeling point of view one has to be very cautious about how the drug is supposed to change the cellular processes and where in the model this effect can be introduced and about the experimentally determined potential shifts that again underlie uncertainties. The application of multiple drugs at the same time with opposing effects is possible in general but has not been investigated in here.

5.4.3 Electrophysiological Models

In order to understand how the choice of the proper cell models for the purposes of this thesis have been made, it is necessary to provide an overview about the currently existing models. Models for SA cells and ventricular cells are in the focus because those are the investigated cell types.

The first model that has been implemented during this work is the Fenton-Karma model Fenton and Karma [48] for ventricular cells representing a fast-inward, a slow-inward and a slow-outward current. Each of those three currents represents an assembly of a number of ion currents. In the view of simulation of drug action the level of detail of the Fenton-Karma model is not sufficient because drugs selectively act on ion channels and in order to simulate this appropriately the respective ion channels need to have a separate representation. Moreover this model represents ventricular cells which are not autonomously beating but which need a trigger from outside. In the human heart as well as in the investigated tissues the stimulus originates from nodal cells, like SA cells.

For the sake of simplicity, models have been chosen that do not have much more than 20 unknowns in total. For the investigations in this thesis a higher degree of detail is not necessary and may be even confusing. It is already difficult to find reliable experimental data concerning action potentials of and drug action on different type of cells. The unreliability originates from different factors like the cell environment, species, uncertainty of cell type, the influence of the respective experimental setup and whether the experiments are performed on the level of single ion channels, single cells, tissues or organs. Especially the herein investigated human-induced pluripotent stem cells (hiPSC) show considerably different behavior depending on those and other factors because all over the world they have a different origin. Given the fact that it is very difficult to select appropriate data for hiPS cells from the literature, it is important to keep the models simple in order to provide a certain range of applicable data instead of not being able to find any data.

Besides those concerns there is another one that has already been mentioned: the difference between hiPS cells and native human cells thus the applicability of results obtained with hiPS cells. Although they provide a good and promising basis for ethically beneficial experiments they are functionally different or immature. Recent experimental and simulation studies like Ji et al. [80] and Hu et al. [75], respectively, show that currently it is dangerous trying to transfer hiPSC results to native cells as largely significant functional differences can be seen between different cell lines and even within one cell line.

In order to understand the basic properties of self-contractile cell models, two models for Purkinje fiber cells have been implemented: the Noble model, Noble [120] and the McAllister-Noble-Tsien (MNT) model, McAllister et al. [103]. The former one again is a very simple model having only four variables and therefore is not well-suited for the simulation of drug action. The MNT model was the first model that has been used herein to simulate self-contractile tissue and drug action.

During data evaluation it appeared that the calcium dynamics needed to be simulated in much more detail than it has been done in this first setup. In addition to that the investigated tissues consist of multiple different cell types: nodal, atrial and ventricular CM

as well as fibroblasts. Taking this into account two more recent models have been selected and implemented. The model of STEWART ET AL. [143] is a Purkinje fiber model, just like the MNT model. This model has been chosen because it models the calcium dynamics in much more detail and because it is parameterized based on data of human Purkinje fiber cells in contrast to the MNT model that is mostly based on rabbit and canine data. In the finite element model the Stewart model serves as the pacemaker without a geometrical representation. In turn, the human ventricular model of TEN TUSSCHER ET AL. [147] and TEN TUSSCHER AND PANFILOV [146] (TT) is applied everywhere to simulate the cardiac action potential.

Choosing a Purkinje fiber model instead of a proper nodal model seems to be arbitrary. During the work on the thesis the MNT model for Purkinje cells has been chosen because of its limited number of ionic currents such that basic electrophysiological effects are clearly represented. Later, when a human model was required, the differences to the MNT model should be as little as possible in order to be able to keep track of the changes in the results. Thus, in order to keep the cell type, a consequent choice was the Stewart model for human Purkinje cells. It will be pointed out in sections 5.4.5 and 9.2.2 that human SA models have been chosen for further investigations that extend this thesis.

The three models, MNT, Stewart and TT, that have been used in the simulations are explained in the following paragraphs.

5.4.3.1 McAllister-Noble-Tsien The MNT model proposed in MCALLISTER ET AL. [103] consists of ten variables and therefore it is sufficiently complex to appropriately simulate drug action but not too complex to be confusing concerning the adjustable parameters. Here, the equations and parameters of the original model are shown. If different parameters have been used (NICKERSON [115] shows some minor differences) it is explicitly stated. The following equations form a model for the cellular processes that have been described with the help of fig. 4.3 and the action potential one can compute from this model is shown in fig. 5.3. The different phases of the AP have been explained in sect. 4.1 and it shall be emphasized here that one can clearly observe a rising of the AP before depolarization and after the beat. Consequently, the model will reach its threshold potential on its own and beats with a frequency of about 0.77 s^{-1}.

Disregarding the units in eqs. (5.30–5.38) for compactness, the ion currents in the MNT

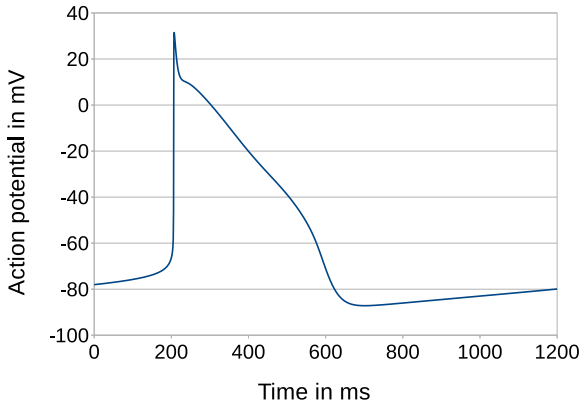

Figure 5.3: Action potential of the McAllister model

model are

$$I_{Na} = c_{Na} g_m^3 g_h (V_m - V_m^{Na}) , \tag{5.30}$$

$$I_{si} = c_{si} g_d g_f (V_m - V_m^{si}) + c_{si}^* \left(1 + exp\left(-\frac{V_m + 40}{6.667}\right)\right)^{-1} (V_m - V_m^{si}) , \tag{5.31}$$

$$I_{K2} = 0.028 g_s \frac{exp\left(\frac{V_m - V_m^K}{25}\right) - 1}{exp\left(\frac{V_m + 60}{12.5}\right) + exp\left(\frac{V_m + 60}{25}\right)} , \tag{5.32}$$

$$I_{x1} = 0.012 g_{x1} \frac{exp\left(\frac{V_m + 95}{25}\right) - 1}{exp\left(\frac{V_m + 45}{25}\right)} , \tag{5.33}$$

$$I_{x2} = g_{x2}(0.25 + 0.00385 V_m) , \tag{5.34}$$

$$I_{qr} = c_{qr} g_q g_r (V_m - V_m^{Cl}) , \tag{5.35}$$

$$I_{K1} = \left(\frac{I_{K2}}{2.8} + 0.002 \frac{V_m - V_m^{K1}}{1 - exp\left(-\frac{V_m - V_m^{K1}}{25}\right)}\right) , \tag{5.36}$$

$$I_{Nab} = c_{Nab} (V_m - V_m^{Na}) , \tag{5.37}$$

$$I_{Clb} = c_{Clb} (V_m - V_m^{Cl}) , \tag{5.38}$$

with $c_{Na} = 1.5\, mS\, mm^{-2}$, $V_m^{Na} = 40\, mV$, $c_{si} = 0.008\, mS\, mm^{-2}$, $c_{si}^* = 0.0004\, mS\, mm^{-2}$, $V_m^{si} = 70\, mV$, $V_m^K = -110\, mV$, $c_{qr} = 0.05\, mS\, mm^{-2}$, $V_m^{Cl} = -70\, mV$, $V_m^{K1} = -30\, mV$, $c_{Nab} = 0.00105\, mS\, mm^{-2}$ and $c_{Clb} = 0.0001\, mS\, mm^{-2}$. The interpretation of those currents can be found in fig. 4.3 with the difference that therein, I_{Naf} and I_{Nas} correspond to I_{Na} and I_{si}, respectively, in the MNT model. From those naming conventions one major drawback of the MNT model can already be seen. The *slow inward* current I_{si} represents the sum of slow sodium and calcium processes (sodium influx, sodium-calcium-exchanger, calcium-induced calcium release of the SR) thereby hiding and averaging important parts of the cellular process. As this model is balanced in a way such that it is self-contractile with a certain frequency no external stimulus is needed. The beating frequency depends on the parameterization of the model and can indirectly be changed for instance by drug

application or other parameter adjustments. By setting $C_m = 0.1\,\mu F\,mm^{-2}$ the currents (5.30)–(5.38) determine the time course of the membrane potential, eq. (5.26).

To complete the model the activation and inactivation parameters of the nine gates of this model are shown. Again, the units are ommited:

$$\alpha_m^+ = \frac{V_m + 47}{1 - exp\left(-\frac{V_m+47}{10}\right)} \qquad \alpha_m^- = 9.86 exp\left(-\frac{V_m + 47}{17.86}\right) \tag{5.39}$$

$$\alpha_h^+ = 1.13 \cdot 10^{-7} exp\left(-\frac{V_m + 10}{5.43}\right) \qquad \alpha_h^- = 2.5\left(1 + exp\left(-\frac{V_m + 10}{12.2}\right)\right)^{-1} \tag{5.40}$$

$$\alpha_d^+ = 0.002\frac{V_m + 40}{1 - exp\left(-\frac{V_m+40}{10}\right)} \qquad \alpha_d^- = 0.02 exp\left(-\frac{V_m + 40}{11.26}\right) \tag{5.41}$$

$$\alpha_f^+ = 0.00253 exp\left(-\frac{V_m + 26}{25}\right) \qquad \alpha_f^- = 0.02\left(1 + exp\left(-\frac{V_m + 26}{11.49}\right)\right)^{-1} \tag{5.42}$$

$$\alpha_q^+ = 0.008\frac{V_m}{1 - exp\left(-\frac{V_m}{10}\right)} \qquad \alpha_q^- = 0.08 exp\left(-\frac{V_m}{11.26}\right) \tag{5.43}$$

$$\alpha_r^+ = 2.08 \cdot 10^{-5} exp\left(-\frac{V_m + 26}{25}\right) \qquad \alpha_r^- = 0.02\left(1 + exp\left(-\frac{V_m + 26}{11.49}\right)\right)^{-1} \tag{5.44}$$

$$\alpha_s^+ = 0.001\frac{V_m + 52}{1 - exp\left(-\frac{V_m+52}{5}\right)} \qquad \alpha_s^- = 5 \cdot 10^{-5} exp\left(-\frac{V_m + 52}{14.93}\right) \tag{5.45}$$

$$\alpha_{x1}^+ = 5 \cdot 10^{-4}\frac{exp\left(\frac{V_m+50}{12.1}\right)}{1 + exp\left(\frac{V_m+50}{17.5}\right)} \qquad \alpha_{x1}^- = 0.0013\frac{exp\left(-\frac{V_m+20}{16.67}\right)}{1 + exp\left(-\frac{V_m+20}{25}\right)} \tag{5.46}$$

$$\alpha_{x2}^+ = 1.27 \cdot 10^{-4}\left(1 + exp\left(-\frac{V_m + 19}{5}\right)\right)^{-1} \qquad \alpha_{x2}^- = 3 \cdot 10^{-4}\frac{exp\left(-\frac{V_m+20}{16.67}\right)}{1 + exp\left(-\frac{V_m+20}{25}\right)} \tag{5.47}$$

Each gate is expressed in the form of eq. (5.27). In order to couple this model to the models of contraction described in sect. 5.4.4, another ordinary differential equation needs to be introduced that determines the inner calcium concentration. In the model of contraction the calcium concentration at a certain time serves as direct input. Unlike other models the MNT model does not provide such a differential equation but in Beeler and Reuter [9] the differential equation

$$\frac{\partial [Ca^{2+}]_i}{\partial t} = -1.848 \cdot 10^{-4} I_{si} + 0.07(10^{-4} - [Ca^{2+}]_i) \tag{5.48}$$

has been proposed that uses I_{si} as input. Here it has already been scaled to a minimum calcium concentration of $0.1\,\mu$M and a maximum calcium concentration of $1\,\mu$M. Any other scaling is also possible depending on the cell type to model.

5.4.3.2 ten Tusscher et al. This model of human ventricular cells consists of 17 variables that are explained in detail in ten Tusscher and Panfilov [146]. The time

course of the membrane potential is determined by a total of 12 ion currents and a possible stimulus. As TEN TUSSCHER ET AL. [147] and TEN TUSSCHER AND PANFILOV [146] are very detailed, within this thesis only some ion currents and some specific gates are explained depending on whether they are influenced by a drug. However, all the differential equations are shown here because they slightly differ from those shown in the cited papers due to minor mistakes that have been corrected in NIEDERER AND SMITH [116]. Each of the gate differential equations is written in the form

$$\frac{\partial g_j(V_m)}{\partial t} = \frac{g_j^{inf} - g_j}{\tau_{g_j}} \,, \tag{5.49}$$

with time constants

$$\tau_{g_j} = \alpha_{g_j}^{+}\alpha_{g_j}^{-} + \beta_{g_j}^{-} \tag{5.50}$$

for most of the gates except for the j- and h-gates for which

$$\tau_{g_j} = \frac{1}{\alpha_{g_j}^{+} + \alpha_{g_j}^{-}} \,. \tag{5.51}$$

Avoiding the units in the equations of this section as well, the activation and inactivation constants $\alpha_{g_j}^{+}, \alpha_{g_j}^{-}$ and $\beta_{g_j}^{-}$ for each gate are given as follows

$$\alpha_m^{+} = \frac{1}{1 + exp\left(-\frac{V_m+60}{5}\right)} \qquad \alpha_m^{-} = \frac{0.1}{1 + exp\left(\frac{V_m+35}{5}\right)} + \frac{0.1}{1 + exp\left(\frac{V_m-50}{200}\right)}$$

$$\beta_m^{-} = 0 \qquad m_{inf} = \frac{1}{\left(1 + exp\left(-\frac{V_m+56.86}{9.03}\right)\right)^2}$$

$$\alpha_d^{+} = \frac{1.4}{1 + exp\left(-\frac{V_m+35}{13}\right)} + 0.25 \qquad \alpha_d^{-} = \frac{1.4}{1 + exp\left(\frac{V_m+5}{5}\right)}$$

$$\beta_d^{-} = \frac{1}{1 + exp\left(\frac{50-V_m}{20}\right)} \qquad d_{inf} = \frac{1}{1 + exp\left(-\frac{V_m+8}{7.53}\right)}$$

$$\alpha_{x1}^{+} = \frac{450}{1 + exp\left(-\frac{V_m+45}{10}\right)} \qquad \alpha_{x1}^{-} = \frac{6}{1 + exp\left(\frac{V_m+30}{11.5}\right)}$$

$$\beta_{x1}^{-} = 0 \qquad x1_{inf} = \frac{1}{1 + exp\left(-\frac{V_m+26}{7}\right)}$$

$$\alpha_{x2}^{+} = \frac{3}{1 + exp\left(-\frac{V_m+60}{20}\right)} \qquad \alpha_{x2}^{-} = \frac{1.12}{1 + exp\left(\frac{V_m-60}{20}\right)}$$

$$\beta_{x2}^{-} = 0 \qquad x2_{inf} = \frac{1}{1 + exp\left(\frac{V_m+88}{24}\right)}$$

$$\alpha_{xs}^{+} = \frac{1400}{\sqrt{1 + exp\left(\frac{5-V_m}{14}\right)}} \qquad \alpha_{xs}^{-} = \frac{1}{1 + exp\left(\frac{V_m-35}{15}\right)}$$

$$\beta_{xs}^{-} = 80 \qquad xs_{inf} = \frac{1}{1 + exp\left(-\frac{V_m+5}{14}\right)}$$

$$\alpha_h^+ = \begin{cases} 0.057exp\left(-\frac{V_m+80}{6.8}\right), & V_m < -40 \\ 0, & \text{else} \end{cases}$$

$$\alpha_h^- = \begin{cases} 2.7exp(0.079V_m) + 310000exp(0.3485V_m), & V_m < -40 \\ \frac{0.77}{0.13(1+exp\left(-\frac{V_m+10.66}{11.1}\right))}, & \text{else} \end{cases}$$

$$h_{inf} = \frac{1}{\left(1+exp\left(\frac{V_m+71.55}{7.43}\right)\right)^2} \qquad \beta_h^- = 0$$

$$\alpha_j^+ == \begin{cases} (-25428exp(0.2444V_m) - \frac{6.948\cdot 10^{-6}exp(-0.04391V_m))(V_m+37.78)}{(1+exp(0.311(V_m+79.23)))^{-1}}, & V_m < -40 \\ 0, & \text{else} \end{cases}$$

$$\alpha_j^- = \begin{cases} \frac{0.02424exp(-0.01052V_m)}{1+exp(-0.1378(V_m+40.14))}, & V_m < -40 \\ \frac{0.6exp(0.057V_m)}{1+exp(-0.1(V_m+32))}, & \text{else} \end{cases}$$

$$j_{inf} = \frac{1}{\left(1+exp\left(\frac{V_m+71.55}{7.43}\right)\right)^2} \qquad \beta_j^- = 0\ .$$

For the remaining f-, f_2-, f_{CaSS}-, s- and r-gates the inferior values and the time constants are given as follows

$$\begin{aligned}
\tau_f &= 1102.5exp\left(-\frac{(V_m+27)^2}{225}\right) + \frac{200}{1+exp\left(\frac{13-V_m}{10}\right)} + \frac{180}{1+exp\left(\frac{V_m+30}{10}\right)} + 20 \\
f_{inf} &= \frac{1}{1+exp\left(\frac{V_m+20}{7}\right)} \\
\tau_{f_2} &= 562exp\left(-\frac{(V_m+27)^2}{240}\right) + \frac{31}{1+exp\left(\frac{25-V_m}{10}\right)} + \frac{80}{1+exp\left(\frac{V_m+30}{10}\right)} \\
f_2^{inf} &= \frac{0.67}{1+exp\left(\frac{V_m+35}{7}\right)} + 0.33 \\
\tau_{f_{CaSS}} &= \frac{80}{1+\left(\frac{Ca_{SS}}{0.05}\right)^2} + 2 \\
f_{CaSS}^{inf} &= \frac{0.6}{1+\left(\frac{Ca_{SS}}{0.05}\right)^2} + 0.4 \\
\tau_s &= 85exp\left(-\frac{(V_m+45)^2}{320}\right) + \frac{5}{1+exp(\frac{V_m-20}{5})} + 3 \\
s_{inf} &= \frac{1}{1+exp(\frac{V_m+20}{5})} \\
\tau_r &= 9.5exp\left(-\frac{(V_m+40)^2}{1800}\right) + 0.8 \\
r_{inf} &= \frac{1}{1+exp(\frac{20-V_m}{6})}\ .
\end{aligned}$$

To complete the set of equations the differential equations for the concentrations of free inner calcium $[Ca^{2+}]_i$, the calcium in the sub-space $[Ca^{2+}]_{SS}$ and in the sarcoplasmic reticulum $[Ca^{2+}]_{SR}$ as well as the one for $\bar{R}$ are shown. $\bar{R}$ is the portion of closed channels that are related to the calcium-induced calcium release of the sarcoplasmic reticulum. In order to avoid another extensive list of parameters that need not to be detailed here, their values are directly inserted into the differential equations:

$$\begin{aligned}\frac{\partial[Ca^{2+}]_i}{\partial t} &= \frac{1}{1+\frac{2\cdot10^{-4}}{([Ca^{2+}]_i+0.001)^2}}\left(0.066691051(I_{leak}-I_{up})+I_{xfer}\right.\\ &\quad \left.-5.8443\cdot10^{-5}(I_{bca}+I_{pca}-2I_{NaCa})\right) \qquad (5.52)\\ \frac{\partial[Ca^{2+}]_{SS}}{\partial t} &= \frac{-0.017532825I_{CaL}+20.007315289I_{rel}-300I_{xfer}}{1+\frac{10^{-4}}{([Ca^{2+}]_{SS}+0.00025)^2}} \qquad (5.53)\\ \frac{\partial[Ca^{2+}]_{SR}}{\partial t} &= \frac{1}{1+\frac{10\cdot0.3}{([Ca^{2+}]_{SR}+0.3)^2}}(I_{up}-(I_{rel}+I_{leak})) \qquad (5.54)\\ \frac{\partial\bar{R}}{\partial t} &= -0.045\left(2.5-\frac{1.5}{1+\left(\frac{1.5}{[Ca^{2+}]_{SR}}\right)^2}\right)[Ca^{2+}]_{SS}\bar{R}+0.005(1-\bar{R}) \qquad (5.55)\end{aligned}$$

The subspace is the space between the SR and the cell wall. In this subspace there are so-called ryanodine receptors which sense an increase in calcium concentration that happens due to a fast calcium ion influx. Those ryanodine receptors are represented via I_{rel} and induce the calcium release from the SR which provides the major portion of calcium.

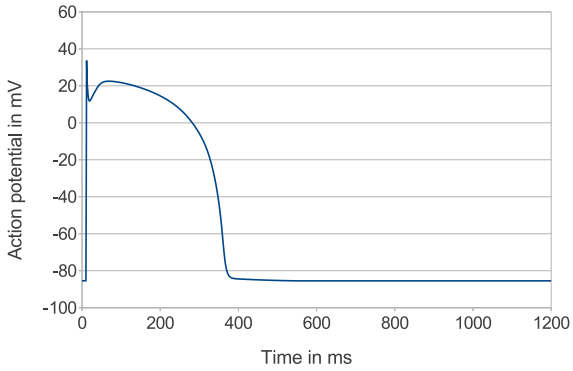

Figure 5.4: Action potential of the TT model

Figure 5.4 shows the AP that is produced by the TT model. The following important differences can directly be seen by comparing it to the AP of the McAllister model (fig. 5.3):

- There is a distinct slow depolarization phase after the quick repolarization following the hyperpolarization in the TT model which is typical for ventricular cells.

- The AP of the TT model is more bulgy which is typical for ventricular cells and atypical for nodal or Purkinje cells.
- The TT model does not show a rise of the AP during the resting state. It represents a ventricular cell thus it needs to be paced from outside by either an external stimulus or another cellular model that provides one.

5.4.3.3 Stewart The Stewart model resembles the TT model in many parts. The most important difference between those models is the introduction of a so-called *funny* current

$$I_f = I_{f,K} + I_{f,Na} \ , \tag{5.56}$$

that is responsible for the repolarization phase and serves as the pacemaker. It is driven by two sub-currents that result from potassium and sodium ion fluxes, respectively. They are governed by the membrane potential and a newly introduced gate y and read as

$$I_{f,K} = c_{f,K} y (V_m - E_K) \tag{5.57}$$

$$I_{f,Na} = c_{f,Na} y (V_m - E_{Na}) \ , \tag{5.58}$$

with conductivities $c_{f,K} = 0.0234346\, nSpF^{-1}$ and $c_{f,Na} = 0.0145654\, nSpF^{-1}$ and equilibrium potentials $E_{f,K} = -86.3596773\, mV$ and $E_{f,Na} = 74.51577033\, mV$. The y gate is defined by

$$\alpha_y^+ = exp(-2.9 - 0.04 V_m) \qquad \alpha_y^- = exp(3.6 + 0.11 V_m) \tag{5.59}$$

$$\tau_y = \frac{4000}{\alpha_y^+ + \alpha_y^-} \qquad y_{inf} = \frac{1}{1 + exp\left(\frac{V_m + 80.6}{6.8}\right)} \ . \tag{5.60}$$

Compared to the TT model there are slight changes in the r- and s-gates and in the currents to account for human Purkinje fiber cells instead of ventricular cells. Further details of this model can be found in Stewart et al. [143].

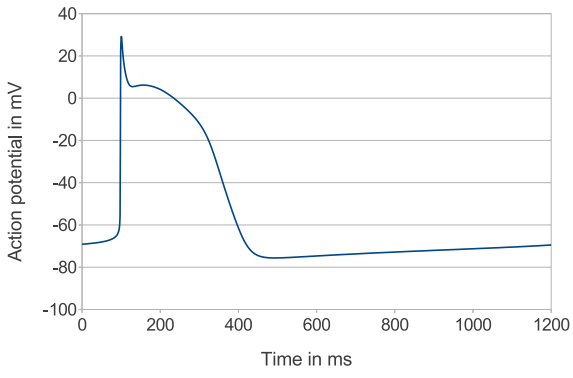

Figure 5.5: Action potential of the Stewart model

Figure 5.5 shows the AP of the Stewart model and again some differences become apparent with respect to the other two models:

- The AP shape looks like a mixture of both previous models. This is due to the fact that the Stewart model just alters the TT model and adds the funny current that provides Purkinje cell characteristics.
- The AP duration is a little bit shorter than in the McAllister model because the Stewart model is parameterized for human rather than for rodent Purkinje cells.
- The beating frequency of both, the McAllister and the Stewart model, is about $0.77\,\mathrm{s}^{-1}$.

5.4.4 Models of Contraction

In this section suitable models for the description of the active stress component in eq. (5.1) are explained and evaluated. Therein the scalar quantity $T(t, \boldsymbol{b})$ depends on the time and the left Cauchy-Green tensor $\boldsymbol{b}$. Current models that describe the active stress of cardiac muscles are formulated one-dimensionally with respect to the stretch λ in fiber direction. To the authors knowledge there is no two-dimensional model of the contractile stress. Therefore, within this thesis, $T(t, \boldsymbol{b})$ is simplified to $T(t, \lambda_1) = T(t, \lambda_2) = T(t, \lambda)$, such that the principal stretches λ_1 and λ_2 are assumed to be equal. This assumption is valid because the circular specimen to be studied is in an equibiaxial strain state. Moreover the specimen is isotropic (cf. sec. 6.1), thus principal stretches are taken for the 'fiber stretches'.

$T(t, \lambda)$ implicitly depends on $[Ca^{2+}]_i$. In the original publications that present the following models, a time course of $[Ca^{2+}]_i$ is usually prescribed. As in this work the calcium concentration in the cytoplasm is determined by a model of cell electrophysiology, $[Ca^{2+}]_i$ is the interface between the models of cell electrophysiology and of mechanical stress development.

5.4.4.1 Hunter-McCulloch-ter Keurs The Hunter-McCulloch-ter Keurs model (HMT) proposed in Hunter et al. [78] was the first choice because of its relative simplicity. In its original version all model parameters have been taken from animal testing. The application to human cardiac cells is questionable but as experimental data for humans were and are quite rare this model is still one of the best choices. An improved version of this model including some model parameters that then have been derived from human cardiac cells is given in the next paragraph.

The HMT model assumes the active stress to be determined by

$$T(t, \lambda, [Ca^{2+}]_i) = T_{ref}(1 + \beta_0(\lambda - 1))z(t, \lambda, [Ca^{2+}]_i), \tag{5.61}$$

with β_0 being a measure of how cooperatively neighboring myofilaments interact, the reference tension of a cell T_{ref} and z being an activation variable. If there is no interaction of neighboring myofilaments, $\beta_0 = 1$ and the length-dependent tension development would result from the changing myofilament overlap only.

The activation variable z represents the tropomyosin kinetics that result from the binding of $[Ca^{2+}]_i$ to troponin C (TnC). With $0 \leq z \leq 1$ it equals the portion of available actin

sites. The system of ordinary differential equations to describe the activation state of the cardiac muscle is given as

$$\frac{\partial z}{\partial t} = \alpha_0 \left(\left(\frac{[Ca^{2+}]_b}{[Ca^{2+}]_b^{50}} \right)^n (1-z) - z \right) \tag{5.62}$$

$$\frac{\partial Ca_b}{\partial t} = \rho_0 [Ca^{2+}]_i ([Ca^{2+}]_b^{max} - [Ca^{2+}]_b) - \rho_1 \left(1 - \frac{T_{cb}}{\gamma T_{ref}} \right) [Ca^{2+}]_b \,, \tag{5.63}$$

with the concentration of bound calcium Ca_b, the half maximal calcium concentration

$$[Ca^{2+}]_i^{50} = 10^{6-(p[Ca^{2+}]_i^{50ref}(1+\beta_2(\lambda-1)))} \tag{5.64}$$

and the Hill coefficient

$$n = n_{ref}(1 + \beta_1(\lambda - 1)) \,. \tag{5.65}$$

An active crossbridge binding ($T_{cb} > 0$) slows down the unbinding and it can even stop the unbinding when, at maximum, $T_{cb} = \gamma T_{ref}$. Due to a very little influence and to reduce the model complexity, crossbridge binding is neglected here, thus one chooses $T_{cb} = 0$.

The time course of $[Ca^{2+}]_i$ is given by the electrophysiological model. A summary and description of the model parameters as well as their values is given in table 5.1. More details about this model and explanations where the experimental data have been taken from is given in Hunter et al. [78].

Table 5.1: Parameters of the original HMT model

Parameter	Value	Interpretation
ρ_0	0.1 $\mu M^{-1} ms^{-1}$	binding rate TnC-Ca^{2+}
ρ_1	0.163 ms^{-1}	unbinding rate TnC-Ca^{2+}
γ	2.6	effect of tension on ρ_1
$[Ca^{2+}]_b^{max}$	2.26 μM	saturation $[Ca^{2+}]_b$
α_0	0.002 ms^{-1}	activation and inactivation rate (actin sites)
n_{ref}	6.9	reference Hill coefficient for cooperativity of actin sites
$p[Ca^{2+}]_i^{50ref}$	6.2	exponential reference half-maximal $[Ca^{2+}]_i$
T_{ref}	100 kPa	tension at resting SL
β_0	1.45	tension-length dependency of T
β_1	1.95	tension-length dependency of n
β_2	0.31	tension-length dependency of $[Ca^{2+}]_b^{50}$

It has to be emphasized that the reference tension of a cell, $T_{ref} = 100kPa$ in table 5.1 does not have any relevance as in this thesis it is determined by a parameter fitting. The fitted value might be differently interpreted as a reference tension of the overall tissue and therefore it is four to five orders of magnitude lower.

5.4.4.2 Niederer et al. The Niederer-Hunter-Smith model (NHS) can be found in Niederer et al. [117]. It improves the HMT model by adding more details and by fitting some of the parameters to human cardiac cells. One major difference between the two models is the introduction of the parameter z_{max} that represents the maximum

portion of available actin binding sites. It is incorporated because it is assumed that even at full activation not all actin sites are available. The muscle tension then reads as

$$T = T_{ref}(1 + \beta_0(\lambda - 1))\frac{z}{z_{max}} \; . \tag{5.66}$$

The differential equation describing the concentration of bound calcium again is eq. (5.63) but z is now determined by

$$\frac{\partial z}{\partial t} = \alpha_0 \left(\frac{[Ca^{2+}]_b}{[Ca^{2+}]_b^{50}} \right)^n (1 - z) - \alpha_{r1} z - \alpha_{r2} \frac{z^{n_r}}{z^{n_r} + K_Z^{n_r}} \; , \tag{5.67}$$

thus binding as well as slow and fast unbinding processes of calcium to and from TnC are separated. The algebraic equations to compute the maximum portion of available actin sites and the half-maximal concentrations of bound and free inner calcium, respectively, are

$$z_{max} = \frac{\frac{\alpha_0 \left([Ca^{2+}]_b^{max} \right)^n}{\left([Ca^{2+}]_b^{50} \right)^n} - K_2}{\alpha_{r1} + K_1 + \frac{\alpha_0 \left([Ca^{2+}]_b^{max} \right)^n}{\left([Ca^{2+}]_b^{50} \right)^n}} \tag{5.68}$$

$$K_1 = \frac{\alpha_{r2} z_p^{n_r - 1} n_r K_Z^{n_r}}{\left(z_p^{n_r} + K_Z^{n_r} \right)^2} \tag{5.69}$$

$$K_2 = \alpha_{r2} \frac{z_p^{n_r}}{z_p^{n_r} + K_Z^{n_r}} \left(1 - \frac{n_r K_Z^{n_r}}{z_p^{n_r} + K_Z^{n_r}} \right) \tag{5.70}$$

$$[Ca^{2+}]_b^{50} = [Ca^{2+}]_b^{max} \frac{[Ca^{2+}]_i^{50}}{[Ca^{2+}]_i^{50} + \frac{\rho_1^{ref}}{\rho_0} \left(1 - \frac{0.5(1 + \beta_0(\lambda - 1))}{\gamma} \right)} \tag{5.71}$$

$$[Ca^{2+}]_i^{50} = [Ca^{2+}]_i^{50ref} (1 + \beta_1(\lambda - 1)) \; . \tag{5.72}$$

The original parameter values are given in table 5.2. Again, T_{ref} will be replaced by an experimentally determined value. In Niederer and Smith [116] and Weise and Panfilov [156] this model has been used to simulate human cardiac tissue. Therein the myocyte relaxation rates $\alpha_{r1} = 0.01 s^{-1}$ and $\alpha_{r2} = 0.025 s^{-1}$ are modified in order to achieve a faster relaxation. Also $T_{ref} = 125 kPa$ and $p[Ca^{2+}]_i^{50ref} = 6.5$ have been adopted.

The cross-bridge binding kinetics, i.e. the history-dependent relaxation that has been proposed in the NHS model have been implemented as well but as this does not affect the results too much, it is not detailed here but can be found in Niederer et al. [117].

5.4.5 Excitation-Contraction Coupling

The presented HMT and NHS models require the time course of free intra-cellular calcium as input. In its original version the MNT model does not provide a differential equation for $[Ca^{2+}]_i$ thus the coupling differential equation (5.48) needs to be implemented.

Table 5.2: Parameters of the original NHS model

Parameter	Value	Interpretation
ρ_0	0.1 $\mu M^{-1} ms^{-1}$	binding rate TnC-Ca^{2+}
ρ_1	0.2 ms^{-1}	reference unbinding rate TnC-Ca^{2+}
γ	2	effect of tension on ρ_1
$[Ca^{2+}]_b^{max}$	70 μM	saturation $[Ca^{2+}]_b$
α_0	0.008 ms^{-1}	activation rate (actin sites)
α_{r1}	0.002 ms^{-1}	slow relaxation rate (actin sites)
α_{r2}	0.00175 ms^{-1}	fast relaxation rate (actin sites)
n	3	Hill coefficient for cooperativity of actin sites
K_Z	0.15	fitted relaxation parameter (actin sites)
n_r	3	fitted relaxation parameter (actin sites)
z_p	0.85	point of Taylor expansion for z
β_1	-4	SL dependency of $[Ca^{2+}]_i^{50}$
$[Ca^{2+}]_i^{50ref}$	1.05 μM	reference half-maximal $[Ca^{2+}]_i$
T_{ref}	56.2 kPa	tension at resting SL
β_0	4.9	tension-length dependency of T

The combined HMT-MNT model has one major drawback. The ion current I_{si} comprises multiple cellular processes like the sodium-calcium exchanger and the calcium induced calcium release of the sarcoplasmic reticulum, the latter of which is known to deliver the largest portion of calcium. Thus the calcium dynamics which are most important for the development of contractile force are not represented in sufficient detail. Especially in the modeling of drug action those dynamics need to be represented in more detail because drugs act very specifically on certain gates and processes.

Thus in the second step the MNT model has been replaced by the TT model that fulfills the named requirement. This model is then coupled to the NHS model. *Coupling* just means combining all the differential equations of both models into one system.

The TT model is a model for ventricular cells that provides more detailed calcium dynamics such that the differential equation (5.48) is replaced by multiple differential equations describing the free inner calcium concentration, the calcium concentration in the sarcoplasmic reticulum and in the sub-space. As it is a model of ventricular cells, this model is not self-contractile and needs to be paced from outside by a prescribed stimulus. For the simulation of autonomously beating tissue the Stewart model has been chosen as a pacemaker, although it is a Purkinje fiber cell model, because it is one of the rare human models, and because it is as complex as the TT model. A similar complexity of both models is necessary to allow for comparable drug application in both models. In the simulations, the stimulus that is autonomously created by the Stewart model is directly applied to the TT model for $1ms$.

As an extension of this thesis the human sinoatrial models of Seemann et al. [137] and Chandler et al. [23] are studied in Frotscher et al. [56] in terms of their applicability to the herein investigated cardiac tissue construct. Therein they re-

place the Stewart model. Both models are modified versions of the atrial model in Courtemanche et al. [33].

5.5 Remarks on Viscoelasticity

Both, the ECM and the cells, in reality behave viscoelastically. The time-dependent behavior of both has been investigated and modeled in Abney [1] and Zahalak et al. [161]. This chapter closes with some remarks on the viscoelastic behavior of cardiac tissues.

Regarding stress only, viscoelasticity means that under constant strain the tissue relaxes with a certain time rate until it reaches a certain stress level. In the experiments, the drugs are applied to the tissue at constant strain but at that time the strain was held constant for a long time already thus there should be only neglectable viscoelastic effects. If there would be some, one could observe it in the experiments. As this observation is negative the viscoelastic effect of the ECM is disregarded in the model.

At the cellular level strong viscoelastic effects occur thus after a contraction it is not only the decay in calcium concentration inside the cell that recovers the resting state but also viscoelastic effects in the sliding filaments. Especially in cells without automaticity this effect is quite strong. The half-relaxation time has been measured to be approximately 0.7s, which is in the range of physiological heart beats. Nevertheless this effect is disregarded in the herein presented finite element model because firstly this would further complicate this comprehensive model. Secondly, additional experiments would be required for the determination of the viscoelastic parameters that could not be conducted during the thesis.

6 Experimental Setup

The main purposes of the developed model and its parts are the interpretation of mechanical and electrophysiological experiments as well as, in a future perspective, their partial replacement by validated models. The main focus lies on the simulation of cardiac tissues and the respective drug treatment.

For the development of the whole model and its validation, experimental data are of high importance. Experiments to determine the mechanical properties of cardiac cells, like their passive stress-strain behavior, the orientation of fibers and the influence of the stretch of sarcomeres to the active stress have been conducted in different works, e.g. Yamada [159], Guccione et al. [65], Trzewik et al. [152], Trzewik [151], Grosberg et al. [64], Nawroth et al. [111] and Agarwal et al. [2]. Also different ways to determine the electrical properties of cardiac cells and tissues exist. In patch clamp experiments one measures the action potential of the cellular membrane or the electrical properties of a single ion channel. Using multi-electrode arrays (MEAs) one can measure the cell action potential and the speed of the electrical propagation through a tissue. Recent approaches are heading to combine mechanical and electrical measurements using the concept of stretchable MEAs like in Pakazad et al. [123], Pakazad et al. [124] and Pakazad et al. [125].

In summary there is a vast amount of measurements of forces and stresses, membrane potential, electrical propagation, drug action on ion channels, conductivity of single ion channels, ion concentrations, etc. for different cell types of different species. Studying the literature reveals that those data often are very difficult to compare due to the different experimental setups, the biological and mechanical environment of the cells, the way of cell cultivation, the age and the maturity of the cells. Thus literature data varies significantly and should be verified by own experiments if possible. An important collection of electrophysiological data of cardiac cells can be found in Niederer et al. [117].

The experimental setup which is explained in the next section delivers some mechanical data that, in conjunction with electrophysiological data from the literature, serves as input for the model.

6.1 CellDrum

Since its invention in 2001 there have been a number of publications concerning the experimental device called CellDrum^{TM}, e.g. Linder et al. [93], Trzewik et al. [152] and Trzewik [151]. It is basically an inflation test of a circular, $4\mu m$ thin silicone membrane with a diameter of $1.6cm = 16000\mu m$. On top of the membrane hiPSC-CM are cultivated in a collagen monolayer of about $4\mu m$ thickness that is chemically attached. The cells are produced by *Axiogenesis AG* in Cologne, Germany who is a project partner. A regularly refreshed culture medium keeps the cells alive and as in the real heart the tissue is autonomously beating. This results from the fact that in the Cor.4U® cell line approximately 10% of the cells are nodal cells. The nodal cells have a repolarization phase thus no external stimulus is needed for cell contraction. A total number of $2 \cdot 10^5$ cells is

equally distributed in the tissue.

This composite material is clamped in a fixed ring like the one shown in fig. 6.1. The CellDrum^{TM} then can be placed into an inflation setup, named *Tissue Tension Analyzer*, as depicted in fig. 6.2. The inflation setup generates a pressure and therefor inflates the composite tissue. The corresponding deflection is measured using a laser triangulation sensor in the membrane chamber resulting in a nonlinear pressure-deflection curve as shown in the same figure.

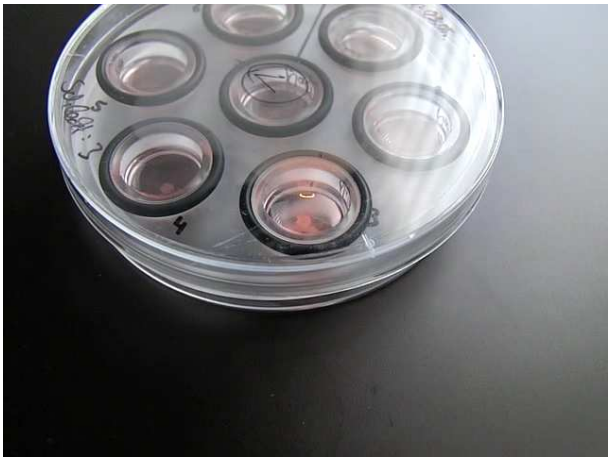

Figure 6.1: Seven CellDrums

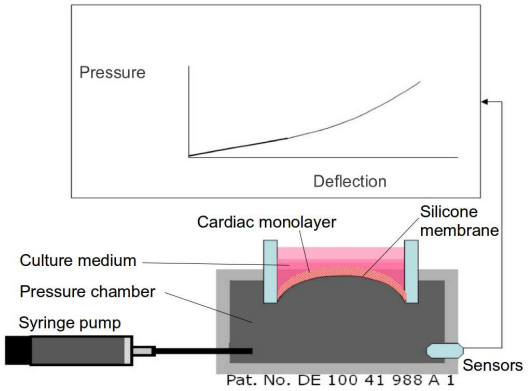

Figure 6.2: Schematic drawing of the inflation experiment

Currently the investigations are limited to so-called 2D or monolayered tissue with an approximate thickness of around 4 μm although in general the experimental setup allows for 3D tissue with a thickness of hundreds of microns. In a three-dimensional tissue the cells can distribute better and they are less restricted in their shape which both leads to a more realistic imitation of native cardiac tissue. Making the CellDrum available for 3D tissues is ongoing research that focuses on a sufficiently strong attachment of the tissue to the membrane.

Due to the circular shape of the tissue the myocytes do not align in a common preferred direction as can be seen in fig. 6.3. That gives rise to the assumption that the tissue is statistically isotropic and the global state is equibiaxial.

Figure 6.4 shows the deflection of the composite in time at constant pressure. In this case the cells are beating with a frequency of approximately $1Hz$ and during contraction they change the deflection of the composite by approximately $37\mu m$. Depending on the medication that is applied to the tissue, the amplitude will be different and the beating frequency might change because the action potential of the cells differs from the normal situation. A detailed discussion of the experimental and simulation results will follow in sect. 8.

The total thickness of a monolayer composite is $8\mu m$. The silicone membranes are accurately produced with a thickness of $4\mu m$. Before the cultivation each silicone membrane is tested by putting $500\mu l$ on top of the membrane and checking whether its resulting deflection is about $1.22mm$. Additionally the average monolayer thickness can be deter-

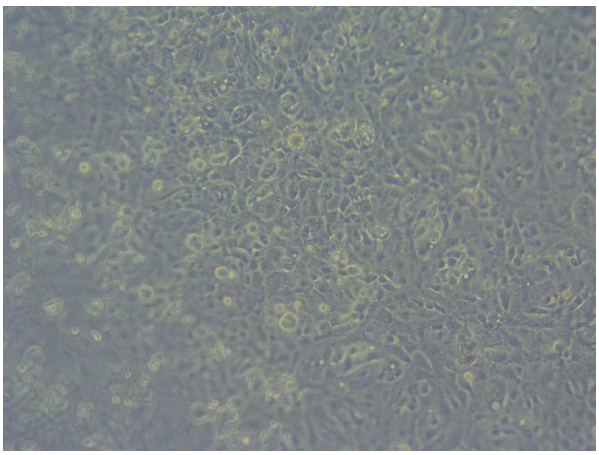

Figure 6.3: 1 mm × 1 mm microscopic cutout of the tissue showing isotropy

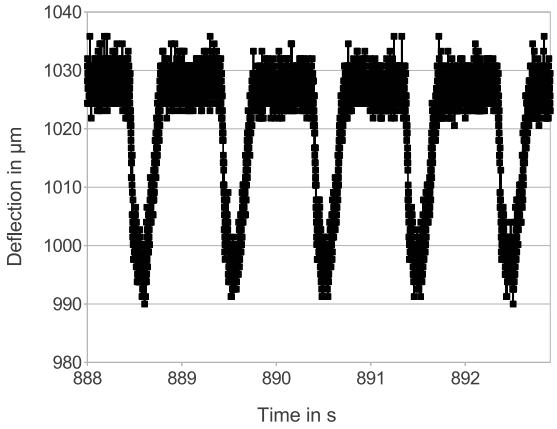

Figure 6.4: Cyclic deflection due to contraction (incl. noise)

mined using a laser scanning microscope (LSM) and has been found to be $4\mu m$ for the cell monolayers investigated here. The monolayer thickness can also be computed from the tissue volume that is known. However, the monolayer thickness can only be an average value because of the heterogeneity of the tissue and differences in cell shape. In Quintão Júnior et al. [127] 718 ventricular CM have been measured and the average cell length and width were approximately $160\mu m$ and $21.7\mu m$, respectively. Given a cross-sectional area of CM of about $191\mu m^2$ reported in Bersell et al. [10] the normal cell height is approximately $8.8\mu m$. These dimensions already show that the cell shape in a native environment strongly differs from the one in a cardiac monolayer if therein the cells have a height of approximately $4\mu m$ only. As the cells are considerably deformed in the monolayer, its thickness is very heterogeneous.

The CellDrum is intended to be used for the determination of passive and active mechanical stresses in cardiac and other tissue and for the investigation of drug treatment as reported in Gossmann et al. [63].

6.2 Discussion and Critique

In the remainder of this section the experimental setup is discussed in order to clarify its capabilities.

The CellDrum delivers purely mechanical information. Employing the herein described finite element model it is possible to evaluate the experimental results on ion channel level, i.e. computationally it is possible to determine the electrophysiology of the cells in the tissue.

As the tissue layer is chemically attached to the silicone membrane this influences the behavior of the cardiac monolayer in two ways. Firstly, the passive material properties of the composite of course depend on the silicone membrane. In the case that the passive stress of the cardiac tissue is of interest, one could perform inflation experiments with

the membrane only and with a composite that is chemically prevented from beating, respectively. An additive and volume-weighted split into passive tissue and membrane stresses leads to the accurate passive stress of the cardiac tissue. Secondly, the cells form adhesions not only to neighboring cells and to the ECM but also to the silicone membrane which not only changes the cell morphology but also its contractile behavior. Currently there is no way to quantify how the silicone membrane influences the tissue behavior. Qualitatively one can say that cells form more and stronger adhesions to a stiff substrate than to a soft substrate. Consequently the silicone substrate is constructed as soft and thin as possible in order to have a little influence on the contractile behavior of the cells. Having in mind that the next goal is the cultivation of 3D tissue on the silicone membranes the importance of these limitations will decrease.

The general applicability to 3D tissue has already been mentioned. Investigating 3D tissue is very important because it is known that cells behave differently in a monolayer and in a 3D tissue. In fact, currently there are difficulties concerning a strong attachment of the 3D tissue, i.e. during experiments a 3D tissue would detach from the silicone membrane due to a comparably weak fibronectin binding between the tissue and the membrane. The investigation of 3D tissue in the CellDrum is part of an ongoing PhD thesis.

As it is apparent from fig. 6.3, the tissue is globally isotropic. The different regions of the human heart show anisotropy and of course anisotropic tissue again behaves different from an isotropic tissue equivalent. One major work could be to change the circular membrane to a different shape such that an anisotropy can evolve.

Currently the *Tissue Tension Analyzer* is very expensive because a laser triangulation sensor is utilized for the measurement of the membrane deflection. Within a Master thesis (Bayer [8]) and a PhD thesis in progress (Bayer [7]) a new capacitive *Tissue Tension Analyzer* is under construction. This approach decreases the costs for a single setup by a factor of 100.

As will be seen in the results section, both the beating frequency and the beating force greatly vary with respect to different cell cultures. The reasons for that are manifold and interconnected as an enforced change in the beating frequency of a cardiac cell induces a change in the beating force too because the free inner calcium concentration is altered within some seconds after the frequency change. Therefore it is currently impossible to even try to exactly reproduce the experimental data. Consequently, in the investigation of the drug action one needs to focus on qualitative observations.

7 Modeling of Cardiac Tissue Constructs

In general the models and model parts that have been described in chap. 5 are applicable to 2D, 3D and plate problems. Due to the central experimental setup, the CellDrum, the focus in this work lies on plate problems. The length-thickness ratio of the tissue composite exceeds 2000 and therefore any attempt to model the CellDrum with 3D volume elements would lead to huge computational costs because the need of an unreasonably large number of finite elements.

Due to isotropy and symmetry of the problem only a quarter of the CellDrum is modeled. Rotational symmetry is not used because noncircular membranes and anisotropic tissues should not be excluded in later studies. Appropriate symmetry boundary conditions are applied as depicted in fig. 7.1. The geometry is usually discretized with a relatively large number of triangular plate elements. The fineness of the discretization is mainly due to the extremely large deflection of the CellDrum which is in the range of 1.2–3 mm. The simulations are performed in a physically and geometrically nonlinear framework inside the FE software *Code_Aster* of the French power utility EDF. The computationally demanding problem requires a large number of time steps in order to achieve convergence in the Newton-Raphson algorithm.

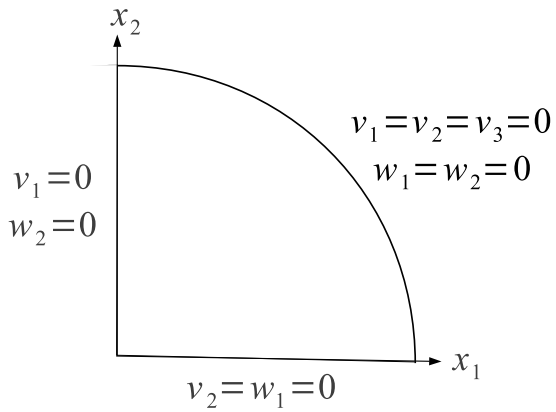

Figure 7.1: Symmetry and clamping boundary conditions for the quarter CellDrum model

7.1 Choosing Appropriate Finite Elements

The choice of appropriate plate finite elements is problem dependent. They need to be highly performant in the case of large displacements and to handle incompressible material. Both possible choices, the smoothed plate finite element described in sect. 3.4 and the *Code_Aster* shell element called COQUE_3D (engl.: 3D shell), are capable of solving this problem. The ES-FEM plate element needs a finer discretization as it uses 3-noded triangular elements only, compared to the COQUE_3D element that employs a hybrid approach. 7-noded triangular serendipity elements are used for the interpolation of the

rotational degrees of freedom and 6-noded triangular Lagrange elements are used for the translational degrees of freedom. The performance of those two elements obviously is quite different as they use interpolation functions of different degree and as the COQUE_3D elements employ a corotational framework. For the current problems, that are supposed to often show below 5% or at most 10% strain, both elements produce nearly equal results. The ES-FEM plate element is expected to perform better if the geometry becomes more complex and if the strains become larger because it is comparably insensitive to element distortion that is likely to occur in those cases.

7.2 Parameter Fitting

Currently we model the passive material response with the Neo-Hookean material. Its strain energy function Ψ in terms of the principal stretches $\boldsymbol{\lambda} = (\lambda_1, \lambda_2, \lambda_3)^T$ reads as

$$\Psi(\lambda_1, \lambda_2, \lambda_3) = C_{10}(\lambda_1^2 + \lambda_2^2 + \lambda_3^2 - 3) \; , \tag{7.1}$$

with its material constant C_{10} that defines the slope of the nonlinear stress-strain curve. Taking into account the active component of the constitutive law one can specialize eq. (5.1) using eq. (5.61) to

$$S^{11} = 2C_{10} - p\frac{1}{\lambda_1^2} + T_{ref}(1 + \beta_0(\lambda_1 - 1))\frac{1}{\lambda_1^2} \; , \tag{7.2}$$

at maximum activation $z = 1$. Of course eq. (5.61) of the HMT model can be replaced by the NHS version, eq. (5.66). The main mechanical parameters in this model are the Neo-Hookean material constant C_{10} and the tissue tension at rest T_{ref}, both determined by a parameter fitting. To this end we minimize

$$2C_{10} + \frac{1}{\lambda_1^2}(1 + \beta_0(\lambda_1 - 1))T_{ref} - p\frac{1}{\lambda_1^2} - S_e \rightarrow Min \; , \tag{7.3}$$

with respect to C_{10} and T_{ref} with the stress S_e obtained from the experiments. The experimental stress values can be determined by simple geometric considerations that are illustrated in fig. 7.2. It is obvious that for the circular isotropic membrane the stretch is equibiaxial and

$$\lambda_1 = \lambda_2 = \lambda = \frac{d_2}{d_1} \tag{7.4}$$

holds with d_1 being the initial diameter of the membrane and d_2 the arc length in the deflected state. $\lambda_3 = \lambda^{-2}$ can be obtained from the incompressibility condition $J = 1$ that has been introduced in eqs. (7.2) and (7.3). The arc length can be computed from the center deflection u_3 via

$$d_2 = \frac{arctan\left(\frac{2u_3}{d_1}\right)(4u_3^2 + d_1^2)}{2u_3} \; . \tag{7.5}$$

An expression for the experimentally determined 2^{nd} Piola-Kirchhoff stress can been derived like for instance in Schomburg [136]. The balance of the pressure-induced vertical

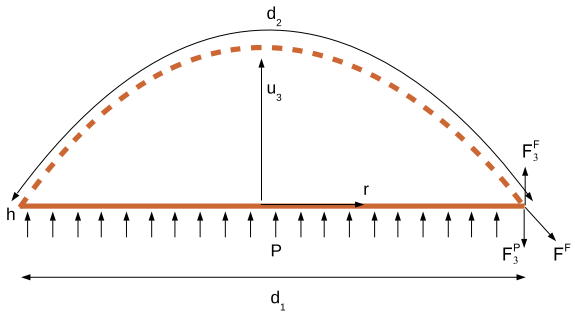

Figure 7.2: Illustration of the deflected CellDrum

force F_3^P and the vertical component F_3^F of the force that is acting on the clamping frame as shown in fig. 7.2 reads as $F_3^P = F_3^F$. Replacing F_3^P by the pressure acting on the circular membrane and representing F_3^F by the membrane (experimental) stress S_e acting on the whole circumference of the frame and on the membrane thickness h, the balance of vertical forces is given by

$$F_3^P = P\pi \left(\frac{d_2}{2}\right)^2 = F_3^F = S^e h \cdot 2\pi \frac{d_2}{2} \left.\frac{dw}{dr}\right|_{r=\frac{d_2}{2}} . \tag{7.6}$$

The derivative of the deflection w in radial direction is included in order to get the vertical portion of F^F. Given the approximation that the inflated membrane has a parabolic shape, its deflection w can be represented by

$$w(r) = u_3 \left(1 - \frac{4r^2}{d_2^2}\right) . \tag{7.7}$$

Carrying out the differentiation in eq. (7.6) leads to

$$P\pi \left(\frac{d_2}{2}\right)^2 = S^e h \cdot 2\pi \frac{d_2}{2} u_3 \frac{4}{d_2} \tag{7.8}$$

and reorganizing delivers the experimentally determined 2^{nd} Piola-Kirchhoff stress

$$S_e = \frac{P\left(\frac{d_2}{2}\right)^2}{4hu_3} . \tag{7.9}$$

As usual in soft tissue biomechanics the poisson ratio ν is assumed to be close to 0.5.

With respect to the described parameter fitting the data for the membrane-tissue composite yields $C_{10} = 0.0838284$ and $T_{ref} = 0.058kPa$. A parameter fitting for measurements of the silicone membrane alone revealed $C_{10} = 0.1840321$. Thus, in the small strain regime the membrane is approximately twice as stiff as the composite which proves that it influences the contractility of the cardiac cells as discussed in sect. 6.2. This influence even grows when large strains occur which is not the case for the results presented here, though.

Another limitation of the parameter fitting is the assumption of a homogeneous and isotropic stretch although the local stretch of course depends on the tissue composition, a local anisotropy and the activation state. In the fitting procedure these local differences are disregarded and the average stretch λ is used instead. The assumption of global isotropy has been verified in sect. 6.1.

Finally it should be mentioned that fig. 7.2 implies that the membrane inflates like a freely supported plate and is shaped like a sphere segment. From fig. 7.1 it is apparent that the membrane is actually fully clamped and consequently the model in eq. (7.9) is only an approximation.

7.3 Constitutive Tensor

In order to compute the stiffness matrices the constitutive tensor is needed. The stress can be split up into three parts and so can the constitutive tensor

$$\mathbb{C} = \mathbb{C}_{dev} + \mathbb{C}_{vol} + \mathbb{C}_a \ . \tag{7.10}$$

The deviatoric and volumetric parts of the constitutive tensor need not be derived here as they represent the passive response of the material that is not in the focus of this thesis. Those derivations can be found in Holzapfel [72]. It is still necessary to derive $\mathbb{C}_a$

$$\mathbb{C}_a = 2\frac{\partial \boldsymbol{S}_a}{\partial \boldsymbol{C}} = 2\frac{\partial \boldsymbol{S}_a}{\partial \lambda} \otimes \frac{\partial \lambda}{\partial \boldsymbol{C}} \ , \tag{7.11}$$

the part of the constitutive tensor that arises from the cellular contraction. With

$$\lambda^2 = \boldsymbol{a}_0 \cdot \boldsymbol{C}\boldsymbol{a}_0 = \boldsymbol{C} \cdot (\boldsymbol{a}_0 \otimes \boldsymbol{a}_0) \tag{7.12}$$

the derivative of the stretch with respect to the right Cauchy-Green tensor can be computed as follows

$$\begin{aligned}
\frac{\partial \lambda}{\partial \boldsymbol{C}} &= \frac{1}{2}(\boldsymbol{C} \cdot (\boldsymbol{a}_0 \otimes \boldsymbol{a}_0))^{-\frac{1}{2}} \frac{\partial (\boldsymbol{C} \cdot (\boldsymbol{a}_0 \otimes \boldsymbol{a}_0))}{\partial \boldsymbol{C}} \\
&= \frac{1}{2}(\boldsymbol{a}_0 \cdot \boldsymbol{C}\boldsymbol{a}_0)^{-\frac{1}{2}} \frac{\partial (\boldsymbol{a}_0 \cdot \boldsymbol{C}\boldsymbol{a}_0)}{\partial \boldsymbol{C}} \\
&= \frac{1}{2}\lambda^{-1} \frac{\partial \boldsymbol{C}}{\partial \boldsymbol{C}} \cdot (\boldsymbol{a}_0 \otimes \boldsymbol{a}_0) \\
&= \frac{1}{2}\lambda^{-1} (\boldsymbol{a}_0 \otimes \boldsymbol{a}_0) \ .
\end{aligned} \tag{7.13}$$

In terms of the herein investigated circular membrane one can ideally assume that $\lambda_1 = \lambda_2 = \lambda$ and $\lambda_3 = 1$. Using the spectral decomposition of $\boldsymbol{C}$,

$$\boldsymbol{C} = \sum_{i=1}^{3} \lambda_i^2 \boldsymbol{a}_i \otimes \boldsymbol{a}_i, \tag{7.14}$$

leads to

$$\boldsymbol{C} = \lambda^2(\boldsymbol{a}_1 \otimes \boldsymbol{a}_1 + \boldsymbol{a}_2 \otimes \boldsymbol{a}_2) = \lambda^2 \boldsymbol{R} \tag{7.15}$$

$$\boldsymbol{C}^{-1} = \lambda^{-2}\boldsymbol{R}^T = \lambda^{-2}\boldsymbol{R}. \tag{7.16}$$

with $\boldsymbol{R}$ orthogonal and symmetric. The derivative of the active part of the 2^{nd} Piola-Kirchhoff stress tensor with respect to the stretch then reads as

$$\begin{aligned}
\frac{\partial \boldsymbol{S}_a}{\partial \lambda} &= \frac{\partial (T(t,\lambda)\lambda^{-2}\boldsymbol{R})}{\partial \lambda} \\
&= \left(\frac{\partial T(t,\lambda)}{\partial \lambda}\lambda^{-2} - 2\lambda^{-3}T(t,\lambda)\right)\boldsymbol{R} \\
&= \left(T_{ref}\beta_0 z\lambda^{-2} - 2\lambda^{-3}T_{ref}(1+\beta_0(\lambda-1))z\right)\boldsymbol{R} \\
&= T_{ref}z\left(\beta_0\lambda^{-2} - 2\lambda^{-3} - 2\lambda^{-2}\beta_0 + 2\lambda^{-3}\beta_0\right)\boldsymbol{R} \\
&= T_{ref}z\lambda^{-2}(2\lambda^{-1}(\beta_0 - 1) - \beta_0)\boldsymbol{R}\,.
\end{aligned} \tag{7.17}$$

In the given isotropic application, $\boldsymbol{R} = \boldsymbol{I}$ and one arrives at

$$\mathbb{C}_a = 2\frac{\partial \boldsymbol{S}_a}{\partial \lambda} \otimes \frac{\partial \lambda}{\partial \boldsymbol{C}} \tag{7.18}$$

$$= \lambda^{-3}T_{ref}z(2\lambda^{-1}(\beta_0 - 1) - \beta_0)\boldsymbol{I} \otimes \boldsymbol{I}\,. \tag{7.19}$$

7.4 Model Summary

In order to facilitate the understanding of this multi-component model, fig. 7.3 depicts the basic steps. Inflation experiments and drug testing are performed in the Lab of Medical and Molecular Biology at Aachen University of Applied Sciences. These data can be used to construct the model and to fit the mechanical model parameters.

The two systems of ordinary differential equations are solved at each time step at the level of the constitutive equations. The models of cellular processes are parameterized solely using electrophysiological literature data. The nodal model provides the stimulus for the ventricular model, thereby being the pacemaker.

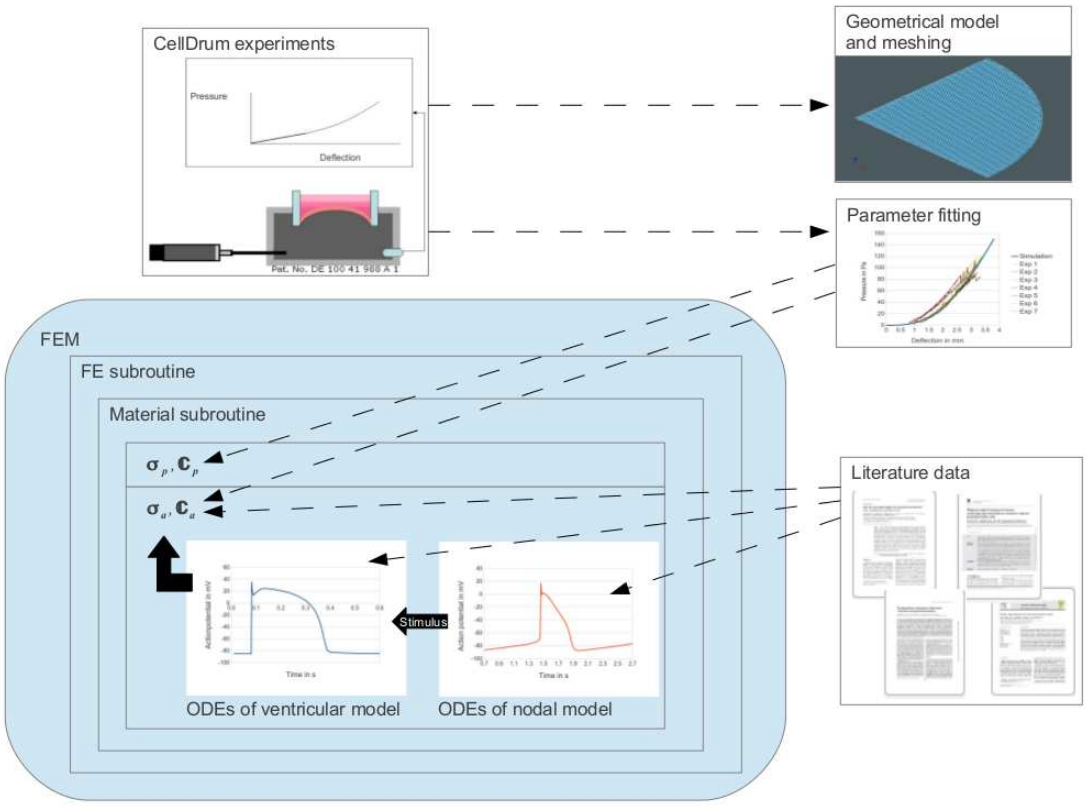

Figure 7.3: Model summary

8 Implementation, Validation and Numerical Results

8.1 Implementations

8.1.1 Data Acquisition and Processing

The data acquisition from the CellDrum is implemented in LabView and further analytics of the results is made through MS Excel or its non-commercial equivalent Libre Office Calc. The parameter fittings have been implemented in the software Scilab and statistical analysis of the pressure-deflection curves has been implemented in the statistics software R.

8.1.2 Finite Element Framework

As already indicated, the FE software in use is *Code_Aster* which is developed by the French utility EDF. It is an open source software whose core is written in FORTRAN77 until version 11.x. Most of the implementations have been done in *Code_Aster* version 10.6 and have been successfully tested in version 11.4 too. Starting from version 12.0 the core of *Code_Aster* is written in FORTRAN90 and the material subroutines written in this thesis have been successfully converted to FORTRAN90 and tested in *Code_Aster* version 12.1. The administrative and configuration files as well as the user interfaces of *Code_Aster* are written in Python.

The pre- and post-processor that has been employed is called SALOME and also comes from EDF. Geometry creation and modification, meshing and graphical analysis of the results can all be done in this software.

In order to prepare a simulation using *Code_Aster* one needs to define a so-called command file. In this Python interpreted command file the mesh can be read in and modified, the material definitions are made, the boundary conditions are established, the solver can be chosen and configured and the results can be processed to prepare post-processing.

8.1.2.1 ES-FEM For the implementation of the plate smoothed FEM the so-called discrete Kirchhoff triangular (DKT) element of *Code_Aster* has been modified. The implementation of the DKT element provides all the structures that are required in order to be able to implement the plate ES-FE. The DKT element is a three-noded triangular plate element with three translational and three rotational degrees of freedom at each node. The only change to the element definition that has to be made is an increase of the bandwidth of the stiffness matrix because edge-based smoothing domains generally span over two elements. The computation of the strain-displacement matrix and the stiffness matrix is made on element level by replacing the standard computation of the DKT element.

Besides some work-around implementations to fit into the complex framework of *Code_Aster* the whole implementational work is limited to the element subroutine. It is ongoing work to properly integrate the implementation into the *Code_Aster* distribution making it available to the community.

8.1.2.2 Material Model The passive-active model for cardiac tissue is implemented on the level of the constitutive equation. The standard hyper-elastic material model is used and the active part is additionally implemented. Within those subroutines the systems of ordinary differential equations are implemented that describe the cellular electrophysiology of different cell types. Depending on the given problem the ventricular cell model can either be solved on each Gaussian point or only once. The nodal cell model is always solved only once per time step as it has no influence to the beating force but only serves as a pacemaker for the ventricular cells.

Some configuration files have been written in order to let the *Code_Aster* distribution know the material model.

The nonlinear equation systems are solved using a Newton-Raphson algorithm with a relative error of $e_{rel} = 10^{-6}$ at discrete times t_i. At each Gaussian point the stiff system of ODEs is solved with an adaptive time stepping scheme in the way that the Newton-Raphson time interval $[t_i, t_{i+1}]$ is further divided into m time steps because the electrical processes are much faster than the mechanical response. A fourth order singly-diagonal implicit Runge-Kutta solver with adaptive time stepping (Hairer and Wanner [67]) which has been shown to be unconditionally A-stable is used for the solution of the system of ODEs.

8.2 Validation of S-FEM Implementation

Firstly the ES-FEM implementation for plate problems is validated for some academic plane stress and plain strain problems that already have been presented in Frotscher and Staat [50]. They show the abilities of the ES-FEM in general and the application to geometrically and materially nonlinear plates. Secondly the ES-FEM implementation is applied to the CellDrum problem and performs well despite the extreme slenderness of the membrane.

8.2.1 Square Plate with Circular Hole

The first problem to be examined is a linear plane strain problem shown in fig. 8.1. It illustrates a quarter of a square plate of size $10m \times 10m$ with a circular hole of $1m$ radius and the applied symmetry and traction boundary conditions. Its thickness is $t = 1m$. The material has been chosen with $E = 1000N/m^2$ and $\nu = 0.3$. The problem domain has been discretized with three-noded triangular elements as can be seen in fig. 8.2.

Figures 8.3 and 8.4 show the displacements u_1 and u_2 on the symmetry lines $x_2 = 0$ and $x_1 = 0$, respectively. The ES-FEM results achieved with linear triangular elements (ES-FEM-T3) are compared with the results achieved with standard FEM using triangular elements (FEM-T3, i.e. constant strain) and quadrilateral elements (FEM-Q4). The latter serves as the reference solution. It is obvious that the ES-FEM-T3 solution is nearly equal to the FEM-Q4 solution whereas FEM-T3 shows deficiencies. Especially with $x_1 \to 1$ and $x_2 \to 1$, i.e. next to the hole, the FEM-T3 solution differs significantly from the two other solutions.

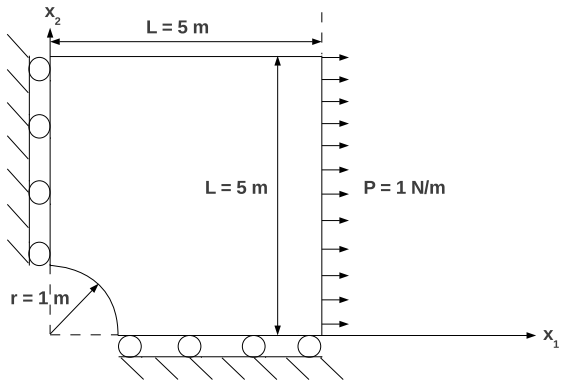

Figure 8.1: Geometry and boundary conditions of plate with hole

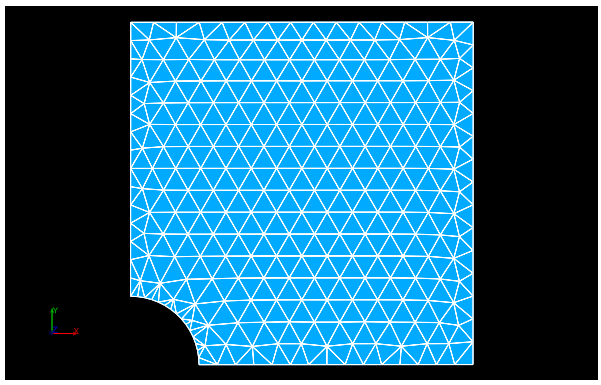

Figure 8.2: Discretization with triangular elements

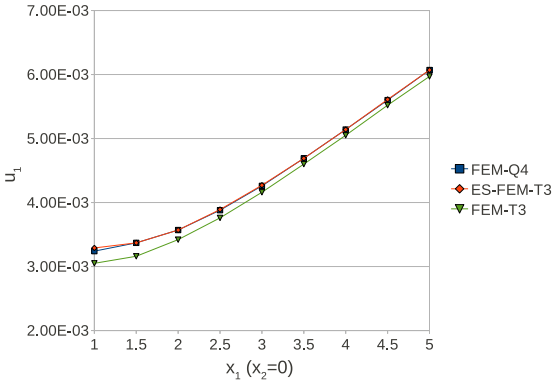

Figure 8.3: Displacement u_1 of the bottom symmetry line of the plate with a hole

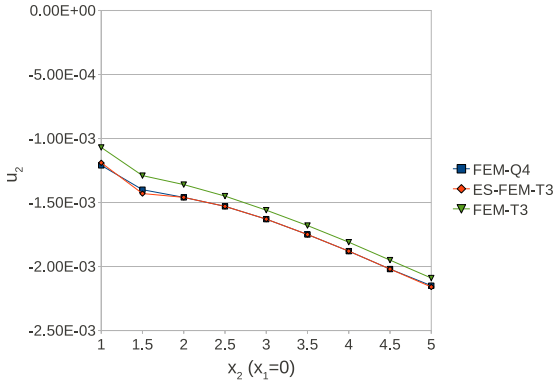

Figure 8.4: Displacement u_2 of the left symmetry line of the plate with a hole

Here, the T3 and Q4 meshes were built on a similar number and a similar set of nodes. It can be observed that if both meshes are built on the same set of nodes the ES-FEM-T3 solution is as good as the FEM-Q4 solution. To use the same set of nodes is a very difficult task in practical applications but the more general observation that ES-FEM-T3 and FEM-Q4 perform similarly for meshes of similar complexity is remarkable. Especially in biomechanics the investigated structures often have a quite complex and irregular geometry thus an automatic discretization with quadrilaterals usually fails. Being able to use a method that allows the usage of T3 elements (or T4 for 3D problems) without loss of accuracy is very beneficial.

8.2.2 L-shaped 2D Solid

Now, neo-Hookean material is applied to the plane stress problem shown in fig. 8.5 using $C_{10} = 2MPa$ and $\nu = 0.4999999$ to represent soft incompressible material. Figure 8.6 shows the very good accuracy of ES-FEM-T3. Comparing the strains in tension direction at the traction line, i.e. at $x_1 = -25mm$, the ES-FEM-T3 results are nearly equal to the

FEM-Q4 results whereas FEM-T3 again shows deficiencies. Especially in the vicinity of $(x_1, x_2) = (-25, 50)mm$ FEM-T3 becomes inaccurate.

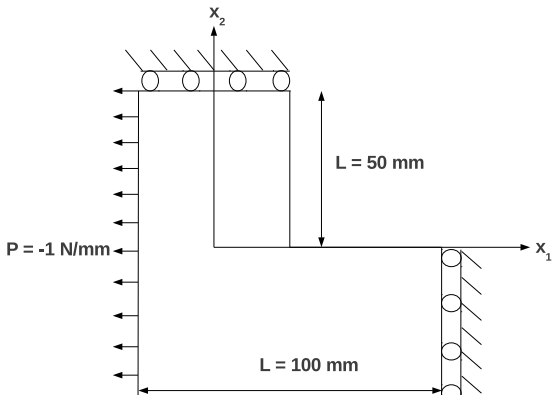

Figure 8.5: L-Shaped solid with boundary conditions

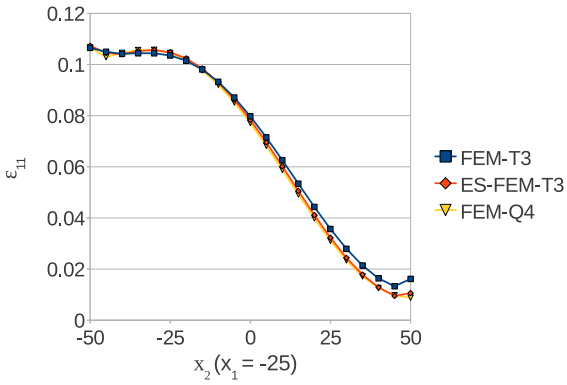

Figure 8.6: Strain in 1-direction at traction line

In table 8.1 the tangential strains on the horizontal middle line of the solid, i.e. at $x_2 = 0$, are compared. Having in mind that a singularity appears at the reentrant corner at $x_1 = 25$, one can observe that the normal strains in direction x_1 produced by ES-FEM-T3 are closer to those produced by FEM-Q4 than those produced by FEM-T3. This is a result of the strain smoothing and shows the main benefit of ES-FEM.

Table 8.1: ε_{11} at horizontal middle line

x_1	FEM-T3	FEM-Q4	ES-FEM-T3
-25	0.07974	0.07716	0.07838
-20	0.07994	0.0803	0.07925
-15	0.08729	0.08789	0.08763
-10	0.09705	0.09795	0.09772
-5	0.10899	0.11023	0.11018
0	0.12289	0.12459	0.12478
5	0.13854	0.14095	0.14157
10	0.15569	0.15932	0.16051
15	0.17445	0.18097	0.18268
20	0.20137	0.21098	0.20469
25	0.26564	0.38176	0.28432

Those first two examples of course are academic test cases but they already show that ES-FEM-T3 is superior to FEM-T3 and that the results are more accurate. One more very important property of S-FEM for the application in biomechanics is their insensitivity to element distortion that is illustrated in the following section.

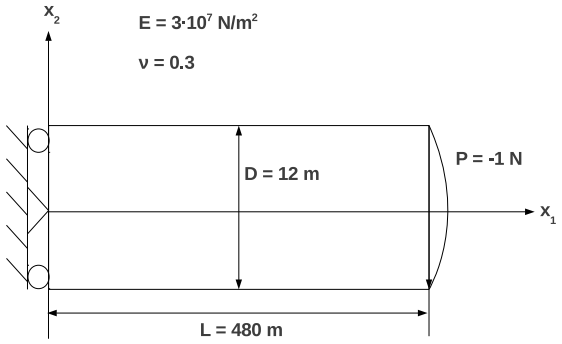

Figure 8.7: Cantilever beam with boundary conditions (drawing is not true to scale)

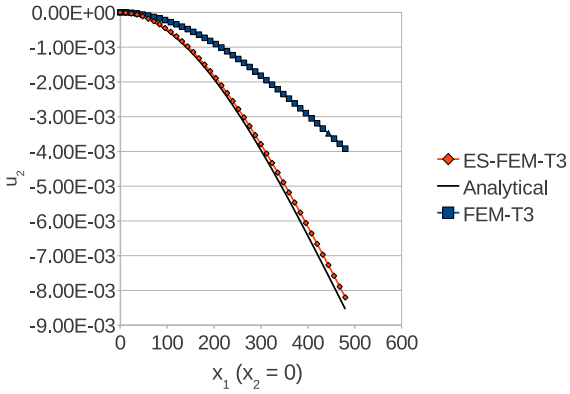

Figure 8.8: Displacement u_2 of the beam line discretized with distorted T3 elements

8.2.3 Cantilever Beam

Within this thesis the applications mainly are thin plates and shells consisting of soft biological material that possibly undergo large deformations. These problems lead to largely distorted meshes that are difficult to handle using standard FEM because shear locking occurs. To show the strong abilities of ES-FEM it is applied to the long cantilever beam shown in fig. 8.7 (Liu et al. [97]). The cantilever beam has a length-thickness ratio of 40 and is loaded with $P = -1N$ such that the parabolic shear distribution

$$\sigma_{12} = -\frac{P}{I}\left(\frac{D^2}{4} - x_1^2\right) \tag{8.1}$$

is achieved at the free end with the moment of inertia

$$I = \frac{D^3}{12}\,. \tag{8.2}$$

It is discretized with distorted triangular elements with an aspect ratio of 6.11. As one can see in fig. 8.8, FEM-T3 has a very poor performance whereas ES-FEM-T3 is very close to the exact solution. This demonstrates that ES-FEM-T3 naturally overcomes the shear locking problem. Its ability to compute problems discretized with a largely distorted mesh with high accuracy is especially very beneficial when it comes to large deformation. These problems often are solved incorporating remeshing procedures that are not necessary with ES-FEM. The locking is reduced due to the fact that the matrix bandwidth is increased by employing smoothing domains and thus the strain approximation is better. Element distortion has a minor influence in S-FEM in general because no derivatives occur in the finite element formulation for the computation of the strain-displacement matrix and because the isoparametric mapping can be avoided. The Gaussian integration is performed on the boundary of each smoothing domain in the physical coordinate system.

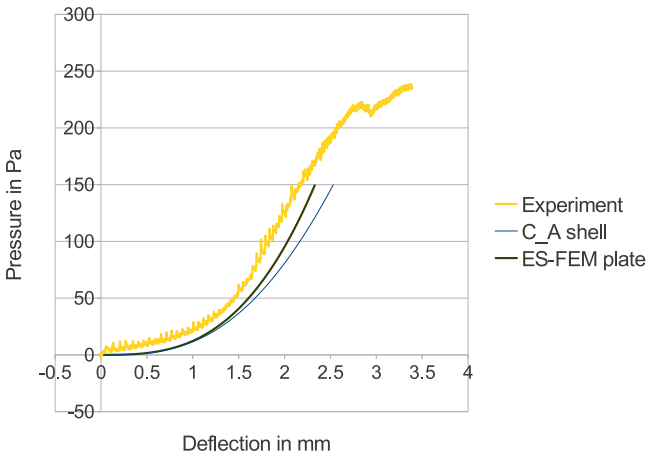

Figure 8.9: 4 μm thick membrane seeded with 100 μm thick tissue

8.3 Simulation of Cardiac Monolayers

The CellDrum setup described in sect. 6 up to now has been used for the investigation of cardiac monolayers that have a thickness of about $4\mu m$. As the current plate ES-FEM implementation does not incorporate a handling of large rotations, like for instance the corotational approach, it converges very slowly when the deflection of the membrane becomes very large. Thus for the current application we usually employ the *Code_Aster* shell element named COQUE_3D that has been mentioned in sect. 7.1 already. One drawback of those elements are stress oscillations close to regions where Dirichlet boundary conditions are applied. Those oscillations do not appear for the ES-FEM-T3 elements.

As already indicated, both elements produce similar results and this is shown in fig. 8.9. For large rotations the ES-FEM-T3 element shows a much worse convergence behaviour concerning the Newton iterations (although it always converges). ES-FEM-T3 is the element of choice for so-called three-dimensional tissue layers with a thickness of about $100\mu m$. For 3D tissue layers the CellDrum problem is still a plate problem with a diameter to thickness ratio of 160.

Based on the implementations that have been done in this thesis, materially and geometrically nonlinear FS-FEM-T4 elements have been implemented in another PhD thesis (Duong [42]). As FS-FEM is the 3D equivalent of ES-FEM those tetrahedral elements have very similar properties. Those elements can be employed when - apart from the investigation of the CellDrum experiments - 3D tissue simulations need to be performed.

Due to isotropy and symmetry the model only represents a quarter of the CellDrum and the applied appropriate boundary conditions are depicted in fig. 7.1. The fineness of the discretization mainly depends on the slenderness and the expected deflection of the CellDrum. It has a diameter of 16 mm and in the case of a cell monolayer it has a thickness of only $0.008mm$. Therefore we have to deal with radius-thickness ratios of about 1000 and a maximum deflection of the membrane in the range of 2.5–$3mm$. This computationally

demanding situation requires a large number of time steps. The maximum pressure is $150Pa$ and it is applied with an initial step size of $1.5 \cdot 10^{-4}Pa$ that adaptively increases to a step size of $2.7Pa$ that is then constant in the range of $15Pa$ to $150Pa$.

All experimental data that is shown in this section has been measured in the course of a PhD thesis (Gossmann [62]) and serves as a unique data set for model validation.

8.3.1 Simulation of Pressure-deflection Curves

Firstly the model is validated by simulating the experimental pressure-deflection curves. The contraction of the cells produces an active stiffness contribution that reduces the deflection of the membrane as observed in fig. 6.4. This change in deflection Δu_3^c due to contraction is in the range of 10–$40\mu m$ and therefore is much smaller than the usual deflections of 1–$2mm$ at which the membrane is investigated. Consequently in those simulations the electrophysiological cell processes are not computed but maximum activation of the cells is assumed (i.e. $z = 1$). Figure 8.10 shows seven experimental pressure-deflection curves of $4\mu m$ thick silicone membranes with a $4\mu m$ thick monolayer of cultivated cardiac tissue. Those curves are employed for the parameter fitting and with the resulting parameters the shown pressure-deflection curve can be simulated that perfectly fits the experimental results.

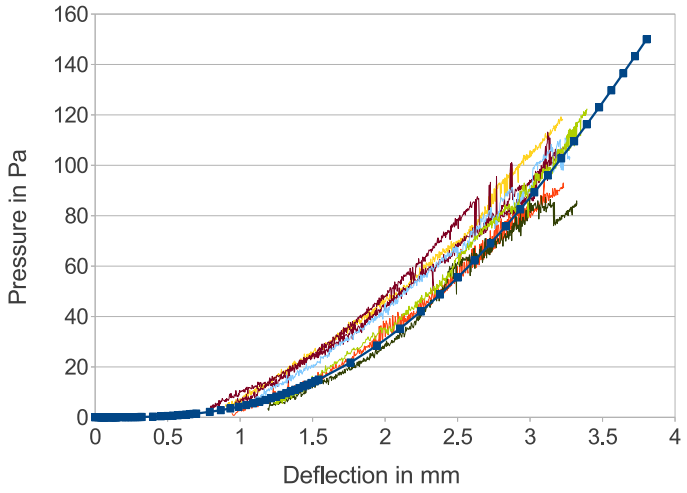

Figure 8.10: Comparison of seven experimental and simulation (*continuous line with markers*) results

The accurate simulation of the passive reaction of the tissue strongly depends on a good estimation of C_{10} and parameter fittings should be repeated regularly. This is especially true if the amount of fibroblasts, the ratio of fibroblasts to CM, the thickness of the cardiac tissue or of the silicone membrane change. Not only by construction but also due to remodeling processes in the lifetime of an engineered cardiac tissue the ratio of fibroblasts to CM changes. Consequently, besides drug testing, it is necessary to regularly

repeat the plain inflation experiments in order to be able to properly parameterize the models. On the other hand the computational model can be improved by incorporating the amount of fibroblasts directly as discussed in sect. 9.2.5.

8.3.2 Simulation of Cell Contraction

To simulate single or multiple contractions one can start the contraction process at a certain point of the simulation result in fig. 8.10. This starting point can be chosen depending on the experimental results as follows.

From the experiments one is able to extract the deflection of the membrane when the cells are inactivated. For clarity fig. 8.11 shows an experimental result that has a deflection at rest of $1.23mm$ and compares it to a simulation result. Even with an equal pressure a different membrane will have a different deflection at rest in the order of approximately $0.05mm$ because it is not possible to accurately reproduce the biological tissues. To provide a good accuracy of the simulations one can select a time step of the pressure-deflection simulation in sect. 8.3.1 at which the membrane has a deflection that is close to the one shown in the experiments. If that does not provide sufficient accuracy one can simulate up to a pressure such that the proper deflection at rest is achieved in the simulation. It can be seen in fig. 8.10 that it is generally possible to simulate any membrane deflection in the experimental range.

Starting from this resting state when the cells are inactive. One can now simulate one or multiple contractions using all parts of the model, i.e. computing the electrophysiological processes on cell level and use the resulting free inner calcium concentration as an input to the mechanical part of the constitutive model at time t_i. The time steps $\Delta t_i = t_{i+1} - t_i$ need to be chosen in the way so that the mechanical response of the model is sufficiently accurate. The electrophysiological processes are much faster and therefore are computed in adaptively subdivided time steps.

Figure 8.11 compares one contraction of the CellDrum with two simulation results. It is obvious that the change in deflection is nearly the same in all the cases. Thus the contractility of the cells can be captured very well by the model.

One also observes that the duration of the deflection, i.e. the contraction time is much shorter in the simulation where the MNT Purkinje fiber model has been used in conjunction with the HMT model ($0.2s$ vs. $0.6s$). This effect leads to the assumption that the mechanical response of the applied model is too fast. Possible reasons have been identified that explain the discrepancy:

- Depending on the specific cell type the speed of development of free intra-cellular calcium concentration is different. As the literature data provides a wide range of results the parameter set of the system of ODEs might have to be adjusted according to the respective cell type. Currently there are a lot of uncertainties concerning the actual cell types that are represented in the monolayer, their degree of maturity, the cell environment and literature data is often very specific and does not fully fit.
- The time rate of muscle activation $\dot{z}$ (cf. eq. (5.67)) depends on the free intra-

cellular calcium concentration. Again, it might be the rate constants that need to be adjusted to the cell type.

- It has been mentioned in Ruiz-Baier et al. [132] that today's models directly use cellular models on tissue level without properly scaling or averaging the cellular contributions to the passive or active stress in the tissue with respect to cell volume portion or cell distribution. Necessarily, the mechanical reaction of the tissue on the electrophysiological processes is much more direct than it would be with a so-called homogenization that is discussed in sect. 9.2.7.

- The current model assumes that all the cells in the monolayer contract synchronously. In reality the action potential is transmitted through the monolayer via gap junctions that connect neighboring cells to each other. This again would lead to a slower mechanical response.

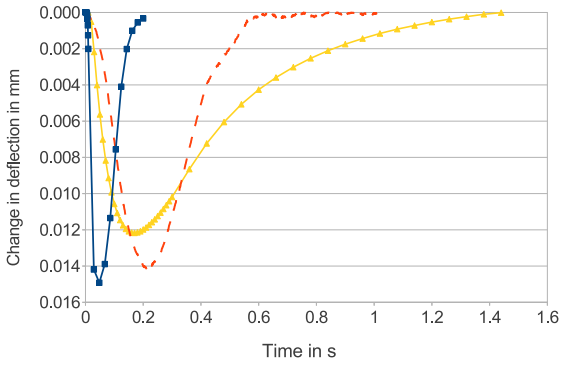

Figure 8.11: Comparison of MNT-HMT (*blue continuous line with square markers*) and TT-NHS (*yellow continuous line with triangular markers*) simulations with experimental results (*red dashed line*) with respect to Δu_3^c

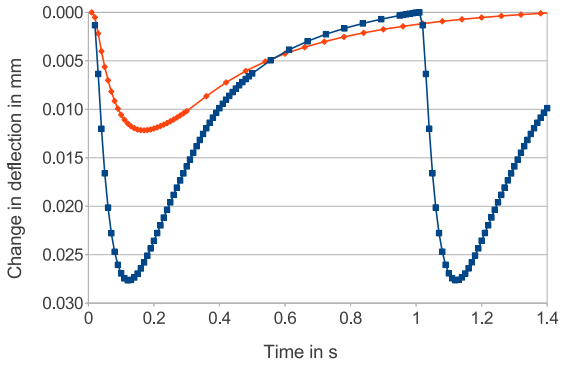

Figure 8.12: Comparison of simulations paced with a current density of $52pA \cdot pF^{-1}$ at $1Hz$ (*blue continuous line with square markers*) and $0.7Hz$ (*red continuous line with diamond markers*) with respect to Δu_3^c

The second simulation curve has been computed using the TT human ventricular model in conjunction with the NHS excitation-contraction coupling. It can clearly be seen that the duration of the contraction, i.e. the shape of the curve agrees much better with the experimental findings. This is more due to the changes made in the NHS model with respect to the HMT model as explained in sect. 5.4.4.2 rather than due to the different electrophysiological model that is employed. Especially the splitting of the tropomyosin relaxation into slow and fast terms is supposed to drive those differences.

It has to be mentioned that there even seems to be a quantitative agreement between the curves in fig. 8.11. The question that arises is whether this is generally true and it can only

be answered partially by this thesis as the amount of available experimental data is quite low. However, the following results indicate that a quantitative agreement is achieved. In the following section some experimental results are shown for drug action on the CellDrum tissue and in the experimental results one recognizes strong differences in the beating frequencies of the control groups. It has already been mentioned that a so-called *staircase* effect exists that stands for positive relation between beating frequency and contractile force, i.e. if the beating frequency increases, the contractile force increases too and vice versa. In fig. 8.12 the TT model has been paced externally at two different frequencies and after a $60s$ pre-equilibration phase the contractile force is considerably different between the two simulations. The pre-equilibration phase is necessary because the model needs some time to adjust to the new beating frequency just like real cells. Accounting for the staircase effect indeed gives a fairly good quantitative agreement between the experimental and simulated change in deflection as can be seen from table 8.2.

Table 8.2: Comparison of experimental ($m = 3$) and simulated maximum change in deflection at different beating frequencies in mm

	f $= 0.5Hz$	f $= 1.0Hz$
Experiment	0.00913	0.02735
Simulation	0.00462	0.02764

Nevertheless, respecting the given data, it currently is not possible to reliably compare effects quantitatively. Therefore the following results are partially normalized to facilitate the interpretation of the results. However, the results are not normalized in some diagrams if quantitative differences are important to be shown.

8.3.3 Drug Action

This section shows simulation results for the drugs named in sect. 4.4 and discusses them by comparison to CellDrum results and to findings from literature. Most of the results have already been published in Frotscher et al. [53; 54].

The results need to be regarded with respect to the fact that, although a lot of electrophysiological experiments have been performed all over the world for measuring the action potential of single cells, the action potential conduction through cell clusters, individual currents as well as intra- and extracellular ion concentrations, the gathered information varies. The experimental data strongly depend on the cell type, their maturity, the production batch, the investigated species, the experimental setup, the environment of the cells and many more. Therefore the data differ in the reported beating force, cell stresses, beating frequency, action potential shifts and IC_{50} values. The data are selected such that it fits the CellDrum experimental setup the most but often even this very carefully selected information varies quite much. In some cases reliable data could not be found for human induced pluripotent stem cells. Thus data from different cells need to be taken. Even under relatively well-controlled and well-known conditions the mechanical CellDrum results themselves vary for the named reasons. Currently there are only few setups that measure mechanical parameters like the CellDrum, e.g. Grosberg et al. [64],

Nawroth et al. [111], Agarwal et al. [2] and Pakazad et al. [125] but so far they have not been regarded for comparison because of the aforementioned uncertainties.

In the following all the results are collected comparing experimental and simulation results of drug action on cardiac monolayers. If not stated otherwise, the inotropic and chronotropic drug effects have been simulated with the TT-NHS model and the Stewart model, respectively. For each respective drug the employed data for modeling the drug action, as described in sect. 5.4.2, are summarized in a table including the source where it has been obtained from.

8.3.3.1 Lidocaine Figures 8.13 and 8.14 show the simulated influence of Lidocaine to the change in deflection of the membrane and to the beating frequency of the cells at different concentrations and corresponding experimental results obtained from CellDrum experiments. According to table 8.3 an IC_{50} value of 50 μM is applied to both, the activation gate of the fast sodium channel and the activation gate of the pacemaker current.

Table 8.3: IC_{50} values for Lidocaine

IC_{50}	Ion channel	Species and cell type	Reference
11.2 μM	Nav1.5	HiPSc-derived cardiomyocytes	Sirenko et al. [140]
70 μM	Nav1.5	HiPSc-derived cardiomyocytes	Terasawa [148]
20 μM	Sodium	Mouse eSc-derived cardiomyocytes	Stoelzle et al. [144]
61 μM	Sodium	Freshly isolated rat cardiac myocytes	Hill et al. [70]
20–70 μM	HCN	Xenopus laevis Oocytes	Meng et al. [105]

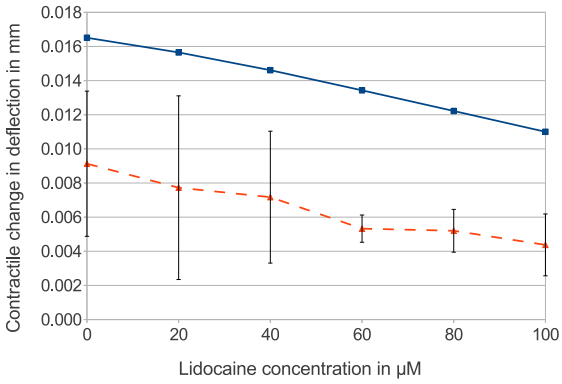

Figure 8.13: Lidocaine affecting contractibility in experiment (*dashed*) and simulation (*continuous*); sample size $m = 3$

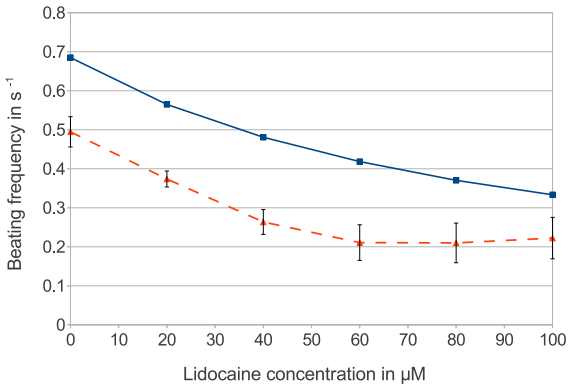

Figure 8.14: Lidocaine affecting beating frequency in experiment (*dashed*) and simulation (*continuous*); sample size $m = 3$

Clearly both, the simulated dose-dependent change in beating force and in heart rate, are in good agreement with the experimental results. Within the range of 0–100 μM of applied Lidocaine, the beating force seems to be linearly dose-dependent. The model even captures

the nonlinear slope of the experimental curve for the influence of Lidocaine on the beating frequency shown in fig. 8.14. Although, qualitatively, the simulation results show a good agreement with the experiments, the untreated cells (0 μM of Lidocaine) show half of the change in deflection of the membrane and half of the beating frequency the cells have had in standard pressure-deflection experiments. The multiply addressed force-frequency relationship (FFR) or *staircase* effect leads to the expectation that if the model beating frequency is reduced to the experimental beating frequency, the beating force and thus the change in deflection reduces as well. The influence of the FFR has been investigated within a master thesis (Koch [84]) and the results are published in Frotscher et al. [56]. Computational results on the FFR can be found in there and are repeated here only exemplarily. The FFR is still under investigation because the mechanism how to adopt the model remains unclear. Unfortunately, intentionally prescribing or altering the beating frequency of a cellular model that has been parameterized for a different frequency (here: 1 Hz) does not reflect the unknown underlying differences in the cell electrophysiology. In the master thesis we showed that an external pacing which results in an adjustment of the change in deflection according to the staircase effect, potentially alters the model response to drug treatment. In fig. 8.15 one can observe a saturation effect for high Lidocaine concentrations if the model is externally paced at the experimentally determined frequencies given in fig. 8.14. The saturation results from the fact that the observed beating frequency of the model is approximately halved by the external pacemaking. Consequently, the negative effect on the beating force is huge and the effect of a treatment with Lidocaine will clearly be different, even qualitatively.

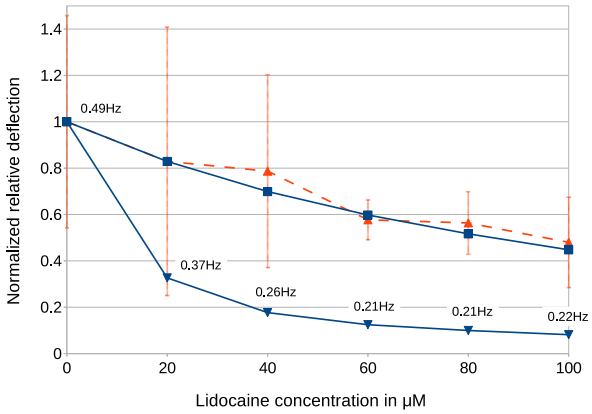

Figure 8.15: Effect of external pacing on model response to Lidocaine application. Beating frequencies taken from fig. 8.14 (*triangular markers*); the other curves are the normalized versions of those in fig. 8.13

As a result we gain the understanding that the differences in the experimentally observable beating frequencies need to be accounted for in a more sophisticated way. Most probably they result from differences in ion channel expression depending on for instance maturity, cell production batch or donor. Modeling such influences is very challenging but can be approached with increasing amount, level of detail and quality of experimental data. Related recent approaches and ideas are discussed in the final chapter of this work.

8.3.3.2 Verapamil To appropriately model Verapamil we take $IC_{50} = 40\mu M$ to modify the activation gate of the fast inward sodium channel, according to table 8.4. The secondary inward channel of the model is, amongst others, responsible for calcium influx during the plateau phase. Its activation is modified by $IC_{50} = 0.1\mu M$. Lastly the activation of the delayed rectifier potassium current needs to be modified by $IC_{50} = 0.14\mu M$.

The simulation and experimental results are shown in figs. 8.16 and 8.17. The

Table 8.4: IC_{50} values for Verapamil

IC_{50}	Ion channel	Species and cell type	Reference
$40\mu M$	Nav1.5	HiPSC derived cardiomyocytes	Kramer et al. [87]
$0.14\mu M$	hERG	HiPSC derived cardiomyocytes	Kramer et al. [87]
$0.19\mu M$	hERG	Human embryonic kidney cells	Liang et al. [92]
$0.1\mu M$	Cav1.2	HiPSC derived cardiomyocytes	Kramer et al. [87]
$0.25\mu M$	Cav1.2	Wistar rat isolated ventr. myoc.	Zahradníková et al. [162]

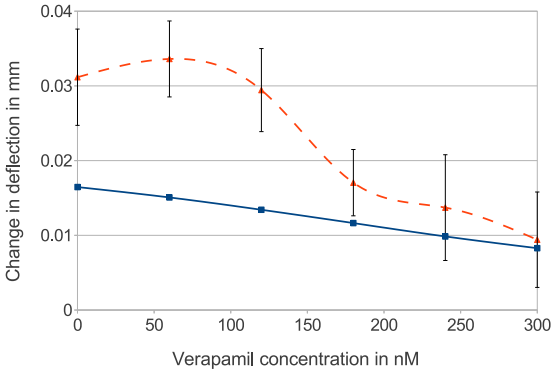

Figure 8.16: Verapamil affecting contractibility in experiment (*dashed*) and simulation (*continuous*); sample size $m = 3$

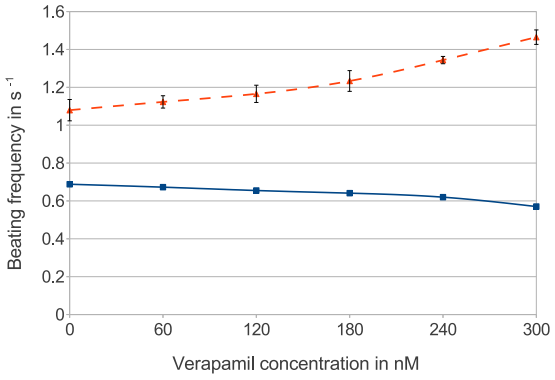

Figure 8.17: Verapamil affecting beating frequency in experiment (*dashed*) and simulation (*continuous*); sample size $m = 3$

experimental results show concentration-dependent negative inotropic and positive chronotropic effects. The negative inotropic effect of Verapamil confirms recent findings Mehta et al. [104], Rosen [130], Yokoo et al. [160] and the increase in contractibility for very low concentrations of Verapamil has also been observed in Mehta et al. [104] leading to the suspicion that Verapamil affects further ion channels or that non-investigated actions take place. Despite this effect the model appropriately reproduces the negative inotropic effect.

Comparing fig. 8.18 with fig. 8.16 reveals that a replacement of the MNT model with the TT model directly yields a much different model response to Verapamil. From the experimental data shown in both figures it is merely impossible to tell which of the two is more correct, especially in conjunction with the mentioned uncertainties.

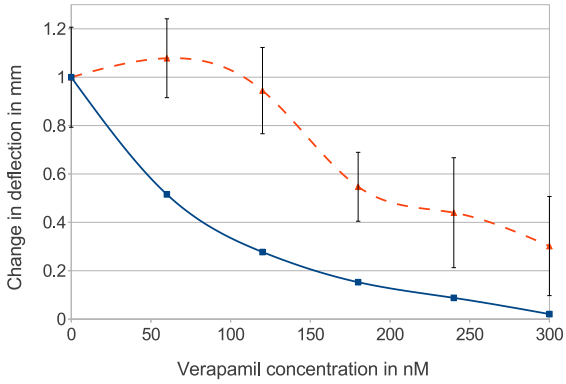

Figure 8.18: Different effect of Verapamil when using the TT-NHS model (*square markers*)

The positive chronotropic effect of Verapamil, i.e. the increase in beating frequency, obtained in CellDrum experiments (monolayer), is contradictory to recent findings on stem-cell derived cardiomyocyte clusters (hiPSC-EBs and hESC-EBs), cf. Yokoo et al. [160], Mehta et al. [104] and Sirenko et al. [140]. The simulation shows a negative chronotropic effect that qualitatively fits the experimental findings for monolayers in the literature (Guo et al. [66] and Harris et al. [68]), although the increasing nonlinearity for Verapamil concentrations above 180 nM cannot be verified due to a lack of data.

8.3.3.3 Veratridine Veratridine is entirely accounted for effecting fast sodium channels and its half maximal inhibitory concentration for modeling the inhibition of the fast sodium inactivation is $IC_{50} = 0.4\mu M$, according to table 8.5. The increased calcium influx due to a reversal mode of the sodium-calcium-exchanger is considered by the inhibition of the opening transition rate of the slow inward inactivation gate by $IC_{50} = 1.2\mu M$.

Table 8.5: IC_{50} values for Veratridine

IC_{50}	Ion channel	Species and cell type	Reference
$7.7\mu M$	Sodium	Human embryonic kidney cells	Felix et al. [47]
$0.4\mu M$	Sodium	Guinea pig purkinje fibers	Honerjäger and Reiter [74]

The simulations for Veratridine show dose-dependent positive inotropic and negative chronotropic effects, as shown in figs. 8.19 and 8.20, respectively. The simulation results fit the expectations that arise from the description of the drug effects in sect. 4.4.3: an increased calcium concentration leads to a higher beating force and the prolonged action potential reduces the beating frequency.

In the simulation result in fig. 8.19 there seems to be some saturation effect as the change in deflection stays nearly constant for Veratridine concentrations larger than 0.5 μM. This observation is misleading as in fact it can be explained by inappropriate parametrizations of eq. (5.48) and the Hunter model. The point of reference for the maximum inner calcium

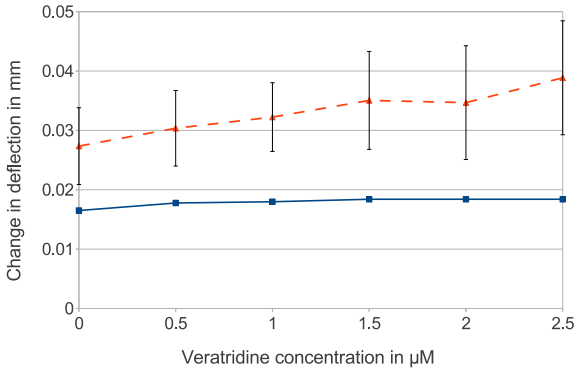

Figure 8.19: Veratridine affecting contractibility in experiment (*dashed*) and simulation (*continuous*); sample size $m = 3$

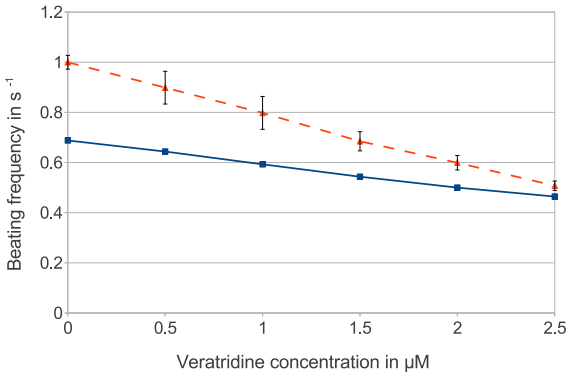

Figure 8.20: Veratridine affecting beating frequency in experiment (*dashed*) and simulation (*continuous*); sample size $m = 3$

concentration is set to 1 μM although more than 10 μM can be reached. Thus the maximum activation is already reached for comparably low Veratridine concentrations.

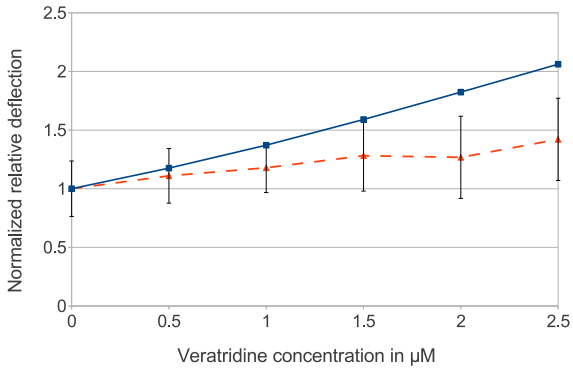

Figure 8.21: Disappearance of the inotropic saturation effect of Veratridine when using the TT-NHS model (*square markers*)

In fig. 8.21 this is proven by using the TT-NHS instead of the HMT-MNT model. Unlike the latter one, the former models ion dynamics in detail and is thus more appropriate. As a result the saturation effect disappears and the drug response in the model is qualitatively comparable to the experimental one. As a ventricular model, the TT-NHS model is externally paced at 1Hz by $52pA \cdot pF^{-1}$.

The experimentally determined negative chronotropic effect can be simulated as shown in figure 8.20. Here the major reason for the different slopes is supposed to be an inaccurate IC_{50} value.

8.3.3.4 Bay K8644 Modeling the effects of Bay K8644 differs from the other drugs because Bay K8644 does not block but stimulates activation and inactivation of the L-type calcium channels. Therefore potential shifts are introduced into the activation

(d-gate) and inactivation (f-gate) gate models as explained in sect. 5.4.2.2. Both, the half-maximal (in-)activation voltages V_{50} and the slope of (in-)activation S are changed according to experimental results found in SANGUINETTI [135]. Therein the change of test potentials according to drug actions has been investigated and some data points of the curves have been used for a parameter fitting. Table 8.6 summarizes how the two parameters should be changed with respect to the drug concentration.

Table 8.6: ΔV_{50}^x and ΔS^x for channel activation ($x = a$) and inactivation ($x = i$) through Bay K8644

Bay K8644 concentration	ΔV_{50}^a	ΔS^a	ΔV_{50}^i	ΔS^i
$30nM$	-6.60mV	0.00mV	-0.56mV	0.62mV
$60nM$	-8.44mV	0.00mV	-1.13mV	1.22mV
$90nM$	-9.51mV	0.00mV	-1.70mV	1.82mV
$120nM$	-10.27mV	0.00mV	-2.27mV	2.42mV
$150nM$	-10.86mV	0.00mV	-2.84mV	3.02mV

Figure 8.22 apparently is very similar to fig. 8.19 although here we can hardly see an increase in the deflection. Zooming in, one can observe a small inotropic effect and a saturation just like in the case of Veratridine, though.

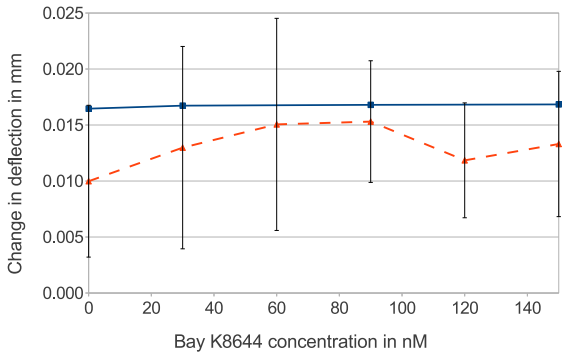

Figure 8.22: Bay K8644 affecting contractibility in experiment (*dashed*) and simulation (*continuous*); sample size $m = 5$

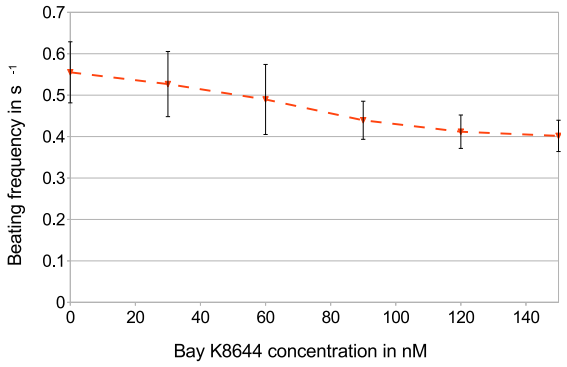

Figure 8.23: Bay K8644 affecting beating frequency in experiment; sample size $m = 5$

Again, the rudimentary calcium dynamics in the HMT-MNT model have been identified to be responsible for this behavior. Performing simulations with the TT-NHS model improves the results a lot and relaxes the saturation. This is shown in fig. 8.24.

Although the literature does not report about a significant influence of Bay K8644 on the beating frequency, experimental evidence is shown in fig. 8.23 that one exists in the case of the herein investigated hiPSc-derived cardiomyocytes. Thus this effect might be due to an immaturity of the cells. Similar differences between hiPSc-derived cardiomyocytes of heterogeneous origin and native cardiomyocytes have been found in JI ET AL. [80]

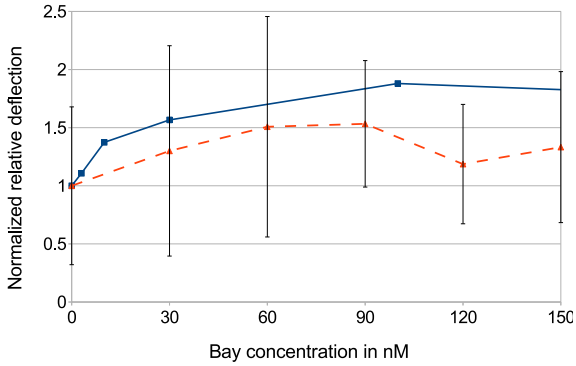

Figure 8.24: Disappearance of the inotropic saturation effect of Bay K8644 when using the TT-NHS model (*square markers*)

although beating frequency effects are not mentioned in there. Due to this disagreement and the resulting lack of supporting literature data, no simulations have been performed on the chronotropic effect of Bay K8644.

8.4 Discussion

In the previous section the results have been discussed already from a qualitative point of view. In summary these are:

- In the figures 8.13 and 8.14 one could clearly see that the presented model is able to qualitatively capture the negative inotropic and negative chronotropic effects of Lidocaine on hiPSC-CM.
- The same holds for the positive inotropic and negative chronotropic effects of Veratridine (cf. figures 8.21 and 8.20) although the inotropic effect initially was not captured due to a saturation in the Hunter excitation-contraction coupling. Replacing the Hunter model by the NHS model and using the TT model with more sophisticated ion dynamics instead of a combination of the MNT and Beeler-Reuter models solved this.
- From the figures 8.16 and 8.18 one could conclude that the negative inotropic effect of Verapamil is captured although the experimental curve is far from being linear like the simulation result. This might be due to the low sample size ($m = 3$) or due to unknown or unexplained effects.
- The positive inotropic effect of Bay K8644 could be simulated using the TT-NHS model as well (cf. fig. 8.24) including a decay in deflection for drug concentrations above $90nM$.
- The chronotropic effects of neither Verapamil nor Bay K8644 could not be captured. In the case of Verapamil the literature data on single cells suggest a negative

chronotropic effect whereas in monolayers the effect is positive. Of course the single cell MNT and TT models are not able to capture this effect without major modification (cf. fig 8.17). In the case of Bay K8644 no chronotropic effects are reported in the literature at all whereas a negative chronotropic effect could be observed in the CellDrum experiments (cf. 8.23).

- Including the FFR into the model is promising (see also Frotscher et al. [56]) but with an external pacing there is an overreaction of the model. An alternative will be discussed in sec. 9.2.2.

From a quantitative point of view one can state that in the control groups, i.e. without drug treatment, neither the simulated contractile change in deflection nor the beating frequency are equal to the experimental values. The reasons are quite manifold but the two major reasons are the FFR and the immaturity of the hiPSC-CM. Respecting the FFR in an appropriate way, i.e. by reparameterization of the model according to experimentally observed beating frequencies will adjust the beating force and thus the contractile change in deflection as well. First investigations in Frotscher et al. [56] show that the FFR indeed has a strong effect and should be regarded in modeling.

The immaturity of the hiPSC-CM though is a generic term for the lack of knowledge on the phenotypical expression of the individual ion channels in hiPSC-CM compared to native mammalian and human CM. The *in vitro* differentiation processes do not entirely reflect the *in vivo* processes and therefore some channels might express differently. Moreover the maturity of the cells depends on how long after the day of cultivation the experiments are performed. For this influence to be included in the model many patch clamp and MEA experiments are required. This way one could clearly specify the differences between the investigated hiPSC-CM and native CM and derive better predictions of drug effects. Computational models could support this by parameter studies that help to find the ion channels in question.

8.5 Simulation of Cardiac 3D Tissue

The heart of course is a 3D structure and it is well known that cells behave differently depending on their environment. This is especially true for a cell monolayer in which the cells are not organized in a 3D tissue. In a monolayer they can only communicate with each other in a 2D plane. Moreover the mechanical environment is influenced by the surface of the silicone membrane and the cells are flat in a monolayer whereas their shape is significantly different in a 3D tissue. Nevertheless, investigating cell monolayers first is a reasonable approach as this simplification leads to much more basic results. During this thesis no 3D tissues ($t > 100\,\mu m$) have been investigated on the CellDrum which is mainly due to manufacturing problems. The chemical fixation of the tissue containing the hiPSc-derived cardiac myocytes at this time was not strong enough to reliably connect a 3D tissue to the silicone membrane. Thus, lacking experimental data for 3D tissue it was necessary to focus on simulations of 2D tissue and the respective drug action.

First attempts to create 3D tissue consisting of hiPSC-CM and to investigate it in an

experimental setup have been successful as for instance in MATHUR ET AL. [102]. Therein the authors built a microfluidic device to measure the beating rate of the tissue based on computational motion-tracking in control conditions and with the option to apply drugs.

Surely the model can be applied to 3D tissues in the CellDrum setup as well although some changes will have to be made then:

- First of all the problem formulation will be three-dimensional and replace the plate formulation. This requires the usage of different finite elements. Regarding the results obtained by DUONG [42], a face-based smoothed finite element might be a good choice.
- The implemented material models and especially the electrophysiological models are implemented for a 2D domain. Those models need to be extended to the third dimension.
- In a larger piece of tissue than the one investigated here, the propagation of the membrane potential through the tissue has a large effect on the mechanical behavior. Moreover the heart only works if the electrical propagation works appropriately. Thus this needs to be modeled appropriately and also in three dimensions.

9 Summary and Conclusion

The central goal of this work was the computational investigation of drug action on cardiac tissue. Regarding the complexity of the human heart on each length scale, a simplifying inflation test, called CellDrum, has been chosen to measure beating forces and frequencies of cardiac monolayers. The system provides mechanical data for a cardiac monolayer consisting of hiPSC-derived cardiomyocytes, fibroblasts and an ECM that is chemically fixed on an ultra-thin silicone membrane.

The mechanical experimental data has been used as input and validation data for a FE based computational model. The shell FE model is able to capture the mechanics of the system and appropriate cellular electrophysiology models including the excitation-contraction coupling have been introduced on the level of the constitutive equations.

In the previous chapter the reader could see the capabilities of the model and the purpose of the following sections is mainly to point out necessary and nice-to-have model improvements and to point into rewarding future directions of research, especially concerning patient-specific investigation of drug action.

9.1 ES-FEM in Soft Tissue Mechanics

The edge-based S-FEM has been applied to the presented biomechanical plate problem. This method smooths a compatible, element-wise constant strain field across the edges of a standard FE mesh. Converting the integrals over smoothing domains to boundary integrals, the derivatives of shape functions and the isoparametric concept can be avoided. It has been shown that the ES-FEM-T3 element is superior to the standard FEM-T3 element and can be as accurate as the standard FEM-Q4. The only drawback is an increase in matrix bandwidth that is more than compensated by the gain in accuracy and the following properties of the method. For both, plate and three-dimensional applications (FS-FEM), it is a method that facilitates the handling of volumetric locking, mesh distortion, shear locking and that avoids remeshing.

Today, geometrical models of anatomical structures are very often created from MRI data, plastinates or other image processing methods, for instance for the heart (Jiang et al. [81]) and for pelvic floor structures (Bhattarai et al. [12] and van der Giessen et al. [153]). Especially in these non-generic models, automatic meshing algorithms often produce highly distorted elements from the image processing data. ES-FEM and FS-FEM do not only improve the accuracy of T3 and T4 elements, respectively, which might lead to the preference of T3 and T4 elements over T6 and T8 elements in some applications. Maybe even more importantly they avoid a singularity of the system matrix for very large aspect ratios. To demonstrate this the cantilever beam shown in figure 8.7 has been stretched to a length of $4800m$ and the tip load has been modified by $P = 0.001N$. The elements show aspect ratios greater than 50 and table 9.1 shows that standard FEM can hardly produce a solution different from zero and for slightly larger aspect ratios it will give a singular system matrix. ES-FEM on the other hand keeps two more decimal places and thus is able to handle much higher aspect ra-

tios than standard FEM. One can conclude that although the result will be inaccurate in the respective element, at least the computation is successful, whereas the standard FEM simply fails. Moreover, the result obtained with ES-FEM will still produce accurate results in regions that are not in the vicinity of this element.

Table 9.1: Beam tip deflection with aspect ratios above 50

Method	Beam tip deflection
Analytical	$-0.00853m$
FEM	$-0.00007m$
ES-FEM	$-0.00188m$

Not only in cardiovascular applications but for simulations anywhere in the human body this method proves to be beneficial. Very recently a selective S-FEM using both ES-FEM and NS-FEM has been successfully applied to the homogenization of incompressible materials in Li et al. [89]. Homogenization is a key topic in further modeling of cardiac tissue as pointed out in section 9.2.7.

The three-dimensional equivalent to ES-FEM, FS-FEM, as well has been applied in a selective setup to an anisotropic large deformation problem in Jiang et al. [81]. Therein the passive deformation behavior of a MRI-based heart geometry of a rabbit has been simulated.

9.2 Model Improvements

The presented simulation results for the pressure-deflection curves and the drug action on the CellDrum tissue show the capabilities of the proposed finite element model. In the results section it has been shown that a qualitatively correct simulation of drug action on cardiac tissue is fairly possible. However, there is a number of possible model improvements that shall become discussed here.

9.2.1 Shell and Finite Element Model

The currently employed plate and shell models are appropriate for the given task if techniques are applied that avoid transverse shear and volumetric locking. However, recent research on NURBS-based discretizations reveal great potentials for shell element development. Replacing the FEM with the *Isogeometric Analysis* that has been introduced by Hughes et al. [76] in 2005 and developed since then, as apparent from Cottrell et al. [32], introduces smooth and generally more continuous basis functions that can be used for the approximation of the geometry and the solution. Very recently an elegant *isogeometric shell element* formulation has been introduced by Echter et al. [45]. Due to its purely displacement-based formulation the shear gap method (cf. sect. 3.5) and related methods are obsolete because these isogeometric elements are shear locking-free by construction. The authors even state that each and every locking effect can be removed by relatively simple considerations that have to be made in

the near future. The simplicity of the proposed isogeometric shell elements makes them a good choice for more complex thin tissue constructs that might become investigated in the CellDrum setup in the future where the currently used elements might fail.

9.2.2 Electrophysiology

It is well known that the cardiac tissue construct investigated in here, consists of a mixture of cells of the Cor.4U cell line of Axiogenesis AG, Cologne, approximately 60% ventricular, 30% atrial and 10% nodal cells. In the latest model at least two different cell types have been modeled. The Stewart model represents a human Purkinje fiber cell and serves as a pacemaker. The TT model, as a model of a human ventricular cell, is employed in the whole computational domain to drive the active tissue behavior.

In Frotscher et al. [56], the Stewart model has been replaced by models of human sinoatrial nodal cells. Therein the model of Chandler et al. [23] and Seemann et al. [137] has been employed that both have a complexity that is similar to that of the TT model. They are based on the atrial model of Courtemanche et al. [33]. Modifications on the ion channels and ion concentrations are made to match nodal characteristics and nodal ion currents are introduced based on recent data that have been published in Zhang et al. [164] and Verkerk et al. [154]. Further even more recent results on the funny current and the calcium dynamics in SAN cells (Verkerk et al. [155]) could be integrated in the nodal model. The Courtemanche model itself can serve as a human model of atrial cells.

Employing those three electrophysiological models would have the benefits of modeling purely human cells and of closely matching the cell types that are actually occuring on the CellDrum. In addition to that the models have very similar complexity, i.e. they all model round about 20 unknowns.

So far it has been difficult to adjust the frequency of the pacing model to the experimentally observed beating frequency of the cardiac tissue. The range of which is approximately 0.5–$1.2Hz$. In order to get the chronotropic effects of drugs right, it is reasonable to try to adjust the frequency of the new pacing model although it is parameterized appropriately for human nodal cells. The exemplary parameter study in fig. 9.1 shows that an adjustment of the maximal conductivity of the funny current, c_f can be made in order to get different beating frequencies.

From the cited literature it becomes apparent that this approach is reasonable. Nevertheless it should be regarded with caution as there are some inaccuracies:

- The funny current is not the only current that has an influence to the beating frequency. As it is a hyperpolarization-actived current that is active during phase 4 of the action potential one can assume that it is mainly responsible for the beating frequency. Nevertheless it is necessary to keep in mind that there are other currents that for instance shorten or lengthen the action potential or background currents that have a comparably strong influence during phase 4.

  In a Master thesis (Muanghong [108]), parameter studies similar to the one shown

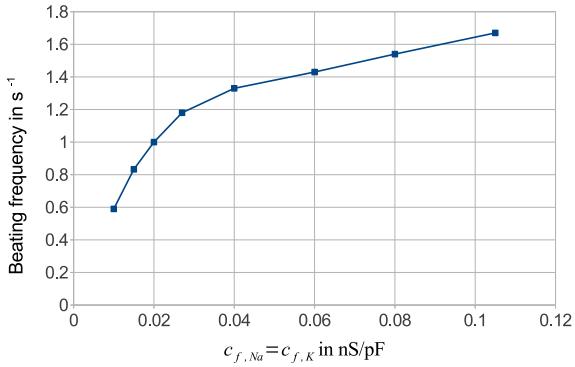

Figure 9.1: Influence of c_f on the beating frequency of the Stewart model

in fig. 9.1 are performed with respect to the Chandler SAN model. As can be seen in fig. 9.2, it has been found that the sodium-driven funny current $I_{f,Na}$, the inward rectifier potassium current I_{K1}, the transient outward current I_{to} and the T-type calcium current I_{CaT} have a strong influence on the beating frequency of the model. Currently, computational drug testing is performed on isolated cells in combination with modified conductance values in order to match the experimental beating frequencies. The goal is to construct hypotheses that can better explain the experimentally observed chronotropic effects of Lidocaine, Verapamil, Veratridine and Bay K8644 and that lead to assumptions concerning the ion channel expressions in the investigated cardiac monolayer.

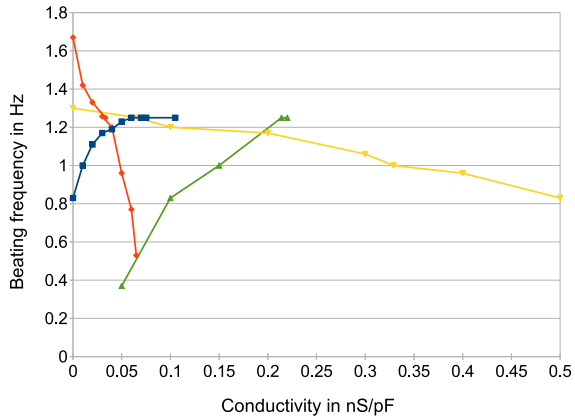

Figure 9.2: Influence of $c_{f,Na}$ (*blue square markers*), c_{K1} (*red diamond markers*), c_{to} (*yellow upside down triangular markers*) and c_{CaT} (*green triangular markers*) on the beating frequency of the Chandler model

- It is an ongoing debate, whether there exists a funny current at all or whether the contractile behavior of cardiac myocytes is driven by a so-called calcium clock (DiFrancesco [41], Li et al. [90]).

- Often the funny current is split up into a potassium- and a sodium-mediated part with separate maximum channel conductances. Applying the explained quite phenomenological approach requires equal maximum conductances if the funny current is split up. Otherwise there would be an infinite number of combinations leading to the same beating frequency.
- The experimental range of frequencies between $0.5Hz$ and $1.2Hz$ is quite large compared to what one would expect for healthy cells in a normal environment. This huge range might result from the fact that the hiPSC-CM are immature, i.e. not fully differentiated. Consequently there are lots of possible reasons for these differences and one has to keep in mind that a model of adult human cells is not fully valid for perhaps immature hiPSC-CM.

9.2.3 Model Adjustment to HiPSC-derived Cardiac Myocytes

This directly leads to the task of modeling hiPSC-CM instead of adult human cells. Although there are attempts of building models for those cells (Paci et al. [122]), in the author's opinion this is questionable for the given application for three main reasons:

1. It has been reported by Ji et al. [80] that there are huge quantitative and qualitative differences in the normal behavior and in the pharmacological response of hiPSC-CM coming from different cell cultures and vendors.
2. The immaturity of the cells is an uncontrollable issue that challenges any modeling attempt.
3. Stem cell researchers have the goal to better control the differentiation of hiPSC-CM in order to reproducibly get patient-specific cells that are functionally closer to their native counterparts (Liang and Du [91]). Consequently the cellular function of hiPSC-CM will change which always requires a model adaptation.

With the goal of simulating patient-specific drug treatment, it seems to be a better approach to use models for native human cells and, if necessary, to modify them according to the known functional differences of hiPSC-CM. Due to the named issues, it is currently impossible to build a globally valid model for hiPSC-CM but it is possible for native cells.

9.2.4 Passive Material Modeling

It is less a suggestion than more an obvious necessity that the passive material response needs to be modeled and parameterized appropriately. For the currently investigated tissue constructs the Neo-Hookean strain energy function sufficiently models the passive tissue behavior. Nevertheless the material parameter needs to be adjusted according to the mixture of different tissues and cells in the tissue construct that consists of different cardiomyocytes, fibroblasts, silicone and an ECM. Depending on the mixture ratio of the constituents the passive material behavior will change, i.e. the parameter fitting should be repeated.

9.2.5 ECM-dependent Model of Contraction

The mixture of cells mentioned in the previous section also has an influence on the overall contractile behavior of the tissue. It is well-known and has been investigated experimentally and computationally that the ratio between fibroblasts and cardiomyocytes Θ influences the contractile force (Xie et al. [158], Marquez et al. [99], Abney [1], Zhan et al. [163]). CellDrum experiments currently being in progress support this influence for the given monolayers. One could therefore suggest a modification of the reference tension $T_{ref}(\Theta)$ such that the contractibility of the cells directly depends on the portion of fibroblasts. Abney [1] shows that one might even be able to simply relate the passive stiffness to the fibroblast-to-cardiomyocyte ratio which allows for the interpretation that, up to a certain ratio, a stiffer cellular environment leads to more contraction due to an improved cell adhesion. Both, the fibroblast-to-cardiomyocyte ratio and the passive stiffness are known a-priori and from parameter fitting, respectively such that the model to be constructed can easily be verified.

9.2.6 Excitation-Contraction Coupling

The coupling of the cellular free inner calcium concentration to the active stress contribution is currently done using the NHS model. One suggestion is to split the active stress contribution

$$T_a(\Theta) = r_v T_{a,v}(\Theta) + r_a T_{a,a}(\Theta) + r_n T_{a,n}(\Theta) \tag{9.1}$$

into weighted contributions $T_{a,v}, T_{a,a}$ and $T_{a,n}$ from the ventricular, atrial and nodal cells, respectively. The weights are the volume ratio of the respective cell type with respect to the total amount of cells thus they fulfill

$$r_v + r_a + r_n = 1 \, . \tag{9.2}$$

Moreover, eq. (9.1) respects the fact that the different cell types show different contractile forces and that the respective change in contractile force depends differently on the fibroblast-to-cardiomyocyte ratio. It is an open issue how the differences in contractibility could be integrated in the model. Although the electrophysiological models compute different time courses of free inner calcium, the available models of excitation-contraction coupling do not further distinct cardiomyocytes. Possibly the actin-myosin kinetics and the binding of calcium to troponin C also differ for different types of cardiomyocytes. The cell type-specific parameterization of the NHS model could be attempted as in Tøndel et al. [150], where an approach is presented how to consider the inter-species dependency of the model parameters.

9.2.7 Homogenization

As pointed out by Ruiz-Baier et al. [132], bridging the scales via homogenization currently is not common in computational cardiac electromechanics. The current model is not an exception, it does not take into account the micro-structure of the tissue as generated by the mixture of cell types, local anisotropies or local cell-cell and the previously mentioned cell-ECM interactions. Global anisotropies, as given by the orientation of cardiac

muscles might be handled with macroscopic anisotropic constitutive laws as described in Holzapfel [72], for instance. In order to incorporate the local effects induced by cell-cell and cell-ECM interaction though, one has to perform a homogenization using a framework like the one presented and investigated in Miehe et al. [107]. A future work could consider these local effects by introducing a representative volume element of the micro-scale and a map to the macro-structure, like recently proposed in Keip et al. [83]. Problems like instabilities can arise from such a homogenization as pointed out in the cited paper. However, a homogenization framework as described therein, immensely increases the level of model detail and introduces some more model flexibility and local heterogeneity that is necessary to have when modeling living tissue. On the other hand one has to be careful because introducing more detail is computationally costly thus perhaps not all features of a chosen homogenization framework can be used. A first average-based homogenization approach avoiding reference volumes has been presented in Frotscher and Staat [51].

9.2.8 Modeling Drug Action, Diseases and Mutations

Especially with respect to the modeling of drug action, cardiac diseases and mutations the Hodgkin-Huxley (HH) models show a clear deficit because they lack heterogeneity. Heterogeneity of ion channels or protein function and cellular function also occurs in normal tissues. It means that, in contradiction to what is the outcome of a HH model, an ion channel shows a specific behavior, i.e. is in a state, with a certain probability. As a consequence a portion of ion channels of a given kind might be in the open state whereas another portion is in an inactivation state.

As already discussed in Frotscher et al. [55] a more recent approach is to use Markovian processes to model the ion channel expression rather than its phenotype (Clancy and Rudy [30]). In the cited paper a Markovian model of the fast sodium current I_{Na} that contributes to the depolarization phase of the membrane potential has been suggested. Therein it replaces the standard Hodgkin-Huxley representation of this current in the Luo-Rudy model (Luo and Rudy [98]). Figure 9.3 illustrates the model. Six different states have been modeled, namely three different closed states C1–C3, fast and slow inactivation states, IF and IS and an open state O. There is a certain probability

$$\begin{array}{rcl} & & \mathrm{IF} \rightleftarrows \mathrm{IS} \\ & \swarrow\!\!\nearrow & \uparrow\downarrow \\ \mathrm{C3} \rightleftarrows \mathrm{C2} \rightleftarrows \mathrm{C1} & \rightleftarrows & \mathrm{O} \end{array}$$

Figure 9.3: Markovian model of I_{Na}

for an ion channel to be in one of the states. The probabilities of being in a certain state are computed by solving the associated system of ordinary differential equations. In the end there will be a certain probability O_{Na} of a fast sodium channel being in the open state and the corresponding ion current is computed as usual by

$$I_{Na} = G_{Na} O_{Na} (V_m - E_{Na}) \, . \tag{9.3}$$

In HH models O_{Na} is replaced by a product of gate variables which govern opening and closure. The Markovian way of modeling shows some clear benefits:

- Replacing parts of an HH model by Markovian processes does not change the general type of the mathematical problem. The system to solve on cellular level still is a system of ordinary differential equations.
- The opening, closure, activation and inactivation kinetics of an ion channel can be modeled in very detail by introducing more states. Separation of slow and fast inactivation, for instance, is rather simple.
- The heterogeneity of ion channels within one cell is directly reflected by the states in which they can be with a certain probability. This way ion channel expression is modeled rather than its phenotype.

Related to that is the individualization of the Markovian ion channel model. One way of individualization is the adjustment of the transition rates between the states. For instance, Bondarenko et al. [17] succeeded in reparameterizing the Markovian model of I_{Na} in Clancy and Rudy [30] to match mouse data.

Another way of individualization is the introduction of additional states as for instance in Clancy and Rudy [30] and Clancy et al. [31]. In the former one the model shown in fig. 9.3 has been supplemented by four additional states to model the changes in protein function arising from the ΔKQP mutation in the SCN5A gene that causes long-QT syndrome. In the latter one the authors clearly showed the benefit of Markovian models being able to reflect heterogeneity. Therein the I_{Na} model has been amended again by four states and some transition rates have been adjusted to account for the 1795insD mutation in SCN5A. This mutation causes both, a long-QT syndrome and a Brugada syndrome which result in an enhanced and a reduced function of the fast sodium channel at the same time. Being able to model those opposing effects is important to distinct both effects from each other and to get the appropriate cellular response.

Those are only some examples one can find in the literature. The same arguments apply for heterogeneity in general and for drug or disease modeling in particular. Markovian models simply introduce much flexibility that is necessary for proper patient-specific simulation of cellular response.

9.2.9 Action Potential Conduction

The conduction of the action potential through the tissue has been ignored in this thesis and total synchrony of all cells has been assumed instead. The computational investigation of action potential conduction through the heart is a wide and important field and has been investigated a lot already, e.g. by Nash and Panfilov [110], Seemann et al. [137], Cherubini et al. [29], Pathmanathan and Whiteley [126], Göktepe and Kuhl [59], Göktepe et al. [61], Weise and Panfilov [156] and many many more. Respecting

the conduction, the systems of ordinary differential equations are formulated locally and are solved as an integral part of a globally parabolic system

$$\nabla \cdot (\boldsymbol{D}(\boldsymbol{C})\nabla V) = C(\boldsymbol{C})\frac{\partial V}{\partial t} + I_m(\boldsymbol{C}, t) \ , \tag{9.4}$$

with a strain-dependent conductivity tensor $\boldsymbol{D}(\boldsymbol{C})$, the potential V and capacitance C. The electrical source current I_m still results from the local cellular processes. This parabolic system is then coupled to the purely mechanical problem described by an elliptic differential equation. Such a framework is thoroughly described in Göktepe and Kuhl [60] and is schematically depicted in fig. 9.4. The nonlinear parabolic system that determines the action potential, provides activation characteristics that are forwarded to the nonlinear mechanical elliptic system. Therein, the activation drives the active stress component and the deformed structure is computed. Using mapping algorithms the electrical mesh is modified accordingly and the mechanical strain is projected onto the electrical mesh serving as input to the computation of the action potential. Both, the mechanical and the electrical model are solved by a Newton-Raphson algorithm due to their nonlinear nature. The nonlinearity of the parabolic system arises from the source term I_m on the right hand side of eq. (9.4). The source term is strongly varying in time and determined by a stiff system of ordinary differential equations.

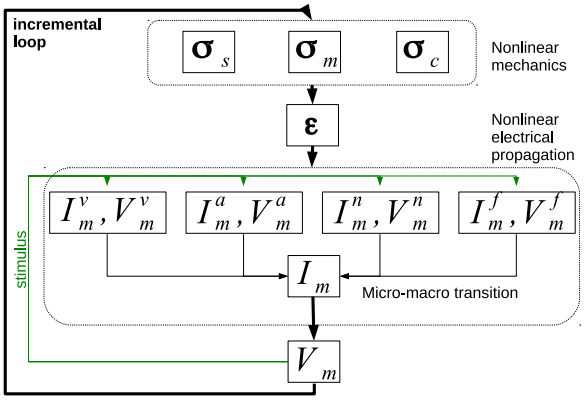

Figure 9.4: Flowchart of the incremental algorithm, the nonlinear mechanical and electrical model

Electrical conduction through cardiac tissue and the influence of the cellular environment on the cellular action potential, the action potential propagation and the active stress development are wide fields. It is well known that the mechanical behavior of cardiac cells in general and their contractile behavior in particular strongly defer whether they are isolated, in a cell cluster, in a monolayer or in a 3D tissue. Therefore, the modeling work done in this thesis should be incorporated in the larger framework of eq. (9.4), which already has been started as reported in Frotscher and Staat [52], Frotscher et al. [57] and Duong et al. [43]. Especially when patient-specific simulations should not only be performed on monolayers but on 3D tissues or even on the whole organ, this is essential.

9.3 Future Prospects

The CellDrum, the herein presented computational model, experimental setups and computational models all over the world in general share their future prospects because they have common goals. Research work at different length and time scales, be it experimental or computational, needs to be combined in order to reach the ultimate goals of patient-specific evaluation of drug action, patient-specific avoidance or treatment of cardiovascular diseases, patient-specific evaluation and perhaps control of mutations, reduction of animal and human experiments, safety of proposed treatments and patient-specific production of cardiovascular implants. The investigation of tissue that is mainly composed of hiPSC-derived cardiomyocytes is only one necessary step to reach these goals. With increasing amount and quality of data the computational models on all scales will help to better understand the inner workings of cardiomyocytes, the interaction of cardiomyocytes with the ECM, the electrical conduction through cardiac tissue and the effect of drugs on the whole heart of one specific human. It will be possible to perform only very few laboratory experiments on a piece of artificially created or stem cell-derived tissue and use the assistance of computational models to derive an individualized treatment of a cardiac disease. Contemporary computational models are strong and quite detailed but in the authors opinion there are two main challenges left with respect to this work.

Firstly, the amount of available experimental data is comparably low and it is obvious that the cellular behavior strongly depends on the cell or tissue environment. It seems as if a good approach would be to try to reproduce the cell environment that exists in the human heart as accurately as possible to be able to measure data that is valid for the actual heart tissue of a patient. In fact, this has been a central task in the development of experimental setups for a long time and currently available microfluidic devices connecting lung, heart, kidney and other organs are heading to this direction. The development of a true in vitro heart will take some time though due to the complexity of this organ. However, cultivation techniques are quite advanced already. Some research groups successfully cultivate ureter, skin and vascular tissue. It is only a matter of time when full organs can be created in vitro.

The second challenge that is faced at the current stage of knowledge is model flexibility. The experimental data in the cardiovascular field will always vary a lot due to the environment, temperature, pH, the donor's or patient's condition, differences in genetics, different ion channel expression, diseases and the external stress the tissue is experiencing. Cardiac cells and tissue are highly flexible in order to adopt to all kinds of external influences thus the models of cardiac cells, tissue or the heart need to show the same flexibility and heterogeneity to produce an outcome that is valid. Probabilistic modeling like the mentioned Markovian modeling will become very important when the patient-specific application of computational models will finally reach a state in which it is useful in daily practice. Deterministic models may hardly be sufficient to reflect the variety of responses that cardiac cells are able to give.

References

[1] T. Abney. *Interactions of cardiomyocytes and myofibroblasts : an experimental and theoretical model study*. PhD thesis, Washington University, St. Louis, USA, 2012.

[2] A. Agarwal, J. A. Goss, A. Cho, M. L. McCain, and K. K. Parker. Microfluidic heart on a chip for higher throughput pharmacological studies. *Lab on a Chip*, 13: 3599–608, 2013. doi: 10.1039/c3lc50350j.

[3] B. Alberts, A. Johnson, J. Lewis, M. Raff, K. Roberts, and P. Walter. *Molekularbiologie der Zelle*. Wiley-VCH Verlag & Co. KGaA, Weinheim, Germany, 5th edition, 2011. ISBN 978-3-527-32384-5.

[4] L. Arnold, J. Page, D. Attwell, M. Cannell, and D. A. Eisner. The dependence on heart rate of the human ventricular action potential duration. *Cardiovascular Research*, 16(10):547–51, Oct. 1982.

[5] A. Ay and D. N. Arnosti. Mathematical modeling of gene expression: a guide for the perplexed biologist. *Critical Reviews in Biochemistry and Molecular Biology*, 46 (2):137–51, Apr. 2011. doi: 10.3109/10409238.2011.556597.

[6] K.-J. Bathe. *Finite-Elemente-Methoden*. Springer Verlag, Berlin Heidelberg New York, 2002.

[7] R. Bayer. *Entwicklung eines Gefäßmodells zur biomechanischen Analyse von blutdrucksenkenden Medikamenten*. Phd thesis in progress (preliminary title), Universität Duisburg-Essen.

[8] R. Bayer. *Development of a multi-channel Tissue Tension Analyzer based on capacitive proximity sensor*. Master thesis, Aachen University of Applied Sciences, 2014.

[9] B. Y. G. W. Beeler and H. Reuter. Reconstruction of the action potential of ventricular myocardial fibres. *Journal of Physiology*, 268:177–210, 1977.

[10] K. Bersell, S. Arab, B. Haring, and B. Kühn. Neuregulin1/ErbB4 signaling induces cardiomyocyte proliferation and repair of heart injury. *Cell*, 138(2):257–70, July 2009. doi: 10.1016/j.cell.2009.04.060.

[11] P. Betsch, F. Gruttmann, and E. Stein. A 4-node finite shell element for the implementation of general hyperelastic 3D-elasticity at finite strains. *Computer Methods in Applied Mechanics and Engineering*, 130(1-2):57–79, Mar. 1996. doi: 10.1016/0045-7825(95)00920-5.

[12] A. Bhattarai, R. Frotscher, M.-C. Sora, and M. Staat. A 3D Finite Element model of the female pelvic floor for the reconstruction of urinary incontinence. In E. Oñate, J. Oliver, and A. Huerta (Ed.), *Proceedings 11th World Congress on Computational Mechanics (WCCM XI), 5th European Conference on Computational Mechanics*

(ECCM V), 6th European Conference on Computational Fluid Dynamics (ECFD VI), pages 923–934, Barcelona, Spain, 2014.

[13] M. Bischoff. *Theorie und Numerik einer dreidimensionalen Schalenformulierung*. PhD thesis, Universität Stuttgart, 1999.

[14] K.-U. Bletzinger, M. Bischoff, and E. Ramm. A unified approach for shear-locking-free triangular and rectangular shell finite elements. *Computers & Structures*, 75 (3):321–334, 2000. doi: 10.1016/S0045-7949(99)00140-6.

[15] M. Böl, S. Reese, K. K. Parker, and E. Kuhl. Computational modeling of muscular thin films for cardiac repair. *Computational Mechanics*, 43:535–544, 2009. doi: 10.1007/s00466-008-0328-5.

[16] M. Böl, O. J. Abilez, A. N. Assar, C. K. Zarins, and E. Kuhl. In vitro/in silico characterization of active and passive stresses in cardiac muscle. *International Journal for Multiscale Computational Engineering*, 10(2):171–188, 2012. doi: 10.1615/IntJMultCompEng.2011002352.

[17] V. E. Bondarenko, G. P. Szigeti, G. C. L. Bett, S.-J. Kim, and R. L. Rasmusson. Computer model of action potential of mouse ventricular myocytes. *American Journal of Physiology - Heart and Circulatory Physiology*, 287(3):H1378–403, Sept. 2004. doi: 10.1152/ajpheart.00185.2003.

[18] J. Bonet and R. D. Wood. *Nonlinear Continuum Mechanics for Finite Element Analysis*. Cambridge University Press, Cambridge, 2nd edition, 2008.

[19] S. P. Bordas, T. Rabczuk, N.-X. Hung, V. P. Nguyen, S. Natarajan, T. Bog, D. M. Quan, and N. V. Hiep. Strain smoothing in FEM and XFEM. *Computers & Structures*, 88(23-24):1419–1443, Dec. 2010. doi: 10.1016/j.compstruc.2008.07.006.

[20] D. M. Brill and J. A. Wasserstrom. Intracellular sodium and the positive inotropic effect of veratridine and cardiac glycoside in sheep Purkinje fibers. *Circulation Research*, 58(1):109–119, Jan. 1986. doi: 10.1161/01.RES.58.1.109.

[21] N. Büchter. *Zusammenführung von Degenerationskonzept und Schalentheorie bei endlichen Rotationen*. PhD thesis, Universität Stutgart, 1992.

[22] N. Büchter, E. Ramm, and D. Roehl. Three-dimensional extension of non-linear shell formulation based on the enhanced assumed strain concept. *International Journal for Numerical Methods in Engineering*, 37(15):2551–2568, 1994.

[23] N. J. Chandler, I. D. Greener, J. O. Tellez, S. Inada, H. Musa, P. Molenaar, D. Difrancesco, M. Baruscotti, R. Longhi, R. H. Anderson, R. Billeter, V. Sharma, D. C. Sigg, M. R. Boyett, and H. Dobrzynski. Molecular architecture of the human sinus node: insights into the function of the cardiac pacemaker. *Circulation*, 119 (12):1562–75, Mar. 2009. doi: 10.1161/CIRCULATIONAHA.108.804369.

[24] D. Chapelle and K.-J. Bathe. *The Finite Element Analysis of Shells - Fundamentals*. Computational Fluid and Solid Mechanics. Springer Verlag, Berlin Heidelberg New York, 2003.

[25] J. Chen, C. Wu, and T. Belytschko. Regularization of material instabilities by meshfree approximations with intrinsic length scales. *International Journal for Numerical Methods in Engineering*, 47(July 1999):1303–1322, 2000. doi: 10.1002/(SICI)1097-0207(20000310)47:7⟨1303::AID-NME826⟩3.0.CO;2-5.

[26] J.-S. Chen, C.-T. Wu, S. Yoon, and Y. You. A stabilized conforming nodal integration for galerkin mesh-free methods. *International Journal for Numerical Methods in Engineering*, 50(2):435–466, 2001. doi: 10.1002/1097-0207(20010120)50:2⟨435::AID-NME32⟩3.0.CO;2-A.

[27] L. Chen, G. Liu, Y. Jiang, K. Zeng, and J. Zhang. A singular edge-based smoothed finite element method (ES-FEM) for crack analyses in anisotropic media. *Engineering Fracture Mechanics*, 78(1):85–109, Jan. 2011. doi: 10.1016/j.engfracmech.2010.09.018.

[28] X. Chen, X. Zhang, D. M. Harris, V. Piacentino, R. M. Berretta, K. B. Margulies, and S. R. Houser. Reduced effects of BAY K 8644 on L-type Ca2+ current in failing human cardiac myocytes are related to abnormal adrenergic regulation. *American Journal of Physiology - Heart and Circulatory Physiology*, 294(5):H2257–67, May 2008. doi: 10.1152/ajpheart.01335.2007.

[29] C. Cherubini, S. Filippi, P. Nardinocchi, and L. Teresi. An electromechanical model of cardiac tissue: constitutive issues and electrophysiological effects. *Progress in Biophysics and Molecular Biology*, 97(2-3):562–73, 2008. doi: 10.1016/j.pbiomolbio.2008.02.001.

[30] C. E. Clancy and Y. Rudy. Linking a genetic defect to its cellular phenotype in a cardiac arrhythmia. *Nature*, 400(6744):566–9, Aug. 1999. doi: 10.1038/23034.

[31] C. E. Clancy, M. Tateyama, and R. S. Kass. Insights into the molecular mechanisms of bradycardia-triggered arrhythmias in long QT-3 syndrome. *The Journal of Clinical Investigation*, 110(9):1251–62, Nov. 2002. doi: 10.1172/JCI15928.

[32] J. A. Cottrell, T. J. R. Hughes, and Y. Bazilevs. *Isogeometric Analysis*. John Wiley & Sons, Ltd, Chichester, UK, Aug. 2009. ISBN 9780470749081. doi: 10.1002/9780470749081.

[33] M. Courtemanche, R. J. Ramirez, and S. Nattel. Ionic mechanisms underlying human atrial action potential properties: insights from a mathematical model. *The American Journal of Physiology*, 275(1 Pt 2):H301–21, July 1998.

[34] M. A. Crisfield. *Non-linear Finite Element Analysis of Solids and Structures, Volume 1 Essentials*. John Wiley & Sons Ltd, Chichester, UK, 1991.

[35] M. A. Crisfield. *Non-linear Finite Element Analysis of Solids and Structures, Volume 2 Advanced Topics*. John Wiley & Sons Ltd, Chichester, UK, 1997.

[36] X. Cui, G. Liu, G. Li, G. Zhang, and G. Sun. Analysis of elasticplastic problems using edge-based smoothed finite element method. *International Journal of Pressure Vessels and Piping*, 86(10):711–718, Oct. 2009. doi: 10.1016/j.ijpvp.2008.12.004.

[37] X. Cui, G.-R. Liu, G.-y. Li, G. Zhang, and G. Zheng. Analysis of plates and shells using an edge-based smoothed finite element method. *Computational Mechanics*, 45(2-3):141–156, Oct. 2009. doi: 10.1007/s00466-009-0429-9.

[38] X. Y. Cui, G. R. Liu, G. Y. Li, X. Zhao, T. T. Nguyen, and G. Y. Sun. A Smoothed Finite Element Method (SFEM) for linear and geometrically nonlinear analysis of plates and shells. *CMES*, 28:109–125, 2008.

[39] K. Dai and G. Liu. Free and forced vibration analysis using the smoothed finite element method (SFEM). *Journal of Sound and Vibration*, 301(3-5):803–820, Apr. 2007. doi: 10.1016/j.jsv.2006.10.035.

[40] K. Dai, G. Liu, and T. Nguyen. An n-sided polygonal smoothed finite element method (nSFEM) for solid mechanics. *Finite Elements in Analysis and Design*, 43 (11-12):847–860, Aug. 2007. doi: 10.1016/j.finel.2007.05.009.

[41] D. DiFrancesco. The role of the funny current in pacemaker activity. *Circulation Research*, 106(3):434–46, Feb. 2010. doi: 10.1161/CIRCRESAHA.109.208041.

[42] M. T. Duong. *Hyperelastic Modeling and Soft-Tissue Growth integrated with the Smoothed Finite Element Method-SFEM*. PhD thesis, RWTH Aachen University, 2014.

[43] M. T. Duong, A. Jung, R. Frotscher, and M. Staat. A 3D electromechanical FEM-based model for cardiac tissue. In M. Papadrakakis, V. Papadopoulos, and V. P. Stefanou (Ed.), *ECCOMAS Congress 2016, VII European Congress on Computational Methods in Applied Sciences and Engineering*, Crete Island, Greece, 2016.

[44] V. Ebbing. *Design of Polyconvex Energy Functions for All Anisotropy Classes*. PhD thesis, University Duisburg-Essen, 2010.

[45] R. Echter, B. Oesterle, and M. Bischoff. A hierarchic family of isogeometric shell finite elements. *Computer Methods in Applied Mechanics and Engineering*, 254: 170–180, Feb. 2013. doi: 10.1016/j.cma.2012.10.018.

[46] A. Eckstein. *Zur Theorie und Finite-Element-Simulation von Schalen mit großen elastischen Dehnungen und duktilen Schädigungen*. PhD thesis, Ruhr-Universität Bochum, 1999.

[47] J. P. Felix, B. S. Williams, B. T. Priest, R. M. Brochu, I. E. Dick, V. A. Warren, L. Yan, R. S. Slaughter, G. J. Kaczorowski, M. M. Smith, and M. L. Garcia. Functional assay of voltage-gated sodium channels using membrane potential-sensitive

dyes. *ASSAY and Drug Development Technologies*, 2(3):260–268, June 2004. doi: 10.1089/1540658041410696.

[48] F. Fenton and A. Karma. Vortex dynamics in three-dimensional continuous myocardium with fiber rotation: Filament instability and fibrillation. *Chaos (Woodbury, N.Y.)*, 8(1):20–47, Mar. 1998. doi: 10.1063/1.166311.

[49] F. H. Fenton and E. M. Cherry. Models of cardiac cell. *Scholarpedia*, 3(8):1868, 2008. doi: 10.4249/scholarpedia.1868.

[50] R. Frotscher and M. Staat. Application of an Edge-based Smoothed Finite Element Method on geometrically non-linear plates of non-linear material. In Eberhardsteiner, J; Böhm, H.J.; Rammerstorfer, F.G. (Eds.), *CD-ROM Proceedings of the 6th European Congress on Computational Methods in Applied Sciences and Engineering (ECCOMAS 2012)*, Vienna, 2012. Vienna University of Technology, Austria.

[51] R. Frotscher and M. Staat. Homogenization of a Cardiac Tissue Construct. In P. Nithiarasu and E. Budyn (Ed.), *Proceedings of the 4th International Conference on Computational and Mathematical Biomedical Engineering*, Cachan, France, 2015.

[52] R. Frotscher and M. Staat. An electromechanical model for cardiac tissue constructs. In S. Elgeti and J.-W. Simons (Ed.), *Proceedings of YIC GACM 2015, 3rd ECCOMAS Young Investigators Conference, 6th GACM Colloquium*, Aachen, Germany, 2015.

[53] R. Frotscher, J.-P. Koch, H.-J. Raatschen, and M. Staat. Evaluation of a computational model for drug action on cardiac tissue. In Onate, E.; Oliver, J.; Huerta, A. (Eds.), *Proceedings 11th World Congress on Computational Mechanics (WCCM XI), 5th European Conference on Computational Mechanics (ECCM V), 6th European Conference on Computational Fluid Dynamics (ECFD VI)*, pages 1425–1436, Barcelona, Spain, 2014.

[54] R. Frotscher, M. Goßmann, H.-J. Raatschen, A. Temiz-Artmann, and M. Staat. Simulation of cardiac cell-seeded membranes using the edge-based smoothed FEM. In Altenbach, Holm; Mikhasev, Gennadi (Eds.), *Shell and Membrane Theories in Mechanics and Biology: From Macro- to Nanoscale Structures*, chapter 11, pages 187–212. Springer, 2015. doi: 10.1007/978-3-319-02535-3_11.

[55] R. Frotscher, J.-P. Koch, and M. Staat. Towards patient-specific computational modeling of hiPS-derived cardiomyocytes. In G. M. Artmann (Eds.), *IFMBE Conference Proceedings of the 9th International Conference on Cell- and Stem Cell Engineering*, 2015.

[56] R. Frotscher, J.-P. Koch, and M. Staat. Computational investigation of drug action on human-induced stem cell-derived cardiomyocytes. *Journal of Biomechanical Engineering*, 137(7):071002–071002–7, 2015. doi: 10.1115/1.4030173.

[57] R. Frotscher, D. Muanghong, G. Dursun, M. Goßmann, A. Temiz-Artmann, and M. Staat. Sample-specific adaption of an improved electro-mechanical model of in vitro cardiac tissue. *Journal of Biomechanics*, 2016. doi: 10.1016/j.jbiomech.2016.01.039.

[58] M. Genet, L. C. Lee, B. Baillargeon, J. M. Guccione, and E. Kuhl. Modeling Pathologies of Diastolic and Systolic Heart Failure. *Annals of Biomedical Engineering*, 44 (1):112–127, Jan. 2016. doi: 10.1007/s10439-015-1351-2.

[59] S. Göktepe and E. Kuhl. Electromechanics of the heart: a unified approach to the strongly coupled excitationcontraction problem. *Computational Mechanics*, 45(2-3): 227–243, Nov. 2009. doi: 10.1007/s00466-009-0434-z.

[60] S. Göktepe and E. Kuhl. Computational modeling of cardiac electrophysiology: A novel finite element approach. *International Journal for Numerical Methods in Engineering*, 79(2):156–178, 2009. doi: 10.1002/nme.2571.

[61] S. Göktepe, A. Menzel, and E. Kuhl. Micro-structurally based kinematic approaches to electromechanics of the heart. In G. A. Holzapfel and E. Kuhl (Ed.), *Computer Models in Biomechanics*, chapter 13, pages 175–187. Springer, 1st edition, 2013. doi: 10.1007/978-94-007-5464-5_13.

[62] M. Goßmann. *Entwicklung eines autokontraktilen Herzmuskelmodells zur funktinalen Medikamenten- und Toxinforschung*. PhD thesis, Universität Duisburg-Essen, 2015.

[63] M. Goßmann, R. Frotscher, P. Linder, S. Neumann, R. Bayer, M. Epple, M. Staat, A. Temiz-Artmann, and G. M. Artmann. Mechano-pharmacological characterization of cardiomyocytes derived from human induced pluripotent stem cells. *Cellular Physiology and Biochemistry*, 38:1182–1198, 2016. doi: 10.1159/000443124.

[64] A. Grosberg, P. W. Alford, M. L. McCain, and K. K. Parker. Ensembles of engineered cardiac tissues for physiological and pharmacological study: Heart on a chip. *Lab on a Chip*, 11:4165–173, 2011. doi: 10.1039/C1LC20557A.

[65] J. M. Guccione, G. S. L. Prell, P. P. D. Tombe, and W. C. Hunter. Measurements of active myocardial tension under a wide range of physiological loading conditions. Technical Report 2, Department of Biomedical Engineering, The Johns Hopkins University, School of Medicine, Baltimore, 1997.

[66] L. Guo, R. M. C. Abrams, J. E. Babiarz, J. D. Cohen, S. Kameoka, M. J. Sanders, E. Chiao, and K. L. Kolaja. Estimating the risk of drug-induced proarrhythmia using human induced pluripotent stem cell-derived cardiomyocytes. *Toxicological Sciences : An Official Journal of the Society of Toxicology*, 123(1):281–289, 2011. doi: 10.1093/toxsci/kfr158.

[67] E. Hairer and G. Wanner. *Solving Ordinary Differential Equations II - Stiff and Differential-Algebraic Problems*. Springer, Berlin Heidelberg, 1st edition, 1991.

[68] K. Harris, M. Aylott, Y. Cui, J. B. Louttit, N. C. McMahon, and A. Sridhar. Comparison of electrophysiological data from human-induced pluripotent stem cell-derived cardiomyocytes to functional preclinical safety assays. *Toxicological Sciences : An Official Journal of the Society of Toxicology*, 134(2):412–26, Aug. 2013. doi: 10.1093/toxsci/kft113.

[69] A. V. Hill. The Heat of Shortening and the Dynamic Constants of Muscle. *Proceedings of the Royal Society B: Biological Sciences*, 126(843):136–195, Oct. 1938. doi: 10.1098/rspb.1938.0050.

[70] R. J. Hill, H. J. Duff, and R. S. Sheldon. Class I antiarrhythmic drug receptor: biochemical evidence for state-dependent interaction with quinidine and lidocaine. *Molecular Pharmacology*, 36(1):150–9, July 1989.

[71] A. L. Hodgkin and A. F. Huxley. A quantitative description of membrane current and its application to conduction and excitation in nerve. *The Journal of Physiology*, 117(4):500–44, Aug. 1952.

[72] G. A. Holzapfel. *A Continuum Approach for Engineering/Nonlinear Solid Mechanics*. John Wiley & Sons Ltd, Chichester, UK, 2000.

[73] G. A. Holzapfel and R. W. Ogden. Constitutive modelling of passive myocardium: a structurally based framework for material characterization. *Philosophical Transactions. Series A, Mathematical, Physical, and Engineering Sciences*, 367(1902): 3445–75, Sept. 2009. doi: 10.1098/rsta.2009.0091.

[74] P. Honerjäger and M. Reiter. The relation between the effects of veratridine on action potential and contraction in mammalian ventricular myocardium. *Naunyn-Schmiedeberg's Archives of Pharmacology*, 289(1):1–28, Jan. 1975.

[75] Z. Hu, M. Qian, and M. Q. Zhang. Novel Markov model of induced pluripotency predicts gene expression changes in reprogramming. *BMC Systems Biology*, 5(Suppl 2), Dec. 2011. doi: 10.1186/1752-0509-5-S2-S8.

[76] T. Hughes, J. Cottrell, and Y. Bazilevs. Isogeometric analysis: CAD, finite elements, NURBS, exact geometry and mesh refinement. *Computer Methods in Applied Mechanics and Engineering*, 194(39-41):4135–4195, Oct. 2005. doi: 10.1016/j.cma.2004.10.008.

[77] J. D. Humphrey. *Cardiovascular Solid Mechanics - Cells, Tissues, and Organs*. Springer, New York, 2002.

[78] P. J. Hunter, A. D. McCulloch, and H. ter Keurs. Modelling the mechanical properties of cardiac muscle. *Progress in Biophysics and Molecular Biology*, 69(2-3): 289–331, 1998. doi: 10.1016/S0079-6107(98)00013-3.

[79] P. J. Hunter, A. J. Pullan, and B. H. Smaill. Modeling total heart function. *Annual Review of Biomedical Engineering*, 5:147–77, Jan. 2003. doi: 10.1146/annurev.bioeng.5.040202.121537.

[80] J. Ji, J. Kang, and D. Rampe. L-type ca(2+) channel responses to bay k 8644 in stem cell-derived cardiomyocytes are unusually dependent on holding potential and charge carrier. *Assay and Drug Development Technologies*, 12(6):352–60, Aug. 2014. doi: 10.1089/adt.2014.596.

[81] C. Jiang, G.-R. Liu, X. Han, Z.-Q. Zhang, and W. Zeng. A smoothed finite element method for analysis of anisotropic large deformation of passive rabbit ventricles in diastole. *International Journal for Numerical Methods in Biomedical Engineering*, 31(1):1–25, 2015. doi: 10.1002/cnm.2697.

[82] J. Kang, X.-l. Chen, J. Ji, Q. Lei, and D. Rampe. Ca channel activators reveal differential L-type Ca channel pharmacology between native and stem cell-derived cardiomyocytes. *The Journal of Pharmacology and Experimental Therapeutics*, 341 (2):510–7, May 2012. doi: 10.1124/jpet.112.192609.

[83] M.-A. Keip, P. Steinmann, and J. Schröder. Two-scale computational homogenization of electro-elasticity at finite strains. *Computer Methods in Applied Mechanics and Engineering*, 278:62–79, Aug. 2014. doi: 10.1016/j.cma.2014.04.020.

[84] J.-P. Koch. *Modeling and simulation of the effects of cardioactive drugs on beating cardiomyocytes*. Master thesis, Aachen University of Applied Sciences, 2014.

[85] F. Koschnick. *Geometrische Locking-Effekte bei finiten Elementen und ein allgemeines Konzept zu ihrer Vermeidung*. PhD thesis, Technische Universität München, 2004.

[86] F. Koschnick, M. Bischoff, N. Camprubí, and K.-U. Bletzinger. The discrete strain gap method and membrane locking. *Computer Methods in Applied Mechanics and Engineering*, 194(21-24):2444–2463, June 2005. doi: 10.1016/j.cma.2004.07.040.

[87] J. Kramer, C. A. Obejero-Paz, G. Myatt, Y. A. Kuryshev, A. Bruening-Wright, J. S. Verducci, and A. M. Brown. MICE models: superior to the HERG model in predicting Torsade de Pointes. *Scientific Reports*, 3:2100, Jan. 2013. doi: 10.1038/srep02100.

[88] H. le Dret and A. Raoult. The quasiconvex envelope of the Saint Venant-Kirchhoff stored energy function. In P. G. Ciarlet, L. Trabucho, and J. M. Viano (Ed.), *Asymptotic Methods for Elastic Structures: Proceedings of the International Conference, Lisbon, Portugal, October 4-8, 1993*, pages 171–180. De Gruyter, 1995.

[89] E. Li, Z. Zhang, C. Chang, G. Liu, and Q. Li. Numerical homogenization for incompressible materials using selective smoothed finite element method. *Composite Structures*, 123:216–232, 2015. doi: 10.1016/j.compstruct.2014.12.016.

[90] P. Li, G. T. Lines, M. M. Maleckar, and A. Tveito. Mathematical models of cardiac pacemaking function. *Frontiers in Physics*, 1(October):1–13, 2013. doi: 10.3389/fphy.2013.00020.

[91] P. Liang and J. Du. Human induced pluripotent stem cell for modeling cardiovascular diseases. *Regenerative Medicine Research*, 2(1):4, 2014. doi: 10.1186/2050-490X-2-4.

[92] P. Liang, F. Lan, A. S. Lee, T. Gong, V. Sanchez-Freire, Y. Wang, S. Diecke, K. Sallam, J. W. Knowles, P. J. Wang, P. K. Nguyen, D. M. Bers, R. C. Robbins, and J. C. Wu. Drug screening using a library of human induced pluripotent stem cell-derived cardiomyocytes reveals disease-specific patterns of cardiotoxicity. *Circulation*, 127 (16):1677–91, May 2013. doi: 10.1161/CIRCULATIONAHA.113.001883.

[93] P. Linder, J. Trzewik, M. Rüffer, G. M. Artmann, I. Digel, R. Kurz, A. Rothermel, A. Robitzki, and A. Temiz Artmann. Contractile tension and beating rates of self-exciting monolayers and 3D-tissue constructs of neonatal rat cardiomyocytes. *Medical & Biological Engineering & Computing*, 48(1):59–65, Jan. 2010. doi: 10.1007/s11517-009-0552-y.

[94] G. Liu, N. Nourbakhshnia, and Y. Zhang. A novel singular ES-FEM method for simulating singular stress fields near the crack tips for linear fracture problems. *Engineering Fracture Mechanics*, 78(6):863–876, Apr. 2011. doi: 10.1016/j.engfracmech.2009.11.004.

[95] G. R. Liu and T. T. Nguyen. *Smoothed Finite Element Methods*. CRC Press, Boca Raton, 2010. ISBN 9781439820278.

[96] G. R. Liu, K. Y. Dai, and T. T. Nguyen. A Smoothed Finite Element Method for mechanics problems. *Computational Mechanics*, 39(6):859–877, 2007.

[97] G. R. Liu, T. Nguyen-Thoi, and K. Y. Lam. An edge-based smoothed finite element method (ES-FEM) for static, free and forced vibration analyses of solids. *Journal of Sound and Vibration*, 320(4-5):1100–1130, 2009. doi: 10.1016/j.jsv.2008.08.027.

[98] C. H. Luo and Y. Rudy. A dynamic model of the cardiac ventricular action potential. I. Simulations of ionic currents and concentration changes. *Circulation Research*, 74 (6):1071–1096, June 1994. doi: 10.1161/01.RES.74.6.1071.

[99] J. P. Marquez, E. L. Elson, and G. M. Genin. Whole cell mechanics of contractile fibroblasts: relations between effective cellular and extracellular matrix moduli. *Philosophical Transactions. Series A, Mathematical, Physical, and Engineering Sciences*, 368(1912):635–54, Mar. 2010. doi: 10.1098/rsta.2009.0240.

[100] J. E. Marsden and T. J. R. Hughes. *Mathematical Foundations of Elasticity*. Dover, Mineola, NY, USA, 1984.

[101] J. Martins, E. Pires, R. Salvado, and P. Dinis. A numerical model of passive and active behavior of skeletal muscles. *Computer Methods in Applied Mechanics and Engineering*, 151(3-4):419–433, Jan. 1998. doi: 10.1016/S0045-7825(97)00162-X.

[102] A. Mathur, P. Loskill, K. Shao, N. Huebsch, S. Hong, S. G. Marcus, N. Marks, M. Mandegar, B. R. Conklin, L. P. Lee, and K. E. Healy. Human iPSC-based Cardiac Microphysiological System For Drug Screening Applications. *Scientific reports*, 5: 1–7, 2015. doi: 10.1038/srep08883.

[103] R. E. McAllister, D. Noble, and R. W. Tsien. Reconstruction of the electrical activity of cardiac Purkinje fibres. *The Journal of Physiology*, 251(1):1–59, Sept. 1975.

[104] A. Mehta, Y. Y. Chung, A. Ng, F. Iskandar, S. Atan, H. Wei, G. Dusting, W. Sun, P. Wong, and W. Shim. Pharmacological response of human cardiomyocytes derived from virus-free induced pluripotent stem cells. *Cardiovascular Research*, 91(4):577–86, Sept. 2011. doi: 10.1093/cvr/cvr132.

[105] Q.-T. Meng, Z.-Y. Xia, J. Liu, D. A. Bayliss, and X. Chen. Local anesthetic inhibits hyperpolarization-activated cationic currents. *Molecular Pharmacology*, 79(5):866–73, May 2011. doi: 10.1124/mol.110.070227.

[106] C. Miehe and J. Schröder. Energy and momentum conserving elastodynamics of a non-linear brick-type mixed finite shell element. *International Journal for Numerical Methods in Engineering*, 50(8):1801–1823, Mar. 2001. doi: 10.1002/nme.95.

[107] C. Miehe, J. Schröder, and M. Becker. Computational homogenization analysis in finite elasticity: material and structural instabilities on the micro- and macro-scales of periodic composites and their interaction. *Computer Methods in Applied Mechanics and Engineering*, 191(44):4971–5005, Oct. 2002. doi: 10.1016/S0045-7825(02)00391-2.

[108] D. Muanghong. *Computational study of drug effects on human induced pluripotent stem cell-derived cardiomyocytes with adopted beating frequencies*. Master thesis, Aachen University of Applied Sciences, 2015.

[109] P. Nardinocchi and L. Teresi. On the active response of soft living tissues. *Journal of Elasticity*, 88:27–39, 2007. doi: 10.1007/s10659-007-9111-7.

[110] M. P. Nash and A. V. Panfilov. Electromechanical model of excitable tissue to study reentrant cardiac arrhythmias. *Progress in Biophysics and Molecular Biology*, 85(2-3):501–22, 2004. doi: 10.1016/j.pbiomolbio.2004.01.016.

[111] J. C. Nawroth, H. Lee, A. W. Feinberg, C. M. Ripplinger, M. L. McCain, A. Grosberg, J. O. Dabiri, and K. K. Parker. A tissue-engineered jellyfish with biomimetic propulsion. *Nature Biotechnology*, 30(8):792–797, 2012. doi: 10.1038/nbt.2269.

[112] T. Nguyen-Thoi, G. R. Liu, K. Y. Lam, and G. Y. Zhang. A face-based smoothed finite element method (FS-FEM) for 3D linear and geometrically non-linear solid mechanics problems using 4-node tetrahedral elements. *International Journal for Numerical Methods in Engineering*, 78(3):324–353, Apr. 2009. doi: 10.1002/nme.2491.

[113] H. Nguyen-Xuan, G. Liu, C. Thai-Hoang, and T. Nguyen-Thoi. An edge-based smoothed finite element method (ES-FEM) with stabilized discrete shear gap technique for analysis of ReissnerMindlin plates. *Computer Methods in Applied Mechanics and Engineering*, 199(9-12):471–489, Jan. 2010. doi: 10.1016/j.cma.2009.09.001.

[114] H. Nguyen-Xuan, G. R. Liu, C. Thai-Hoang, and T. Nguyen-Thoi. An edge-based smoothed finite element method (ES-FEM) with stabilized discrete shear gap technique for analysis of Reissner-Mindlin plates. *Computational Methods in Applied Mechanics and Engineering*, 199:471–489, 2010. doi: 10.1016/j.cma.2009.09.001.

[115] D. P. Nickerson. *Cardiac Electro-Mechanics : From cellML to the Whole Heart*. PhD thesis, University of Auckland, 2004.

[116] S. A. Niederer and N. P. Smith. An improved numerical method for strong coupling of excitation and contraction models in the heart. *Progress in Biophysics and Molecular Biology*, 96(1-3):90–111, 2008. doi: 10.1016/j.pbiomolbio.2007.08.001.

[117] S. A. Niederer, P. J. Hunter, and N. P. Smith. A quantitative analysis of cardiac myocyte relaxation: a simulation study. *Biophysical Journal*, 90(5):1697–722, Mar. 2006. doi: 10.1529/biophysj.105.069534.

[118] Y. Nix, R. Frotscher, and M. Staat. Implementation of the Edge-based Smoothed Extended Finite Element Method. In Eberhardsteiner, J.; Böhm, H.J.; Rammerstorfer, F.G. (Eds.), *CD-ROM Proceedings of the 6th European Congress on Computational Methods in Applied Sciences and Engineering (ECCOMAS 2012)*, Vienna, 2012. Vienna University of Technology, Austria.

[119] F. Nobile, A. Quarteroni, and R. Ruiz-Baier. An active strain electromechanical model for cardiac tissue. *International Journal for Numerical Methods in Biomedical Engineering*, 28(1):52–71, Jan. 2012. doi: 10.1002/cnm.1468.

[120] D. Noble. A modification of the Hodgkin–Huxley equations applicable to Purkinje fibre action and pace-maker potentials. *The Journal of Physiology*, 160:317–52, Feb. 1962.

[121] C. Obiol-Pardo, J. Gomis-Tena, F. Sanz, J. Saiz, and M. Pastor. A multiscale simulation system for the prediction of drug-induced cardiotoxicity. *Journal of Chemical Information and Modeling*, 51(2):483–92, Feb. 2011. doi: 10.1021/ci100423z.

[122] M. Paci, J. Hyttinen, K. Aalto-Setälä, and S. Severi. Computational models of ventricular- and atrial-like human induced pluripotent stem cell derived cardiomyocytes. *Annals of Biomedical Engineering*, 41(11):2334–48, Nov. 2013. doi: 10.1007/s10439-013-0833-3.

[123] S. K. Pakazad, A. M. Savov, A. van de Stolpe, S. Braam, B. van Meer, and R. Dekker. A stretchable Micro-Electrode Array for in vitro electrophysiology. In *2011 IEEE 24th International Conference on Micro Electro Mechanical Systems*, pages 829–832. IEEE, Jan. 2011. ISBN 978-1-4244-9632-7. doi: 10.1109/MEMSYS.2011.5734553.

[124] S. K. Pakazad, A. Savov, S. R. Braam, and R. Dekker. A platform for manufacturable stretchable Micro-Electrode Arrays. *Procedia Engineering*, 47:817–820, 2012. doi: 10.1016/j.proeng.2012.09.272.

[125] S. K. Pakazad, A. Savov, A. van de Stolpe, and R. Dekker. A novel stretchable micro-electrode array (SMEA) design for directional stretching of cells. *Journal of Micromechanics and Microengineering*, 24:034003, 2014. doi: 10.1088/0960-1317/24/3/034003.

[126] P. Pathmanathan and J. P. Whiteley. A numerical method for cardiac mechanoelectric simulations. *Annals of Biomedical Engineering*, 37(5):860–73, May 2009. doi: 10.1007/s10439-009-9663-8.

[127] J. F. Quintão Júnior, A. J. Natali, M. A. Carneiro-Júnior, C. A. de Castro, L. R. Drummond, V. N. Lavorato, L. B. Felix, J. d. S. Cruz, and T. N. Prímola-Gomes. Morphology and contractility in cardiomyocytes of rats with low exercise performance. *Arquivos Brasileiros de Cardiologia*, 98(5):431–6, May 2012.

[128] D. M. Roden and C. C. Hong. Stem cell-derived cardiomyocytes as a tool for studying proarrhythmia: a better canary in the coal mine? *Circulation*, 127(16): 1641–3, Apr. 2013. doi: 10.1161/CIRCULATIONAHA.113.002127.

[129] D. Roehl. *Zur Berechnung von großen elastoplastischen Deformationen bei Flächentragwerken und Kontinua*. PhD thesis, Stuttgart, 1994.

[130] M. R. Rosen. Consequences of the Sicilian Gambit. *European Heart Journal*, 16 Suppl G:32–6, Aug. 1995.

[131] S. Rossi, R. Ruiz-Baier, L. F. Pavarino, and A. Quarteroni. Orthotropic active strain models for the numerical simulation of cardiac biomechanics. *International Journal for Numerical Methods in Biomedical Engineering*, 28:761–788, 2012. doi: 10.1002/cnm.2473.

[132] R. Ruiz-Baier, D. Ambrosi, S. Pezzuto, S. Rossi, and A. Quarteroni. Activation models for the numerical simulation of cardiac electromechanical interactions. In G. A. Holzapfel and E. Kuhl (Ed.), *Computer Models in Biomechanics*, chapter 14, pages 189–201. Springer, 1st edition, 2013. doi: 10.1007/978-94-007-5464-5_14.

[133] R. Ruiz-Baier, A. Gizzi, S. Rossi, C. Cherubini, A. Laadhari, S. Filippi, and A. Quarteroni. Mathematical modelling of active contraction in isolated cardiomyocytes. *Mathematical Medicine and Biology : A Journal of the IMA*, pages 1–25, 2013. doi: 10.1093/imammb/dqt009.

[134] S. Saleh, S. Y. M. Yeung, S. Prestwich, V. Pucovsky, and I. Greenwood. Electrophysiological and molecular identification of voltage-gated sodium channels in murine vascular myocytes. *The Journal of Physiology*, 568(Pt 1):155–69, Oct. 2005. doi: 10.1113/jphysiol.2005.090951.

[135] M. C. Sanguinetti. Voltage-dependent modulation of Ca channel current in heart cells by Bay K8644. *The Journal of General Physiology*, 88(3):369–392, Sept. 1986. doi: 10.1085/jgp.88.3.369.

[136] W. K. Schomburg. Introduction to Microsystem Design. In *Introduction to Microsystem Design*, volume 1, pages 29–52. Springer Berlin Heidelberg, 2011. ISBN 978-3-642-19488-7. doi: 10.1007/978-3-642-19489-4.

[137] G. Seemann, C. Höper, F. B. Sachse, O. Dössel, A. V. Holden, and H. Zhang. Heterogeneous three-dimensional anatomical and electrophysiological model of human atria. *Philosophical Transactions. Series A, Mathematical, Physical, and Engineering Sciences*, 364(1843):1465–81, June 2006. doi: 10.1098/rsta.2006.1781.

[138] J. Simo, M. Rifai, and D. Fox. On a stress resultant geometrically exact shell model. Part IV: Variable thickness shells with through-the-thickness stretching. *Computer Methods in Applied Mechanics and Engineering*, 81(1):91–126, July 1990. doi: 10.1016/0045-7825(90)90143-A.

[139] J. C. Simo and F. Armero. Geometrically non-linear enhanced strain mixed methods and the method of incompatible modes. *International Journal for Numerical Methods in Engineering*, 33(7):1413–1449, May 1992. doi: 10.1002/nme.1620330705.

[140] O. Sirenko, C. Crittenden, N. Callamaras, J. Hesley, Y.-W. Chen, C. Funes, I. Rusyn, B. Anson, and E. F. Cromwell. Multiparameter in vitro assessment of compound effects on cardiomyocyte physiology using iPSC cells. *Journal of Biomolecular Screening*, 18(1):39–53, Jan. 2013. doi: 10.1177/1087057112457590.

[141] N. Smith, P. Mulquiney, M. Nash, C. Bradley, D. P. Nickerson, and P. Hunter. Mathematical modelling of the heart: cell to organ. *Chaos, Solitons & Fractals*, 13 (8):1613–1621, June 2002. doi: 10.1016/S0960-0779(01)00170-9.

[142] L. A. Spyrou. *Muscle and tendon tissues : constitutive modeling , numerical implementation and applications*. PhD thesis, University of Thessaly, 2009.

[143] P. Stewart, O. V. Aslanidi, D. Noble, P. J. Noble, M. R. Boyett, and H. Zhang. Mathematical models of the electrical action potential of Purkinje fibre cells. *Philosophical Transactions. Series A, Mathematical, Physical, and Engineering Sciences*, 367(1896):2225–55, June 2009. doi: 10.1098/rsta.2008.0283.

[144] S. Stoelzle, A. Haythornthwaite, R. Kettenhofen, E. Kolossov, H. Bohlen, M. George, A. Brüggemann, and N. Fertig. Automated patch clamp on mESC-derived cardiomyocytes for cardiotoxicity prediction. *Journal of Biomolecular Screening*, 16 (8):910–6, Oct. 2011. doi: 10.1177/1087057111413924.

[145] K. Takahashi and S. Yamanaka. Induction of pluripotent stem cells from mouse embryonic and adult fibroblast cultures by defined factors. *Cell*, 126(4):663–76, Aug. 2006. doi: 10.1016/j.cell.2006.07.024.

[146] K. H. W. J. ten Tusscher and A. V. Panfilov. Alternans and spiral breakup in a human ventricular tissue model. *American Journal of Physiology - Heart and Circulatory Physiology*, 291(3):H1088–100, Sept. 2006. doi: 10.1152/ajpheart.00109.2006.

[147] K. H. W. J. ten Tusscher, D. Noble, P. J. Noble, and A. V. Panfilov. A model for human ventricular tissue. *American Journal of Physiology - Heart and Circulatory Physiology*, 286(4):H1573–89, Apr. 2004. doi: 10.1152/ajpheart.00794.2003.

[148] Y. Terasawa. Improved strategies for nonclinical cardiac safety assessment. Technical report, ChanTest, 2011.

[149] G. Thomas, M. Chung, and C. J. Cohen. A dihydropyridine (Bay k 8644) that enhances calcium currents in guinea pig and calf myocardial cells. A new type of positive inotropic agent. *Circulation Research*, 56(1):87–96, Jan. 1985. doi: 10.1161/01.RES.56.1.87.

[150] K. Tøndel, S. Land, S. A. Niederer, and N. P. Smith. Quantifying inter-species differences in contractile function through biophysical modelling. *The Journal of Physiology*, 593(5):1083–1111, 2015. doi: 10.1113/jphysiol.2014.279232.

[151] J. Trzewik. *Experimental analysis of biaxial mechanical tension in cell monolayers and cultured three-dimensional tissues*. PhD thesis, Technical University Illmenau, 2008.

[152] J. Trzewik, A. Artmann-Temiz, P. T. Linder, T. Demirci, I. Digel, and G. M. Artmann. Evaluation of lateral mechanical tension in thin-film tissue constructs. *Annals of Biomedical Engineering*, 32(9):1243–51, Sept. 2004.

[153] A. G. van der Giessen, H. C. Groen, P. A. Doriot, P. J. de Feyter, A. F. W. van der Steen, F. N. van de Vosse, J. J. Wentzel, and F. J. H. Gijsen. The influence of boundary conditions on wall shear stress distribution in patients specific coronary trees. *Journal of Biomechanics*, 44:1089–1095, 2015. doi: 10.1016/j.jbiomech.2011.01.036.

[154] A. O. Verkerk, M. M. G. J. van Borren, R. J. G. Peters, E. Broekhuis, K. Y. Lam, R. Coronel, J. M. T. de Bakker, H. L. Tan, and R. Wilders. Single cells isolated from human sinoatrial node: action potentials and numerical reconstruction of pacemaker current. *Engineering in Medicine and Biology Society, 2007. EMBS 2007. 29th Annual International Conference of the IEEE*, pages 904–7, Jan. 2007. doi: 10.1109/IEMBS.2007.4352437.

[155] A. O. Verkerk, M. M. G. J. van Borren, and R. Wilders. Calcium transient and sodium-calcium exchange current in human versus rabbit sinoatrial node pacemaker cells. *The Scientific World Journal*, 2013:507872, Jan. 2013. doi: 10.1155/2013/507872.

[156] L. D. Weise and A. V. Panfilov. A discrete electromechanical model for human cardiac tissue: effects of stretch-activated currents and stretch conditions on restitution properties and spiral wave dynamics. *PloS One*, 8(3):e59317, Jan. 2013. doi: 10.1371/journal.pone.0059317.

[157] K. Willner. *Kontinuums- und Kontaktmechanik*. Springer, Berlin Heidelberg, 2003. ISBN 3540435298.

[158] Y. Xie, A. Garfinkel, P. Camelliti, P. Kohl, J. N. Weiss, and Z. Qu. Effects of fibroblast-myocyte coupling on cardiac conduction and vulnerability to reentry: A computational study. *Heart Rhythm : The Official Journal of the Heart Rhythm Society*, 6(11):1641–9, Nov. 2009. doi: 10.1016/j.hrthm.2009.08.003.

[159] H. Yamada. *Strength of Biological Materials*. William & Wilkins, Baltimore, 1970. ISBN 0683093231.

[160] N. Yokoo, S. Baba, S. Kaichi, A. Niwa, T. Mima, H. Doi, S. Yamanaka, T. Nakahata, and T. Heike. The effects of cardioactive drugs on cardiomyocytes derived from human induced pluripotent stem cells. *Biochemical and Biophysical Research Communications*, 387(3):482–8, Sept. 2009. doi: 10.1016/j.bbrc.2009.07.052.

[161] G. I. Zahalak, J. E. Wagenseil, T. Wakatsuki, and E. L. Elson. A cell-based constitutive relation for bio-artificial tissues. *Biophysical Journal*, 79(5):2369–81, Nov. 2000. doi: 10.1016/S0006-3495(00)76482-4.

[162] A. Zahradníková, I. Minarovic, and I. Zahradník. Competitive and cooperative effects of Bay K8644 on the L-type calcium channel current inhibition by calcium channel antagonists. *The Journal of Pharmacology and Experimental Therapeutics*, 322(2):638–45, Aug. 2007. doi: 10.1124/jpet.107.122176.

[163] H.-Q. Zhan, L. Xia, G.-F. Shou, Y.-l. Zang, F. Liu, and S. Crozier. Fibroblast proliferation alters cardiac excitation conduction and contraction: a computational study. *Journal of Zhejiang University. Science. B*, 15(3):225–42, Mar. 2014. doi: 10.1631/jzus.B1300156.

[164] H. Zhang, A. V. Holden, I. Kodama, H. Honjo, M. Lei, T. Varghese, and M. R. Boyett. Mathematical models of action potentials in the periphery and center of the rabbit sinoatrial node. *American Journal of Physiology - Heart and Circulatory Physiology*, 279(1):H397–421, July 2000.

[165] O. C. Zienkiewicz. *The Finite Element Method in Engineering Science*. McGraw-Hill London, 2nd edition, 1971. ISBN 070941386.

[166] O. C. Zienkiewicz and R. L. Taylor. *Finite Element Method: Volume 1 - The Basis*. Butterworth-Heinemann, Oxford, 5th edition, 2000.

[167] O. C. Zienkiewicz and R. L. Taylor. *Finite Element Method: Volume 2 - Solid Mechanics*. Butterworth-Heinemann, Oxford, 5th edition, 2000.

Der Lebenslauf ist in der Online-Version aus Grnden des Datenschutzes nicht enthalten.

In dieser Schriftenreihe bisher erschienene Berichte:

Nr. 1 (2004) *Ein Modell zur Beschreibung finiter anisotroper elastoplastischer Deformationen unter Berücksichtigung diskreter Rissausbreitung*, J. Löblein, Dissertation, 2004.

Nr. 2 (2006) *Polyconvex Anisotropic Energies and Modeling of Damage applied to Arterial Walls*, D. Balzani, Dissertation, 2006.

Nr. 3 (2006) *Kontinuumsmechanische Modellierung ferroelektrischer Materialien im Rahmen der Invariatentheorie*, H. Romanowski, Dissertation, 2006.

Nr. 4 (2007) *Mehrskalen-Modellierung polykristalliner Ferroelektrika basierend auf diskreten Orientierungsverteilungsfunktionen*, I. Kurzhöfer, Dissertation, 2007.

Nr. 5 (2007) *Proceedings of the First Seminar on the Mechanics of Multifunctional Materials*, J. Schröder, D.C. Lupascu, D. Balzani (Ed.), Tagungsband, 2007.

Nr. 6 (2008) *Zur Modellierung und Simulation diskreter Rissausbreitungsvorgänge*, O. Hilgert, Dissertation, 2008.

Nr. 7 (2009) *Least-Squares Mixed Finite Elements for Solid Mechanics*, A. Schwarz, Dissertation, 2009.

Nr. 8 (2010) *Design of Polyconvex Energy Functions for All Anisotropy Classes*, V. Ebbing, Dissertation, 2010.

Nr. 9 (2012) *Modeling of Electro-Mechanically Coupled Materials on Multiple Scales*, M.-A. Keip, Dissertation, 2012.

Nr. 10 (2012) *Geometrical Modeling and Numerical Simulation of Heterogeneous Materials*, D. Brands, Dissertation, 2012.

Nr. 11 (2012) *Modeling and simulation of arterial walls with focus on damage and residual stresses*, S. Brinkhues, Dissertation, 2012.

Nr. 12 (2014) *Proceedings of the Second Seminar on the Mechanics of Multifunctional Materials*, J. Schröder, D.C. Lupascu, M.-A. Keip, D. Brands (Ed.), Tagungsband, 2014.

Nr. 13 (2016) *Mixed least squares finite element methods based on inverse stress-strain relations in hyperelasticity*, B. Müller, Dissertation, 2016.

Nr. 14 (2016) *Electromechanical Modeling and Simulation of Thin Cardiac Tissue Constructs*, R. Frotscher, Dissertation, 2016.